Chapter five

Unrestricted Hartree-Fock study of the ground states and single-particle excitation spectra of perovskite-type 3*d* transition-metal oxides

We have studied transition-metal 3*d*-oxygen 2*p* lattice models, where full degeneracy of transition-metal 3*d* and oxygen 2*p* orbitals and on-site Coulomb and exchange interactions between 3*d* electrons are taken into account, by means of spin- and orbital-unrestricted Hartree-Fock (HF) approximation. The electronic-structure parameters deduced from the cluster-model analyses of the photoemission spectra are used as input. We have applied this method to perovskite-type 3*d* transition-metal oxides, which exhibit various electrical and magnetic properties. It is shown that the HF results can explain various magnetic structures of insulating oxides. However, the HF calculations tend to overestimate the magnitude of the band gap compared with the experimental results and to predict some paramagnetic metals as magnetic insulators. Single-particle excitation spectra calculated using Koopmans' theorem give us a crude but useful picture on the electronic structure of the perovskite-type 3*d* transition-metal oxides.

5.1. Introduction

In these decades, there have been many attempts to understand a variety of electrical and magnetic properties of 3*d* transition-metal oxides, especially their metal-insulator transitions [Mott, 1990]. Mott [1949] and Hubbard [1963] have shown that the strong *d*-*d* Coulomb interaction is essential to explain why many 3*d* transition-metal compounds with partially filled 3*d* band can exist as magnetic insulators. When the band width of the 3*d* band is larger than the *d*-*d* Coulomb interaction, the compound becomes metallic. When the *d*-*d* Coulomb interaction prevails the band width, the 3*d* electrons are localized and the compound turns into an insulator with local magnetic moment, whose band gap is determined by the magnitude of the *d*-*d* Coulomb interaction. The essential point of the Mott metal-insulator transition is described by the single-band Hubbard model [Hubbard, 1964a, 1964b]. However, in real compounds, the degeneracy of the 3*d* orbitals makes the symmetry-broken state of the magnetic insulator complicated and might affect the metal-insulator transition. In order to study the effect of the orbital degeneracy in the insulating state, a degenerate-band Hubbard model has been studied by applying unrestricted Hartree-Fock (HF) approximation on the Coulomb-interaction term and by constructing an effective Hamiltonian through second order perturbation with respect to the hybridization term [Kugel and Khomskii, 1973, 1982; Inagaki and Kubo, 1973; Cyrot and Lyon-Caen, 1975; Inagaki, 1975; Wakoh, 1977]. Castellani, Natoli and Ranninger [1975] have applied the unrestricted HF calculation to a realistic degenerate Hubbard model for V_2O_3, where hopping term reflects the corrundum structure. Ashkenazi and Weger [1973] have also studied the metal-insulator transitions of Ti_2O_3 and V_2O_3 using the HF method. The validity of the unrestricted HF approach to the Mott transition has generally been discussed by Brandow [1977]. However, in these calculations, the O 2*p* orbitals were not explicitly included and the only transfer integrals between effective *d* orbitals, which correspond to the antibonding band formed by the hybridization between the transition-metal 3*d* and oxygen 2*p* orbitals, were considered.

Following the development of photoemission spectroscopy, Fujimori and Minami have shown that the band gap of NiO is not determined by *d*-*d* Coulomb interaction but by oxygen-to-metal 3*d* charge-transfer energy from the NiO_6 cluster-model calculation [Fujimori and Minami, 1984]. Zaanen, Sawatzky and Allen and Hüfner have provided a clear classification scheme, so-called Zaanen-Sawatzky-Allen (ZSA) scheme based on the Anderson-impurity model [Zaanen *et al.*, 1985; Hüfner, 1985], in which transition-metal compounds can be classified into two regimes according to the relative magnitude of the ligand-to-metal charge-transfer energy Δ and *d*-*d* Coulomb energy U. In the Mott-Hubbard regime, where $\Delta > U$, the band gap corresponds to charge fluctuations of the *d*-*d* type, $d^n + d^n \rightarrow d^{n+1} + d^{n-1}$ and its magnitude is essentially given by $\sim U$. In the charge-transfer regime, where $\Delta < U$, charge fluctuations of the type $d^n + d^n \rightarrow d^{n+1} + d^n\underline{L}$ constitute a *p*-*d* type band gap, whose magnitude

is $\sim \Delta$. Therefore, in order to investigate the metal-insulator transition in which the charge-transfer-type band gap collapses, it is essential to explicitly include the ligand *p* orbitals in the model. On the other hand, the cluster and Anderson-impurity models, which have succeeded in reproducing the photoemission spectra and extracting the important electronic-structure parameters Δ and U, neglect the translational symmetry of the crystals. Therefore, it is difficult to study the metal-insulator transition by using the cluster and Anderson-impurity models.

In this chapter, we have studied transition-metal 3*d*-oxygen 2*p* lattice models, where full degeneracy of transition-metal 3*d* and oxygen 2*p* orbitals and on-site Coulomb and exchange interactions for transition-metal sites are taken into account, by means of spin- and orbital-unrestricted Hartree-Fock (HF) approximations. The aim of the present calculation is two fold. One is to refine the previous HF method [Ashkenazi and Weger, 1973; Inagaki and Kubo, 1973; Castellani *et al.*, 1975; Cyrot and Lyon-Caen, 1975; Wakoh, 1977] by including oxygen 2*p* orbitals explicitly and the other is to extend the cluster-model calculation by including the translational symmetry of the 3*d* orbitals. The organization of this chapter is as follows. In Sec. 5.2, we explain how to apply the unrestricted HF approximation to the perovskite-type lattice model. In Sec. 5.3, results of the HF calculation for various perovskite-type 3*d* transition-metal oxides are presented. Finally, we summarize the results of the unrestricted HF calculations and discuss the limitation of the HF approximation in Sec 5.4.

5.2. Unrestricted Hartree-Fock approximation

Within the HF approximation, the wave function of a many-electron system can be written in the form of an anti-symmetrized product of one-electron wave functions or of a single Slater determinant. The one-electron wave functions are determined by solving a set of HF equations. The unrestricted HF approximation allows the ground-state wave function to have lower symmetry than that of the Hamiltonian. One can calculate the single-electron excitation spectrum from the HF results by using Koopmans' theorem.

We have applied the unrestricted HF approximation to the multiband *d*-*p* model, where ten-fold degeneracy of the transition-metal 3*d* orbitals and six-fold degeneracy of the oxygen 2*p* orbitals are taken into account. The interatomic 3*d*-3*d* Coulomb interaction is expressed by Kanamori parameters, u, u', j and j' [Kanamori, 1963]. We have to assume the relationships $u' = u - 2j$ and $j' = j$ in order to keep the rotational invariance in real space of the Coulomb terms [Kanamori ,1963; Brandow, 1977]. The Hamiltonian is given by

$$H = H_d + \varepsilon_p \sum_{\vec{k},l,\sigma} p^+_{\vec{k},l\sigma} p_{\vec{k},l\sigma} + \sum_{\vec{k},l>l',\sigma} V^{pp}_{\vec{k},ll'} p^+_{\vec{k},l\sigma} p_{\vec{k},l'\sigma} + \text{H. c.}$$
$$+ \sum_{\vec{k},l,\beta m,\sigma} V^{pd}_{\vec{k},l\beta m} p^+_{\vec{k},l\sigma} d_{\vec{k},\beta m\sigma} + \text{H. c.}\ , \qquad (5.1)$$

$$H_d = \varepsilon^0_{d\,\alpha,\beta,m,\sigma} \sum d^+_{\alpha,\beta m\sigma}\, d_{\alpha,\beta m\sigma} + \sum_{\alpha,\beta,m,m',\sigma,\sigma'} h_{m\sigma,m'\sigma'}\, d^+_{\alpha,\beta m\sigma}\, d_{\alpha,\beta m'\sigma'}$$
$$+ \sum_{\alpha,\beta,m} u\, d^+_{\alpha,\beta m\uparrow}\, d_{\alpha,\beta m\uparrow}\, d^+_{\alpha,\beta m\downarrow}\, d_{\alpha,\beta m\downarrow} + \sum_{\alpha,\beta,m\neq m'} u'\, d^+_{\alpha,\beta m\uparrow}\, d_{\alpha,\beta m\uparrow}\, d^+_{\alpha,\beta m'\downarrow}\, d_{\alpha,\beta m'\downarrow}$$
$$+ \sum_{\alpha,\beta,m>m',\sigma} (u'-j)\, d^+_{\alpha,\beta m\sigma}\, d_{\alpha,\beta m\sigma}\, d^+_{\alpha,\beta m'\sigma}\, d_{\alpha,\beta m'\sigma}$$
$$+ \sum_{\alpha,\beta,m\neq m'} j'\, d^+_{\alpha,\beta m\uparrow}\, d_{\alpha,\beta m'\uparrow}\, d^+_{\alpha,\beta m\downarrow}\, d_{\alpha,\beta m'\downarrow}$$
$$+ \sum_{\alpha,\beta,m\neq m'} j\, d^+_{\alpha,\beta m\uparrow}\, d_{\alpha,\beta m'\uparrow}\, d^+_{\alpha,\beta m'\downarrow}\, d_{\alpha,\beta m\downarrow}\ , \qquad (5.2)$$

where $d^+_{\vec{k},\beta m\sigma} \equiv (1/\sqrt{N}) \sum_{\vec{\alpha}} e^{i\vec{k}\cdot\vec{R}_\alpha} d^+_{\alpha,\beta m\sigma}$ and $p^+_{\vec{k},l\sigma}$ are creation operators for Bolch electrons constructed from the transition-metal $3d$ and oxygen $2p$ orbitals, respectively. α and $\vec{k}$ label the unit cell and the wave vector in the first Brillouin zone. β and m are indices for the transition-metal atoms in the unit cell and the $3d$ orbitals on the transition-metal atom, respectively. l denotes the $2p$ orbitals in the unit cell. $V^{pp}_{\vec{k},ll'}$ and $V^{pd}_{\vec{k},lm}$ are $2p$-$2p$ and $2p$-$3d$ transfer integrals. $h_{m\sigma,m'\sigma'}$ represents crystal field and spin-orbit interactions of the $3d$ orbitals. Using the unrestricted HF approximation, the mean-field Hamiltonian becomes

$$H^{MF}_d = \varepsilon^0_{d\,\alpha,\beta,m\sigma} \sum d^+_{\alpha,\beta m\sigma}\, d_{\alpha,\beta m\sigma} + \sum_{\alpha,\beta,m\sigma,m'\sigma'} h_{m\sigma,m'\sigma'}\, d^+_{\alpha,\beta m\sigma}\, d_{\alpha,\beta m'\sigma'}$$
$$+ \sum_{\alpha,\beta,m} u \left\langle d^+_{\alpha,\beta m\uparrow} d_{\alpha,\beta m\uparrow} \right\rangle d^+_{\alpha,\beta m\downarrow} d_{\alpha,\beta m\downarrow} + \sum_{\alpha,\beta,m} u\, d^+_{\alpha,\beta m\uparrow} d_{\alpha,\beta m\uparrow} \left\langle d^+_{\alpha,\beta m\downarrow} d_{\alpha,\beta m\downarrow} \right\rangle$$
$$- \sum_{\alpha,\beta,m} u \left\langle d^+_{\alpha,\beta m\uparrow} d_{\alpha,\beta m\uparrow} \right\rangle \left\langle d^+_{\alpha,\beta m\downarrow} d_{\alpha,\beta m\downarrow} \right\rangle$$
$$+ \sum_{\alpha,\beta,m\neq m'} u' \left\langle d^+_{\alpha,\beta m\uparrow} d_{\alpha,\beta m\uparrow} \right\rangle d^+_{\alpha,\beta m'\downarrow} d_{\alpha,\beta m'\downarrow} + \sum_{\alpha,\beta,m\neq m'} u'\, d^+_{\alpha,\beta m\uparrow} d_{\alpha,\beta m\uparrow} \left\langle d^+_{\alpha,\beta m'\downarrow} d_{\alpha,\beta m'\downarrow} \right\rangle$$
$$- \sum_{\alpha,\beta,m\neq m'} u' \left\langle d^+_{\alpha,\beta m\uparrow} d_{\alpha,\beta m\uparrow} \right\rangle \left\langle d^+_{\alpha,\beta m'\downarrow} d_{\alpha,\beta m'\downarrow} \right\rangle$$
$$+ \sum_{\alpha,\beta,m>m',\sigma} (u'-j) \left\langle d^+_{\alpha,\beta m\sigma} d_{\alpha,\beta m\sigma} \right\rangle d^+_{\alpha,\beta m'\sigma} d_{\alpha,\beta m'\sigma} +$$
$$\sum_{\alpha,\beta,m>m',\sigma} (u'-j)\, d^+_{\alpha,\beta m\sigma} d_{\alpha,\beta m\sigma} \left\langle d^+_{\alpha,\beta m'\sigma} d_{\alpha,\beta m'\sigma} \right\rangle$$
$$- \sum_{\alpha,\beta,m>m',\sigma} (u'-j) \left\langle d^+_{\alpha,\beta m\sigma} d_{\alpha,\beta m\sigma} \right\rangle \left\langle d^+_{\alpha,\beta m'\sigma} d_{\alpha,\beta m'\sigma} \right\rangle$$
$$- \sum_{\alpha,\beta,m>m',\sigma} (u'-j) \left\langle d^+_{\alpha,\beta m\sigma} d_{\alpha,\beta m'\sigma} \right\rangle d^+_{\alpha,\beta m'\sigma} d_{\alpha,\beta m\sigma} -$$
$$\sum_{\alpha,\beta,m>m',\sigma} (u'-j)\, d^+_{\alpha,\beta m\sigma} d_{\alpha,\beta m'\sigma} \left\langle d^+_{\alpha,\beta m'\sigma} d_{\alpha,\beta m\sigma} \right\rangle$$
$$+ \sum_{\alpha,\beta,m>m',\sigma} (u'-j) \left\langle d^+_{\alpha,\beta m\sigma} d_{\alpha,\beta m'\sigma} \right\rangle \left\langle d^+_{\alpha,\beta m'\sigma} d_{\alpha,\beta m\sigma} \right\rangle$$
$$+ \sum_{\alpha,\beta,m\neq m'} j' \left\langle d^+_{\alpha,\beta m\uparrow} d_{\alpha,\beta m\uparrow} \right\rangle d^+_{\alpha,\beta m\downarrow} d_{\alpha,\beta m'\downarrow} + \sum_{\alpha,\beta,m\neq m'} j'\, d^+_{\alpha,\beta m\uparrow} d_{\alpha,\beta m\uparrow} \left\langle d^+_{\alpha,\beta m\downarrow} d_{\alpha,\beta m'\downarrow} \right\rangle$$
$$- \sum_{\alpha,\beta,m\neq m'} j' \left\langle d^+_{\alpha,\beta m\uparrow} d_{\alpha,\beta m\uparrow} \right\rangle \left\langle d^+_{\alpha,\beta m\downarrow} d_{\alpha,\beta m'\downarrow} \right\rangle$$
$$+ \sum_{\alpha,\beta,m\neq m'} j \left\langle d^+_{\alpha,\beta m\uparrow} d_{\alpha,\beta m\uparrow} \right\rangle d^+_{\alpha,\beta m'\downarrow} d_{\alpha,\beta m\downarrow} + \sum_{\alpha,\beta,m\neq m'} j\, d^+_{\alpha,\beta m\uparrow} d_{\alpha,\beta m'\uparrow} \left\langle d^+_{\alpha,\beta m'\downarrow} d_{\alpha,\beta m\downarrow} \right\rangle$$
$$- \sum_{\alpha,\beta,m\neq m'} j \left\langle d^+_{\alpha,\beta m\uparrow} d_{\alpha,\beta m'\uparrow} \right\rangle \left\langle d^+_{\alpha,\beta m'\downarrow} d_{\alpha,\beta m\downarrow} \right\rangle \quad . \qquad (5.3)$$

If we concentrate on a homogeneous solution, the Hamiltonian can be written as

$$H^{MF}_d = \varepsilon^0_{d\,\vec{k},\beta,m,\sigma} \sum d^+_{\vec{k},\beta m,\sigma}\, d_{\vec{k},\beta m,\sigma} + \sum_{\vec{k},\beta,m,m',\sigma,\sigma'} h_{m\sigma,m'\sigma'}\, d^+_{\vec{k},\beta m\,\sigma}\, d_{\vec{k},\beta m'\,\sigma'}$$
$$+ \sum_{\vec{k},\beta,m} u \left\langle n^d_{\beta m\uparrow} \right\rangle d^+_{\vec{k},\beta m\downarrow} d_{\vec{k},\beta m\downarrow} + \sum_{\vec{k},\beta,m} u\, d^+_{\vec{k},\beta m\uparrow} d_{\vec{k},\beta m\uparrow} \left\langle n^d_{\beta m\downarrow} \right\rangle$$
$$- \sum_{\vec{k},\beta,m} u \left\langle n^d_{\beta m\uparrow} \right\rangle \left\langle n^d_{\beta m\downarrow} \right\rangle$$
$$+ \sum_{\vec{k},\beta,m\neq m'} u' \left\langle n^d_{\beta m\uparrow} \right\rangle d^+_{\vec{k},\beta m'\downarrow} d_{\vec{k},\beta m'\downarrow} + \sum_{\vec{k},\beta,m\neq m'} u'\, d^+_{\vec{k},\beta m\uparrow} d_{\vec{k},\beta m\uparrow} \left\langle n^d_{\beta m'\downarrow} \right\rangle$$
$$- \sum_{\vec{k},\beta,m\neq m'} u' \left\langle n^d_{\beta m\uparrow} \right\rangle \left\langle n^d_{\beta m'\downarrow} \right\rangle$$
$$+ \sum_{\vec{k},\beta,m>m',\sigma} (u'-j) \left\langle n^d_{\beta m\sigma} \right\rangle d^+_{\vec{k},\beta m'\sigma} d_{\vec{k},\beta m'\sigma} + \sum_{\vec{k},\beta,m>m',\sigma} (u'-j)\, d^+_{\vec{k},\beta m\sigma} d_{\vec{k},\beta m\sigma} \left\langle n^d_{\beta m'\sigma} \right\rangle$$
$$- \sum_{\vec{k},\beta,m>m',\sigma} (u'-j) \left\langle n^d_{\beta m\sigma} \right\rangle \left\langle n^d_{\beta m'\sigma} \right\rangle$$
$$- \sum_{\vec{k},\beta,m>m',\sigma} (u'-j) \left\langle b^d_{\beta mm'\sigma} \right\rangle d^+_{\vec{k},\beta m'\sigma} d_{\vec{k},\beta m\sigma} - \sum_{\vec{k},\beta,m>m',\sigma} (u'-j)\, d^+_{\vec{k},\beta m\sigma} d_{\vec{k},\beta m'\sigma} \left\langle b^d_{\beta m'm\sigma} \right\rangle$$
$$+ \sum_{\vec{k},\beta,m>m',\sigma} (u'-j) \left\langle b^d_{\beta mm'\sigma} \right\rangle \left\langle b^d_{\beta m'm\sigma} \right\rangle$$
$$+ \sum_{\vec{k},\beta,m\neq m'} j' \left\langle b^d_{\beta mm'\uparrow} \right\rangle d^+_{\vec{k},\beta m\downarrow} d_{\vec{k},\beta m'\downarrow} + \sum_{\vec{k},\beta,m\neq m'} j'\, d^+_{\vec{k},\beta m\uparrow} d_{\vec{k},\beta m'\uparrow} \left\langle b^d_{\beta mm'\downarrow} \right\rangle$$
$$- \sum_{\vec{k},\beta,m\neq m'} j' \left\langle b^d_{\beta mm'\uparrow} \right\rangle \left\langle b^d_{\beta mm'\downarrow} \right\rangle$$
$$+ \sum_{\vec{k},\beta,m\neq m'} j \left\langle b^d_{\beta mm'\uparrow} \right\rangle d^+_{\vec{k},\beta m'\downarrow} d_{\vec{k},\beta m\downarrow} + \sum_{\vec{k},\beta,m\neq m'} j\, d^+_{\vec{k},\beta m\uparrow} d_{\vec{k},\beta m'\uparrow} \left\langle b^d_{\beta m'm\downarrow} \right\rangle$$
$$- \sum_{\vec{k},\beta,m\neq m'} j \left\langle b^d_{\beta mm'\uparrow} \right\rangle \left\langle b^d_{\beta m'm\downarrow} \right\rangle \quad , \qquad (5.4)$$

where

$$\left\langle n^d_{\beta m\sigma} \right\rangle \equiv \left\langle d^+_{\alpha,\beta m\sigma} d_{\alpha,\beta m\sigma} \right\rangle = \frac{1}{N} \sum_{\vec{k}} \left\langle d^+_{\vec{k},\beta m\sigma} d_{\vec{k},\beta m\sigma} \right\rangle \qquad (5.6)$$

and

$$\left\langle b^d_{\beta mm'\sigma\sigma'} \right\rangle \equiv \left\langle d^+_{\alpha,\beta m\sigma} d_{\alpha,\beta m'\sigma'} \right\rangle = \frac{1}{N} \sum_{\vec{k}} \left\langle d^+_{\vec{k},\beta m\sigma} d_{\vec{k},\beta m'\sigma'} \right\rangle \qquad (5.7)$$

are order parameters to be determined self-consistently. The HF wave function then becomes a Slater determinant constructed from Bloch functions.

The charge-transfer energy Δ for d^n is defined as $\varepsilon_d{}^0 - \varepsilon_p + nU$, where U (= u -20/9j) is the multiplet average of the d-d Coulomb interaction. We can also define the charge-transfer energy Δ_{eff} and U_{eff} with respect to the lowest term of each d^n configurations. The transfer

integrals are given in terms of Slater-Koster parameters ($pp\sigma$), ($pp\pi$), ($pd\sigma$) and ($pd\pi$) [Slater and Koster, 1954]. The values for Δ, U and ($pd\sigma$) are obtainable from cluster-model analyses of valence-band and transition-metal $2p$ core-level photoemission spectra, where systematic variation of the parameters have been investigated. The charge-transfer energy Δ increases as the atomic number of the transition metal decreases. The charge-transfer energies have been estimated to be ~ 1 eV for $PrNiO_3$ [Chapter 3], ~ 3 eV for $LaFeO_3$ [Bocquet *et al.*, 1992], ~ 4 eV for $LaMnO_3$ [Bocquet *et al.*, 1992, Saitoh *et al.*, 1995a], ~ 5 eV for $LaCrO_3$ [Saitoh *et al.*, 1995b] and ~ 6 eV for $LaTiO_3$ [Bocquet *et al.*, 1995; Saitoh *et al.*, 1995b] from the cluster-model analyses of the valence-band and transition-metal $2p$ core-level photoemission spectra. It is reasonable to interpolate and extrapolate them and to estimate the Δ for RMO_3 (M = transition metal, R = rare earth and Y) as listed in Table 5.1. Although the systematic variation of U is not so clear as that of Δ, U gradually decreases as the atomic number of the transition metal decreases. U have been estimated to be ~ 6 - 8 eV for late transition-metal oxides [Fujimori and Minami, 1984; Eskes *et al.*, 1990; van Elp, 1991; Bocquet *et al.*, 1992; Saitoh *et al.*, 1995b] and to be ~ 3 - 5 eV for early transition-metal oxides [van Elp, 1991; Uozumi *et al.*, 1993; Bocquet *et al.*, 1995; Saitoh *et al.*, 1995b]. The transfer integral ($pd\sigma$) obtained from the cluster-model analyses for the transition-metal oxides are ranging from -1.0 to -2.5 eV. Based on these results, we have deduced the values of U and ($pd\sigma$) listed in Table 5.1. The ratio of ($pd\sigma$) and ($pd\pi$) is fixed to ~ -2, which is derived from the LCAO fitting of the band calculation [Mattheiss, 1972]. The ($pp\sigma$) and ($pp\pi$) are also fixed to -0.60 and 0.15 eV, which is also taken from the LCAO fitting [Mattheiss, 1972]. Ambiguity of the latter two parameters dose not change the conclusion. The Kanamori parameters can be translated to Racah parameters by the relations $u = A + 4B + 3C$ and $j = 5/2B + C$. The Racah B and C parameters are fixed to free ion values or 0.8 times of the atomic Hartree-Fock values [Mann; de Groot *et al.*, 1990].

The $GdFeO_3$-type structure is orthorhombic with orthogonal a, b and c-axes and the unit cell contains four transition-metal ions. Let us denote the four sites as sites 1, 2, 3 and 4 as shown in Fig. 5.1 (a). $GdFeO_3$-type structure is obtained by tilting the MO_6 octahedra of cubic perovskite structure. Here, we simulate the $GdFeO_3$-type distortion by rotating the MO_6 octahedra by angle θ and $-\theta$ about the three-fold axes of the octahedra or the $(0, -\sqrt{2}/2, \sqrt{2}/2)$ and $(0, \sqrt{2}/2, \sqrt{2}/2)$ axes with respect to a, b and c-axis of the $GdFeO_3$ structure. As a result, the M-O-M bond angles becomes $180 - 2\alpha$ along the x, y and z-directions ($\cos\alpha = 2/3\cos\theta + 1/3$). Here, we have chosen the x, y and z-directions for atomic orbitals to be $(\sqrt{2}/2, -\sqrt{2}/2, 0)$, $(\sqrt{2}/2, \sqrt{2}/2, 0)$ and $(0, 0, 1)$, respectively, with respect to the a, b and c-axes. In addition to the $GdFeO_3$-type distortion, some of the perovskite-type oxides show Jahn-Teller distortions in which the MO_6 octahedra are alternatingly elongated along the x and y direction within the c plane. There are two types of the Jahn-Teller distortions as shown in Fig 5.1(b) depending on the way of stacking the elongated octahedra along the c-axis [Okazaki, 1969; Hutchings *et al.*, 1969; Tsukuda and Okazaki, 1972]. Basic magnetic structures for the perovskite-type

transition-metal oxides, namely, ferromagnetic (FM), A-type antiferromagnetic (AFM), C-type AFM and G-type AFM structures, are shown in Fig. 5. 2 [Wollan and Koehler, 1955].

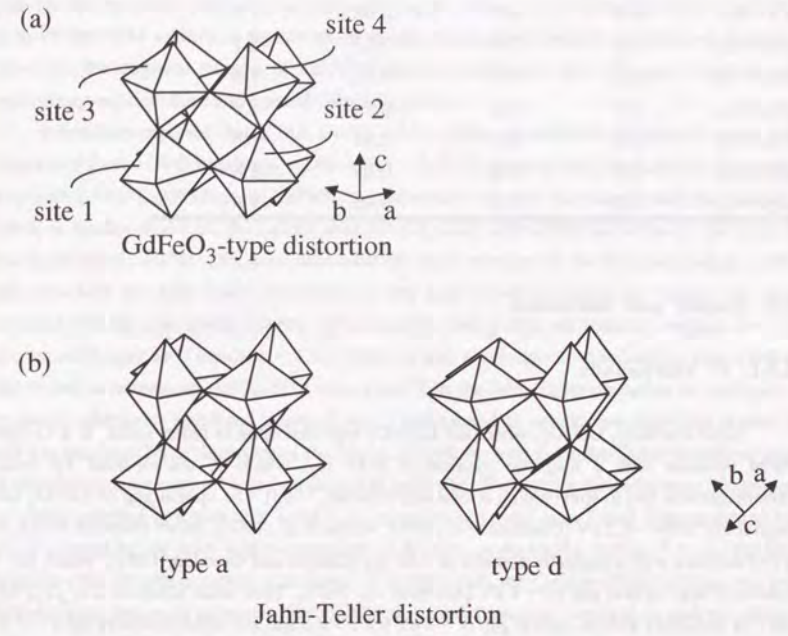

Fig. 5.1. (a) $GdFeO_3$-type lattice distortion. (b) Two types of Jahn-Teller lattice distortion.

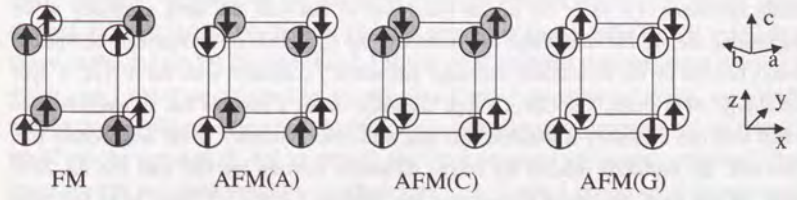

Fig. 5.2. Typical spin- and orbital-ordered structures for the perovskites. Arrows indicate the spin polarization. open and shaded circles represent different orbitals.

Table 5.1. Parameters for the Hartree-Fock calculations (in eV).

	Δ	U	J	$(pd\sigma)$
RTi^{3+}O$_3$	7.0	4.0	0.64	-2.2
RV^{3+}O$_3$	6.0	4.5	0.68	-2.2
RCr^{3+}O$_3$	5.0	5.0	0.72	-2.2
RMn^{3+}O$_3$	4.0	5.5	0.76	-1.8
RFe^{3+}O$_3$	3.0	6.0	0.80	-1.8
RCo^{3+}O$_3$	2.0	6.5	0.84	-1.8
RNi^{3+}O$_3$	1.0	7.0	0.88	-1.8
RCu^{3+}O$_3$	0.0	7.5	0.92	-1.8

5.3. Results and discussion

5.3.1. d^1 compounds

Experimentally, $LaTiO_3$, where the $GdFeO_3$-type distortion is rather small, is a G-type AFM insulator with a magnetic moment of 0.45 μ_B, which is accompanied by weak ferromagnetism due to spin canting [Goral and Greedan, 1983]. The optical gap of $LaTiO_3$ has been found to be ~ 0.2 eV [Crandles *et al.*, 1992; Arima *et al.*, 1993]. More distorted $YTiO_3$ is a FM insulator with a magnetic moment of 0.84 μ_B [Garrett and Greedan, 1981], which has a relatively large optical gap of ~ 1 eV [Arima *et al.*, 1993]. Their solid solutions $La_{1-x}Y_xTiO_3$ are FM insulators with an optical gap of ~ 1 eV for $x > 0.6$ and are AFM insulators for $x < 0.6$. As x goes from 1.0 to 0.0, the magnitude of the optical gap decreases from 1.0 eV to 0.2 eV [Goral *et al.*, 1982; Okimoto *et al.*, 1995].

Without the distortion, one of the three-fold degenerate t_{2g} orbitals should be occupied at each transition-metal site in the insulating d^1 system. Since an electron in an orbital with a certain symmetry (xy, yz or zx) can be transferred to that with the same symmetry at the neighboring site, the FM state where two or three of the t_{2g} orbitals are alternatingly occupied is always favored by the intra-atomic exchange interaction j compared with the A-type, C-type and G-type AFM states. The $GdFeO_3$-type distortion makes it possible that an electron in an orbital with one symmetry is transferred to that with other symmetry at the neighboring site. Therefore, the distortion reduces the energy difference between the FM state and the AFM states. At this stage, we cannot explain why less distorted $LaTiO_3$ is G-type AFM and more distorted $YTiO_3$ is FM. In order to explain why the G-type AFM state is realized in $LaTiO_3$, we have taken account of the spin-orbit interaction represented by the parameter ζ_d = 0.018 eV. With the spin-orbit interaction, the spins and orbitals cannot order independently. The spin-orbit interaction favors the $z'x'\uparrow + iy'z'\uparrow$ and $z'x'\downarrow - iy'z'\downarrow$ type spin-orbitals, in which the spin points in the z'-direction and the orbital angular momentum is antiparalell to that of the spin. A G-type AFM solution, where the two spin-orbitals are alternatingly occupied with the z'-axis pointing (1, 1, 1)-direction in terms of the x, y and z-axes, is expected to be favored both by the spin-obit interaction and by the superexchange interaction [Kanamori, 1959]. Actually the AFM solution is the lowest in energy among the solutions we have investigated. However, the magnetic moment of the AFM state is calculated to be ~ 0.1 μ_B, which is too small compared with the experimental value of $LaTiO_3$.

It has been reported that $YTiO_3$ shows a Jahn-Teller distortion of the type d, where the longer and shorter Ti-O bonds are ~ 2.08 Å and ~ 2.02 Å, respectively [MacLean *et al.*, 1979; Tomimoto, 1995]. Although, in $LaTiO_3$, the difference between the longer and shorter Ti-O bonds is smaller than 0.01 Å, $LaTiO_3$ may have a small Jahn-Teller distortion of the type d [MacLean *et al.*, 1979]. We have calculated the total energies of the FM and G-type AFM solutions with the Jahn-Teller distortions of the type a and d (Fig. 5.1). Here, we have assumed that the ratio $(pd\sigma)_s/(pd\sigma)_l$, where $(pd\sigma)_s$ and $(pd\sigma)_l$ are transfer integrals for the shorter and longer Ti-O bonds, is ~ 1.17. While xy and yz orbitals are stabilized at sites 1 and 4 and xy and zx orbitals are stabilized at sites 2 and 3 in the Jahn-Teller distortion of the type a, xy and yz orbitals are stabilized at sites 1 and 3 and xy and zx orbitals are stabilized at sites 2 and 4 in the Jahn-Teller distortion of the type d. Therefore, with the Jahn-Teller distortion, one of the doubly degenerate orbitals is occupied at each site. Without the $GdFeO_3$-type distortion, an orbital ordering in which sites 1 and 4 are occupied by yz and sites 2 and 3 are occupied by zx, is favored by the Jahn-Teller distortions of the type a. As shown in Fig. 5.3 (a), the FM solution with the orbital ordering is lower in energy than the G-type AFM solution. As the $GdFeO_3$-type distortion increases, the xy orbital is mixed into the occupied zx and yz orbitals and the energy difference between the FM and AFM solutions hardly changes. With the Jahn-Teller distortion of the type d, a FM solution with the yz, xy, xy, zx-type orbital ordering, in which sites 1, 2, 3 and 4 are occupied by yz, xy, xy and zx, respectively, is the lowest in energy when the $GdFeO_3$-type distortion is small. As the $GdFeO_3$-type distortion increases, the energy difference between the FM and AFM solutions with the yz, xy, xy, zx-type orbital ordering decreases and the two become almost degenerate in energy for $\angle$Ti-O-Ti = 147.4° as shown in Fig. 5.3 (a). On the other hand, FM and AFM solutions with the orbital ordering in which sites 1 and 4 are occupied by yz and sites 2 and 3 are occupied by zx, are unstable without the $GdFeO_3$-type distortion. As the $GdFeO_3$-type distortion increases, the xy orbital is mixed into the occupied zx and yz orbitals and these solutions are strongly stabilized. As a result, the FM and AFM solutions, in which sites 1, 2, 3 and 4 are occupied by $\alpha yz+\beta xy$, $\alpha zx+\beta xy$, $\alpha yz-\beta xy$ and $\alpha zx-\beta xy$ ($\alpha^2+\beta^2=1$), respectively, become lower in energy than the FM and AFM solutions with the yz, xy, xy, zx-type orbital ordering for $\angle$Ti-O-Ti = 139.3°. In YTiO3, with $\angle$Ti-O-Ti of ~ 140° and the d-type Jahn-Teller distortion, the orbital ordering, in

which sites 1, 2, 3 and 4 are occupied by $\alpha yz+\beta xy$, $\alpha zx+\beta xy$, $\alpha yz-\beta xy$ and $\alpha zx-\beta xy$ ($\alpha^2+\beta^2=1$), respectively, may be realized. This type of orbital ordering has also been found in the *ab-initio* band-structure calculation for $YTiO_3$ using the generalized gradient approximation [Sawada, 1995]. In Fig. 5.3 (b), we have plotted the energy difference between the FM and *G*-type AFM solutions with the above orbital ordering and the magnetic moment of the two solutions as functions of the magnitude of the Jahn-Teller distortion of the type *d*. While the *G*-type AFM state has the lower energy than the FM state for ∠Ti-O-Ti ~ 155.5°, the FM solution is lower in energy than the *G*-type AFM solution for ∠Ti-O-Ti ~ 139.3°. This explains that the less distorted $LaTiO_3$ is AFM and more distorted $YTiO_3$ is FM. With the Jahn-Teller distortion $[(pd\sigma)_s/(pd\sigma)_l]^{1/3} \sim 1.053$, the orbital angular momentum is now almost quenched and the magnetic moment becomes ~ 0.85 μ_B, which is in agreement with the experimental value of $YTiO_3$. As the Jahn-Teller distortion decreases, the magnetic moments of the *G*-type and FM solutions become smaller. With $[(pd\sigma)_s/(pd\sigma)_l]^{1/3} \sim 1.006$, the magnetic moment of the *G*-type AFM state is calculated to be ~ 0.55 μ_B for ∠Ti-O-Ti ~ 155.5°, which is reduced from 1 μ_B because of the spin-orbit coupling and agrees with the experimental value of $LaTiO_3$ [Goral and Greedan, 1983].

The present HF calculation presents us a scenario to explain the difference between AFM $LaTiO_3$ and FM $YTiO_3$: The $GdFeO_3$ distortion stabilizes the FM state with the orbital ordering compared with the AFM state, which causes the Jahn-Teller distortion. The problem is why the Jahn-Teller distortion of the type *d* is realized in $YTiO_3$ instead of the type *a*. The HF calculation cannot provide an answer to this question. In $Y_{1-x}Ca_xTiO_3$, the FM spin ordering disappears $x > 0.1$ and the insulator-to-metal transition occurs at $x = 0.4$ [Taguchi *et al.*, 1993; Tokura *et al.*, 1993; Kumagai *et al.*, 1993]. The PM insulating region ranging from $x = 0.1$ to $x = 0.4$ may be attributed to the orbital ordered state. On the other hand, spin and orbital orderings are strongly coupled by the spin-orbit interaction in $LaTiO_3$. This is consistent with the AFM to PM transition and the insulator-metal transition occur at the same composition in $La_{1-x}Sr_xTiO_3$ [Fujishima *et al.*, 1992; Tokura *et al.*, 1993; Kumagai *et al.*, 1993].

In Fig. 5.4, the density of states for the FM and AFM solutions is shown. The band gap opens between the occupied and unoccupied t_{2g} orbitals, the magnitude of which is mainly determined by $u' - j$. From the HF calculation, the magnitudes of the band gaps for the FM and *G*-type AFM solutions are estimated to be ~ 2.7 eV and 2.8 eV, respectively, which are considerably larger than the experimental values [Crandles *et al.*, 1992; Arima *et al.*, 1993]. The magnitude of the band gap of the FM and *G*-type AFM states is hardly changed by the distortion, contradicting the experimental results [Crandles *et al.*, 1992; Arima *et al.*, 1993]. In the present HF calculation, since the $GdFeO_3$-type distortion makes some e_g character hybridize into the t_{2g} band, the distortion dose not necessarily decrease the band width and increase the band gap as expected from a simple model where only single t_{2g} orbital is considered [Crandles *et al.*, 1992]. This discrepancy may indicate the limitation of the HF

approximation: The breakdown of Koopmans' theorem due to strong orbital relaxation and/or strong electron correlation will reduce the band gaps.

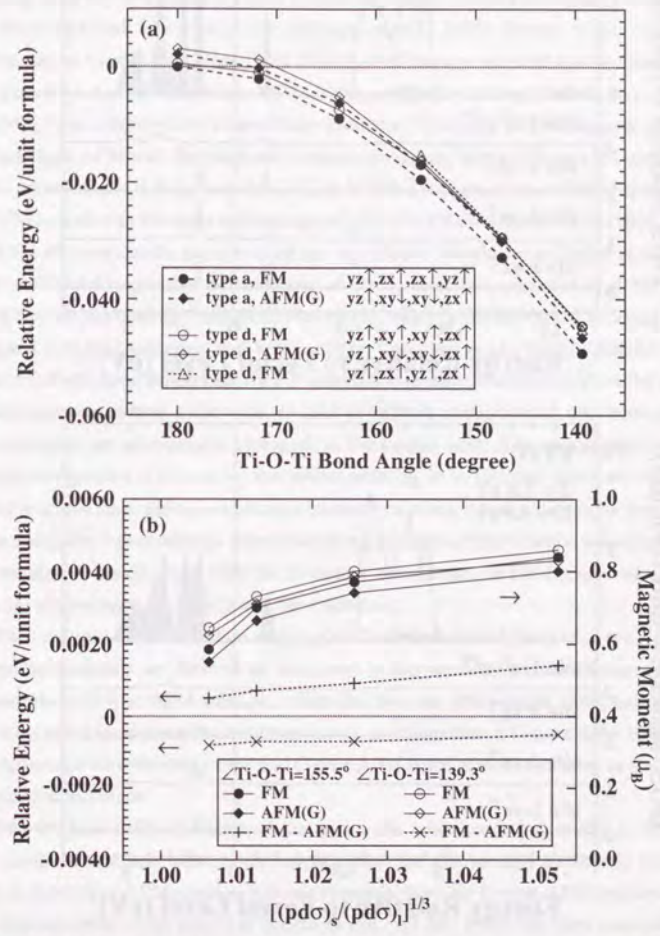

Fig. 5.3. (a) Total energies of various spin and orbital arrangements for $RTiO_3$ as functions of the Ti-O-Ti bond angle. (b) Energy difference between the FM and *G*-type AFM states and magnetic moment of the two states for $RTiO_3$ as functions of the Jahn-Teller lattice distortion of the type *d*.

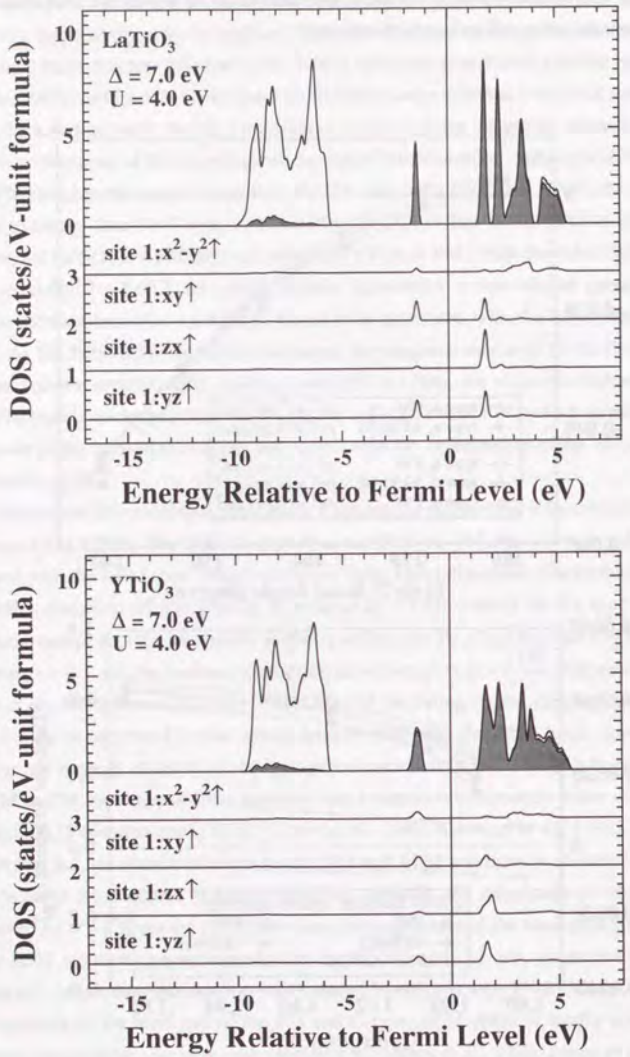

Fig. 5.4. Density of states for $LaTiO_3$ and $YTiO_3$.

5.3.2. d^2 compounds

$LaVO_3$ has a crystallographic and magnetic transition at ~ 140 K. Below the transition temperature, the *C*-type AFM magnetic ordering with magnetic moment ~ 1.3 μ_B is realized and a distortion from the orthorhombic $GdFeO_3$-type structure to monoclinic occurs [Zubkov *et al.*, 1973; Shirakawa and Ishikawa, 1991; Mahajan *et al.*, 1992; Bordet *et al.*, 1993]. The distortion can be viewed as a Jahn-Teller distortion of the type *a*. $LaVO_3$ is an insulator with optical gap of ~ 1.1 eV [Arima *et al.*, 1993]. YVO_3, which has a larger $GdFeO_3$-type distortion than $LaVO_3$, is accompanied by a Jahn-Teller distortion of the type *d*. The magnetic structure of YVO_3 is *G*-type AFM with the magnetic moment of ~ 1.6 μ_B below 77K and is *C*-type with the magnetic moment of ~ 1.0 μ_B between 77 and 118 K [Zubkov *et al.*, 1974; Kawano *et al.*, 1994]. YVO_3 is also an insulator with an optical gap of ~ 1.8 eV [Arima *et al.*, 1993].

In the d^2 compounds, since two of the t_{2g} orbitals should be occupied at each site, a possible orbital ordering is that in which one of the t_{2g} orbitals is occupied in all the sites and the other two are alternatingly occupied. Previously, this type of the orbital ordering has been investigated in V_2O_3 [Ashkenazi and Weger, 1973; Castellani *et al.*, 1975]. Without the Jahn-Teller and $GdFeO_3$-type distortions, the HF calculation predicts that the *C*-type AFM state with the orbital ordering, where a site with *xy* and *yz* orbitals occupied and one with *xy* and *zx* orbitals occupied are alternatingly arranged, is the lowest state. The reason why the *C*-type AFM spin arrangement is favored by this orbital ordering is as follows. Since the *xy* orbital is occupied in all the sites, the superexchange interactions along *x* and *y* directions are AFM. On the other hand, the superexchange interaction along the *z* direction, which is mainly determined by the transfer of the electrons with the *zx* and *yz* symmetries, is FM because the *zx* and *yz* orbitals are alternatingly occupied along the *z* direction.

When the spin-orbit interaction of ζ_d = 0.025 eV is included, the $zx\uparrow + iyz\uparrow$ and $zx\downarrow - iyz\downarrow$ type spin-orbitals are favored as discussed in the previous section [Kanamori; 1959]. Consequently, a *G*-type AFM solution, where the two are alternatingly occupied and the *xy* orbital is occupied in all the sites, becomes lower in energy than a *C*-type AFM solution. The energy difference between the *G*-type and *C*-type AFM states becomes smaller as the $GdFeO_3$-type distortion increases.

With the Jahn-Teller distortion of the type *a*, the orbital ordering, where a site with *xy* and *yz* occupied and one with *xy* and *zx* occupied are alternatingly arranged, is regained. Therefore, the *C*-type AFM solution is lower in energy than the *G*-type AFM solution with the Jahn-Teller distortion of the type *a* as shown in Fig. 5.5 (a). Here, we have assumed that the ratio $(pd\sigma)_s/(pd\sigma)_l$, where $(pd\sigma)_s$ and $(pd\sigma)_l$ are transfer integrals for the shorter and longer V-O bonds, is ~ 1.17. This result can explain why the $LaVO_3$ accompanied by the *a*-type distortion is *C*-type AFM. On the other hand, in the orbital ordering driven by the Jahn-Teller distortion of the type *d*, the same pair of orbitals are occupied along the *c*-axis and the FM spin

coupling along the *c*-axis is not favored. Therefore, with the Jahn-Teller distortion of the type *d*, the *G*-type AFM solution is lower in energy than the *C*-type AFM solution, which agrees with the experimental result that YVO_3 with the *d*-type Jahn-Teller distortion shows *G*-type AFM. However, in the present calculation, the energy gain by the *a*-type Jahn-Teller distortion is larger than that by the *d*-type irrespective of the magnitude of the $GdFeO_3$-type lattice distortion as shown in Fig. 5.5 (a). The HF calculation fails to explain why less distorted $LaVO_3$ has the Jahn-Teller distortion of the type *a* and more distorted YVO_3 shows the Jahn-Teller distortion of the type *d*. In the d^1 system, more distorted $YTiO_3$ is also accompanied by the Jahn-Teller distortion of the type *d*. In order to explain why the *d*-type Jahn-Teller distortion is realized in YVO_3, we have to assume that the $GdFeO_3$-type lattice distortion favors the Jahn-Teller distortion of the type *d*.

The magnetic moment at the V site is calculated to be ~ 1.8 μ_B for the *C*-type AFM state with the *a*-type Jahn-Teller distortion and the *G*-type AFM state with the *d*-type Jahn-Teller distortion. This value is in good agreement with the experimental value for the *G*-type AFM state in YVO_3 and is much larger than those observed for the *C*-type AFM states in YVO_3 and $LaVO_3$. In Fig. 5.5 (b), we have plotted the energy difference between the *C*-type and *G*-type AFM solutions and the magnetic moment of the two solutions as functions of the magnitude of the *d*-type Jahn-Teller distortion for ∠V-O-V ~ 139.3° As the Jahn-Teller distortion decreases, the energy difference between the *C*-type and *G*-type AFM states and the magnetic moment of the two solutions decrease. Without the Jahn-Teller distortion, the *C*-type AFM solution is lower in energy than the *G*-type AFM solution and the calculated magnetic moment is ~ 1.5 μ_B for the *C*-type AFM state, which is close to the experimental value for the *C*-type AFM states in YVO_3 and $LaVO_3$. This result suggests that the transition from the *G*-type AFM state to the *C*-type one in YVO_3 may be related to the reduction of the Jahn-Teller distortion.

In. Fig. 5.6, the density of state for the *C*-type and *G*-type AFM solutions is shown. The band gap opens between the occupied and unoccupied t_{2g} orbitals, the magnitude of which is mainly determined by $u' - j$. Character of the band gap is of the typical Mott-Hubbard type. From the HF calculation, the magnitudes of the band gaps for the *C*-type AFM and *G*-type AFM solutions are estimated to be ~ 3.3 eV and ~ 3.4 eV, respectively, which are by 1-2 eV larger than the experimental results [Arima *et al.*, 1993], indicating the limitation of the HF approximation. Recently, Sawada *et al.* [1995] have performed *ab-initio* band-structure calculations for YVO_3 and $LaVO_3$ using the generalized gradient approximation, which correctly predict the spin and orbital ordering for $LaVO_3$. In contrast to the present model HF result, the magnitude of the band gap is underestimated in the generalized-gradient-approximation calculation.

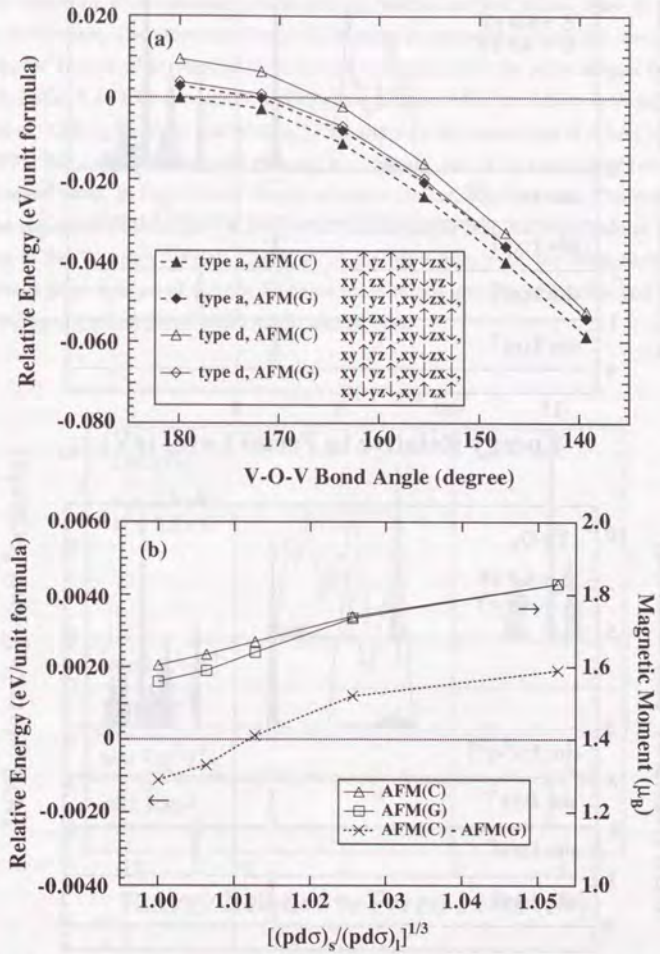

Fig. 5.5. (a) Total energies of various spin and orbital arrangements for RVO_3 as functions of the V-O-V bond angle. (b) Energy difference between the *C*-type and *G*-type AFM states and magnetic moment of the two states for RVO_3 as functions of the Jahn-Teller lattice distortion of the type *d*.

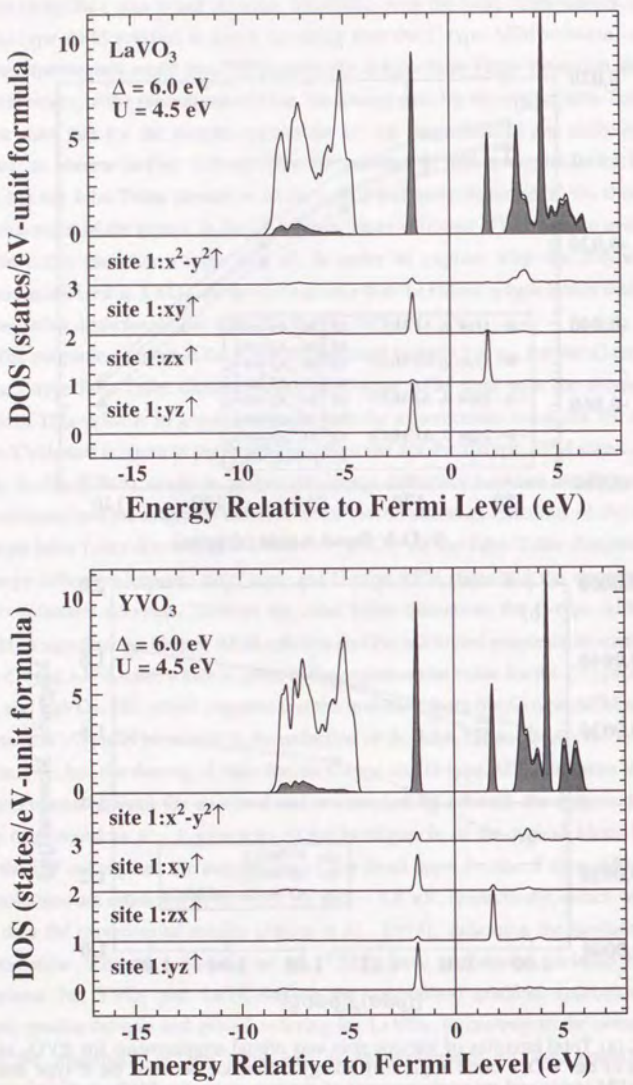

Fig. 5.6. Density of states for $LaVO_3$ and YVO_3.

5.3.3. d^3 compounds

In high-spin d^3 compounds, where the t_{2g} orbitals are half filled, there is no orbital degree of freedom. Therefore, the *G*-type AFM state is expected to have the lowest energy. Actually, the *G*-type AFM solution is the lowest in energy with the parameter set for $LaCrO_3$ listed in Table. 5.1. Experimentally, $LaCrO_3$ is a *G*-type AFM insulators with the magnetic moment of ~ 2.8 μ_B [Koehler and Wollan, 1957] and with the optical gap of ~ 3.5 eV [Arima *et al.*, 1993]. The calculated magnetic moment is ~ 3.0 μ_B and is in good agreement with the experimental value. In Fig. 5.7, the density of states for $LaCrO_3$ is shown. The magnitude of the band gap is calculated to be ~ 4.5 eV, which is also larger than the experimental value by ~ 1 eV as in the Ti and V oxides. Character of the band gap is of the Mott-Hubbard type. However, a large amount of oxygen 2*p* character is mixed into the 3*d* orbitals just above and below the band gap compared with $LaTiO_3$ and $LaVO_3$.

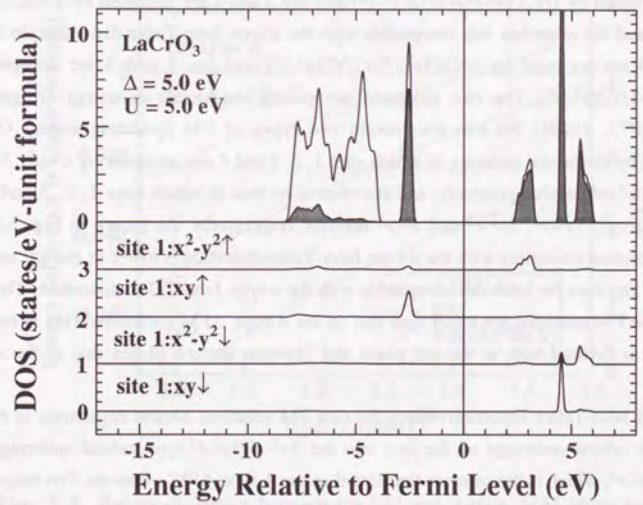

Fig. 5.7. Density of states for $LaCrO_3$.

5.3.4. d^4 compounds

In d^4 high-spin compounds, one of the e_g orbitals is occupied and there is also interesting interplay between the orbital ordering and the Jahn-Teller distortion. A Mn^{3+} perovskite-type oxide, $LaMnO_3$, is an *A*-type AFM insulator accompanied by a Jahn-Teller distortion of the type *d* [Wollan and Koehler, 1955; Goodenough, 1955; Matsumoto, 1970; Elemans *et al.*, 1971]. It is possible to estimate the effect of the Jahn-Teller distortion by scaling the transfer integrals with respect to the distance between the transition-metal ion and the oxygen ion. The magnitude of the Jahn-Teller distortion is represented by the ratio $(pd\sigma)_s/(pd\sigma)_l$, where $(pd\sigma)_s$ and $(pd\sigma)_l$ are transfer integrals for the shorter and longer Mn-O bonds, respectively.

Without the Jahn-Teller distortion, the HF calculation gives us two types of *A*-type AFM insulating solutions accompanied by the $3x^2$-$r^2/3y^2$-r^2-type orbital ordering with considerable mixture of $3z^2$-r^2, which can be regarded as a mixture of the $3x^2$-$r^2/3y^2$-r^2-type and z^2-x^2/z^2-y^2-type orbital orderings [Goodenough *et al.*, 1961; Kugel and Khomskii, 1973, 1982]. One has the orbital arrangement compatible with the *d*-type Jahn-Teller distortion, in which sites 1 and 3 are occupied by $1/\sqrt{2}(3z^2$-$r^2)+1/\sqrt{2}(x^2$-$y^2)$ and site 2 and 4 are occupied by $1/\sqrt{2}(3z^2$-$r^2)$-$1/\sqrt{2}(x^2$-$y^2)$, and the other has that compatible with the *a*-type Jahn-Teller distortion, in which sites 1 and 4 are occupied by $1/\sqrt{2}(3z^2$-$r^2)+1/\sqrt{2}(x^2$-$y^2)$ and site 2 and 3 are occupied by $1/\sqrt{2}(3z^2$-$r^2)$-$1/\sqrt{2}(x^2$-$y^2)$. The two solutions are exactly degenerate in energy [Kugel and Khomskii, 1973, 1982]. We can also obtain two types of FM insulating states. One is accompanied by the orbital ordering in which sites 1, 2, 3 and 4 are occupied by z^2-y^2, $3x^2$-r^2, $3y^2$-r^2 and z^2-x^2 orbitals, respectively, and the other is by that in which sites 1, 2, 3 and 4 are occupied by z^2-y^2, $3x^2$-r^2, $3x^2$-r^2 and z^2-y^2 orbitals, respectively. As shown in Fig. 5.8, the former FM solution consistent with the *d*-type Jahn-Teller distortion is lower in energy and has a larger band gap than the latter one compatible with the *a*-type Jahn-Teller distortion. The total energies of the FM solutions are lower than that of the *A*-type AFM solutions. This is because FM coupling is favored both in the *a*-*b* plane and between the *a*-*b* planes due to the orbital ordering.

A small Jahn-Teller distortion makes the two FM solutions almost degenerate in energy and turns the orbital orderings of the two into the $3x^2$-$r^2/3y^2$-r^2-type orbital ordering with mixture of $3z^2$-r^2, which is the same as that found in the *A*-type AFM solutions. The magnitude of the band gap for the FM solution compatible with the *d*-type Jahn-Teller distortion is reduced and becomes almost equal to that for the FM solution compatible with the *a*-type Jahn-Teller distortion as shown in Fig. 5.8. Although the energy difference between the FM and A-type AFM solutions becomes smaller, the FM solutions are still lower in energy than the *A*-type AFM solutions.

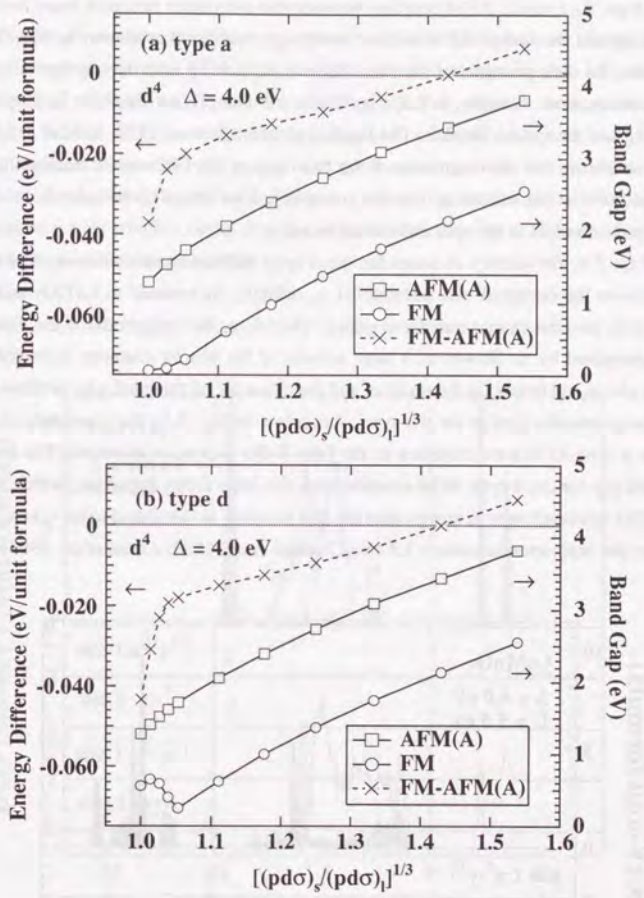

Fig. 5.8. Energy difference between the FM and *A*-type AFM states and band gaps of the FM and *A*-type AFM states for $LaMnO_3$ as a function of the Jahn-Teller lattice distortion (a) of the type *a* and (b) of the type *d*.

As the Jahn-Teller distortion increases, the orbital ordering becomes purely of the $3x^2$-$r^2/3y^2$-r^2-type. As a result, AFM coupling between the a-b planes becomes more favored than FM coupling and the A-type AFM solution is strongly stabilized as shown in Fig. 5.8. This indicates that the disappearance of the Jahn-Teller distortion by hole doping turn A-type AFM into FM arrangement. Actually, in $La_{1-x}Sr_xMnO_3$, the Jahn-Teller distortion is suppressed by hole doping and the system becomes FM [Jonker and van Santen, 1950; Tokura *et al.*, 1994]. Fig. 5.8 also shows that the magnitude of the band gap of the FM state is smaller than that of the A-type AFM state, indicating that the metallization in $La_{1-x}Sr_xMnO_3$ by hole doping is favored by the changes in the spin and orbital ordering.

In Fig. 5.9, the density of states for the A-type AFM solution is shown. The band gap opens between the occupied and unoccupied e_g orbitals. In contrast to $LaTiO_3$ and $LaVO_3$, $LaMnO_3$ falls into the charge-transfer regimes. Therefore, the magnitude of the band gap is mainly determined by Δ. However, a large amount of the Mn $3d$ character is mixed into the states just above and below the Fermi level and the character of the band gap deviates from the typical charge-transfer type or the p-d type. As shown in Fig. 5.8, the magnitude of the band gap of the A-type AFM state increases as the Jahn-Teller distortion increases. The magnitudes of the band gap for the A-type AFM solution with the Jahn-Teller distortion, which makes the A-type AFM solution lower in energy than the FM solution, is calculated to be ~ 3 eV, which is larger than the experimental value ~ 1.3 eV [Chainani *et al.*, 1993; Arima *et al.*, 1993].

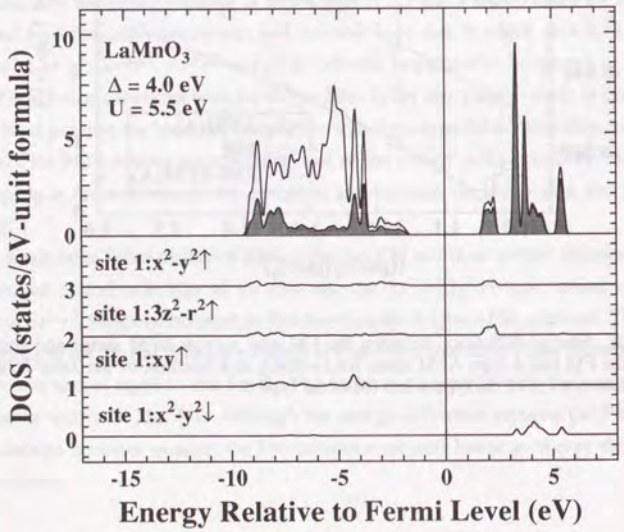

Fig. 5.9. Density of states for $LaMnO_3$. $[(pd\sigma)_s/(pd\sigma)_l]^{1/3} = 1.43$.

5.3.5. d^5 compounds

High-spin d^5 compounds, where t_{2g} orbitals are half filled, has no orbital degree of freedom. Therefore, G-type AFM state has the lowest energy in the HF calculation. Experimentally, $LaFeO_3$ is a G-type AFM insulators with the magnetic moment of ~ 4.6 μ_B [Koehler and Wollan, 1957] and with the optical gap of ~ 2.5 eV [Arima *et al.*, 1993]. The calculated magnetic moment is ~ 4.6 μ_B and is in good agreement with the experimental value. In Fig. 5.10, the density of states for $LaFeO_3$ is shown. The magnitude of the band gap is estimated to be ~ 4 eV which is larger than the experimental value by ~ 1.5 eV. The character of the band gap is of the charge-transfer type.

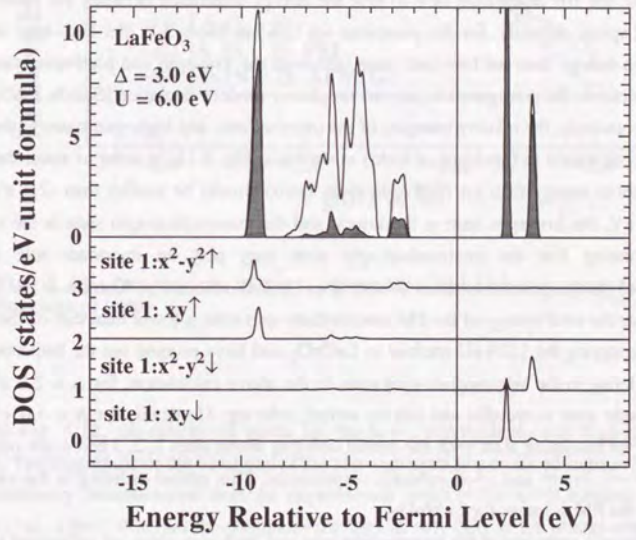

Fig. 5.10. Density of states for $LaFeO_3$.

5.3.6. d^6 compounds

$LaCoO_3$ is a nonmagnetic insulator, where the t_{2g} orbitals are fully occupied, which has no orbital degree of freedom. However, the magnetic susceptibility studies of $LaCoO_3$ indicate that the nonmagnetic-to-paramegnetic transition occurs at ~ 90 K [Jonker and van Santen 1953; Raccah and Goodenough, 1967], which can be regarded as a transition from the low-spin $t_{2g}\uparrow^3 t_{2g}\downarrow^3$ configuration to the intermediate-spin $t_{2g}\uparrow^3 t_{2g}\downarrow^2 e_g\uparrow$ or high-spin $t_{2g}\uparrow^3 t_{2g}\downarrow e_g\uparrow^2$ configurations. Therefore, it is interesting to study the effect of orbital ordering in the intermediate- and high-spin states. For the intermediate-spin and high-spin states, a FM metallic and *G*-type AFM insulating solutions are the lowest in energy, respectively, according to the HF calculation. The low-spin state, where the e_g orbitals are mixed into the t_{2g} orbitals through the *j*' term, is lower in energy by ~ 0.15 eV per formula unit cell than that without the t_{2g}- e_g mixing. However, since the energy gain due to the *j*' term is underestimated in the HF approximation, the HF calculation fails to give the energy difference between the states with different total spins. Actually, for the parameter set listed in Table 5.1, the high-spin state is much lower in energy than the low-spin state, although the low-spin and high-spin states are almost degenerate in the configuration-interaction cluster-model calculation [Saitoh, 1995].

Here, tentatively, the relative energies of the intermediate- and high-spin states to the low-spin state are calculated as functions of ($pd\sigma$) as shown in Fig. 5.11. In order to make the low-spin state lower in energy than the high-spin state, ($pd\sigma$) should be smaller than -2.3 eV. For ($pd\sigma$) < -2.3 eV, the low-spin state is the lowest and the intermediate-spin state is the second lowest, suggesting that the intermediate-spin state may play an important role in the nonmagnetic-to-paramagnetic transition observed in $LaCoO_3$. Recently, Korotin *et al.* [1995] have found that the total energy of the FM intermediate-spin state is lower than that of the high-spin state by applying the LDA+U method to $LaCoO_3$ and have pointed out the importance of the orbital ordering in the intermediate-spin state. In the above calculation, for Δ = 2.0 eV, the intermediate-spin state is metallic and has no orbital ordering. However, for Δ = 3.0 eV, we can obtain a FM insulating state with the orbital ordering where sites 1, 2, 3 and 4 are occupied by z^2-y^2, $3x^2$-r^2, $3y^2$-r^2 and z^2-x^2 orbitals, respectively. This orbital ordering is the same as that found in the FM solution for $LaMnO_3$.

The magnetic moments of the intermediate-spin and high-spin states are calculated to be ~ 2.2 μ_B and ~ 3.5 μ_B, respectively. Since the magnetic moment observed in the FM metallic $La_{1-x}Sr_xCoO_3$ is ~ 1 - 2 μ_B [Jonker and van Santen, 1953; Raccah and Goodenough, 1967], the intermediate-spin FM solution may also be closely related to the FM metallic state in the $La_{1-x}Sr_xCoO_3$ system.

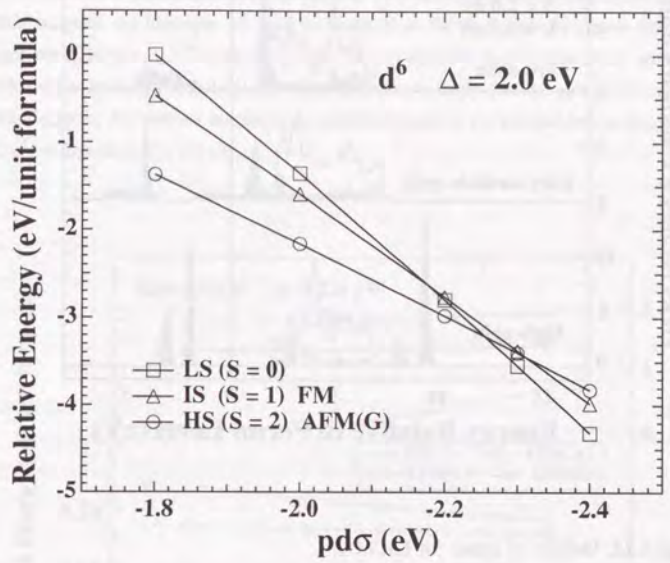

Fig. 5.11. Total energies of low-, intermediate- and high-spin states for $LaCoO_3$ as functions of ($pd\sigma$).

In Fig. 5.12, the density of states for the low-, intermediate- and high-spin states are shown. The magnitude of the band gap of the low-spin state is calculated to be ~ 3.5 eV, which is considerably overestimated than the experimental result ~ 0.6 eV [Chainani *et al.*, 1993; Arima *et al.*, 1993]. Whereas the parameter set for $LaCoO_3$ falls in the charge-transfer regime, in the states just below the Fermi level, the Co 3*d* and O 2*p* orbitals are strongly hybridized. On the other hand, the character of the band gap for the high-spin state is of the typical charge-transfer type. The density states for the low-, intermediate- and high-spin states are quite different. Therefore, it may be interesting to compare the three calculated result with the photoemission and inverse-photoemission spectra of $LaCoO_3$ and $La_{1-x}Sr_xCoO_3$ [Saitoh, 1995].

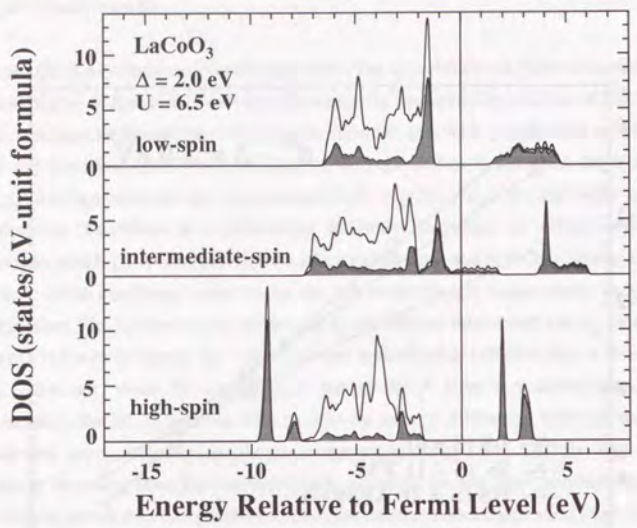

Fig. 5.12. Density of states for $LaCoO_3$.

5.3.7. d^7 compounds

In the Ni^{3+} (low-spin d^7) perovskite-type oxides, the least distorted $LaNiO_3$ is a PM metal and the more distorted $RNiO_3$ with the R ion smaller than La is an AFM insulator [Torrance *et al.*, 1992]. $PrNiO_3$ and $NdNiO_3$, show unusual magnetic structures, where each Ni ion is ferromagnetically coupled to three nearest neighbors and antiferromagnetically coupled to the other three [García-Muñoz *et al.*, 1992b, 1994]. In order to explain this magnetic structure, it has been proposed that the e_g orbitals are polarized into $3z^2$-r^2 and x^2-y^2 for the ferromagnetically coupled Ni pairs and are polarized into the same orbitals for the antiferromagnetically coupled Ni pairs [García-Muñoz *et al.*, 1992b, 1994]. Because the actual magnetic unit cell of $PrNiO_3$ is four-times larger than that of the $GdFeO_3$-type structure, we have only studied the simplified spin- and orbital-ordered structures shown in Fig. 5.2. The actual magnetic structure of $PrNiO_3$ can be viewed as a mixture of these four magnetic structures and hence calculations on these structures will give insight into the actual spin and orbital ordering. Here, we note that for Δ = 1.0 eV the high-spin AFM insulating state is the lowest and the low-spin FM metallic state is the second lowest, incompatible with experiment.

This would be due to the lack of "Heitler-London-type" or ($\uparrow\downarrow$–$\downarrow\uparrow$)-type electron correlation between the $3d$ electron and the oxygen $2p$ hole with antiparalell spins in the HF ground state. Indeed, in the cluster calculation, where electron correlation within the NiO_6 cluster is fully taken into account, the low-spin ^2E state is lower than the high-spin $^4T_1$ state for the same parameter set [Chapter 3]. For larger $\Delta >\sim$ 2.0 eV, the low-spin states exist as insulating metastable states in the HF band calculations. In order to study the changes in the magnitudes of the band gap for the various magnetic structures, therefore, we present below the results for Δ = 2.0 eV rather than Δ = 1.0 eV.

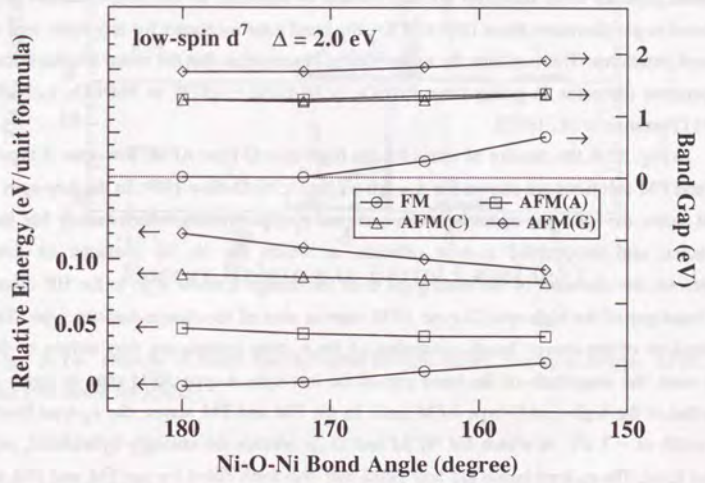

Fig. 5.13. Total energies and band gaps of various spin and orbital arrangement for $RNiO_3$ system as a function of Ni-O-Ni bond angle.

In the low-spin d^7 systems, the t_{2g} orbitals mix with the e_g orbitals through the off-diagonal Coulomb j' term. Therefore, Jahn-Teller distortion does not stabilize the A-type AFM solution significantly unlike the d^4 high-spin system. We denote the e_g orbitals which have mixtures of t_{2g} orbitals as "$3z^2$-r^2" and "x^2-y^2". The FM and C-type AFM solutions, which have FM coupling along the c-axis, favors the "$3z^2$-r^2"/"x^2-y^2"-type orbital ordering. In the FM solution, sites 1, 2, 3 and 4 are occupied by "z^2-y^2", "$3x^2$-r^2", "$3y^2$-r^2" and "z^2-x^2" orbitals. This orbital ordering is similar to that obtained in the FM state for $LaMnO_3$. In the C-

type AFM solution, sites 1, 2, 3 and 4 are occupied by "x^2-y^2", "x^2-y^2", "$3z^2$-r^2" and "$3z^2$-r^2" orbitals. On the other hand, the *A*-type and *G*-type AFM solutions have the "$3x^2$-r^2"/"$3y^2$-r^2"-type orbital ordering. Namely, in the *A*-type and *G*-type AFM solutions, the sites 1, 2, 3 and 4 are occupied by "$3y^2$-r^2", "$3x^2$-r^2", "$3y^2$-r^2" and "$3x^2$-r^2" orbitals into which "$3z^2$-r^2" is mixed. This orbital ordering is essentially the same as that found in the *A*-type AFM solution for $LaMnO_3$. The total energies of the various solutions for $\Delta = 2.0$ eV are plotted in Fig. 5.13 as functions of the Ni-O-Ni bond angle. The FM solution and the *A*-type AFM solution are very close in energy to each other, suggesting that the complicated magnetic structures, where both the FM coupling and AFM coupling coexist and the FM coupling within the *a*-*b* plane and that between the *a*-*b* planes are competing, may be realized in these compounds. In Fig. 5.13, the band gaps for these solutions are also plotted as functions of the Ni-O-Ni bond angle. As the bond angle decreases from 160° to 150°, the band gaps increases for any spin- and orbital-ordered structures. This explains the experimental observation that the metal-insulator transition temperature increases in going from $PrNiO_3$ ($\angle$Ni-O-Ni ~ 157°) to $NdNiO_3$ ($\angle$Ni-O-Ni ~ 156°) [Torrance *et al.*, 1992].

In Fig. 5.14, the density of states for the high-spin *G*-type AFM, low-spin *A*-type AFM, FM and PM solutions are shown for $\Delta = 1.0$ eV and $\angle$Ni-O-Ni = 180°. In the low-spin *A*-type AFM states, the band gap opens between occupied e_g-type orbitals, which mainly has the O 2*p* character, and unoccupied e_g-type orbitals, in which the Ni 3*d* character is dominant. Therefore, the character of the band gaps is of the charge-transfer type in the HF calculation. The band gap of the high-spin *G*-type AFM state is also of the charge-transfer type. Since the dispersions of the energy bands consisting of the e_g-type orbitals are very strong in the low-spin state, the magnitude of the band gap of the low-spin *A*-type AFM state is much smaller than that of the high-spin *G*-type AFM state. In the FM and PM states, the e_g-type bands with the width of ~ 3 eV, in which the Ni 3*d* and O 2*p* orbitals are strongly hybridized, cross the Fermi level. The e_g-type bands are half filled and one-forth filled for the FM and PM solution respectively. As mentioned above, the FM metallic state is the second lowest among the four solutions and the PM metallic state is much higher in energy than the FM state. However, experimentally, the metal-insulator transition of $RNiO_3$ system as a function of the size of the *R* ion is that from a PM metal to an AFM insulator and there is no region in which a FM metallic state is realized [Torrance *et al.*, 1992]. This discrepancy is considered to be due to the lack of spin and orbital fluctuation in the HF approximation. The energy of the PM metallic state may significantly be lowered by inclusion of the spin and orbital fluctuation beyond the HF approximation compared with the other spin and orbital ordered states.

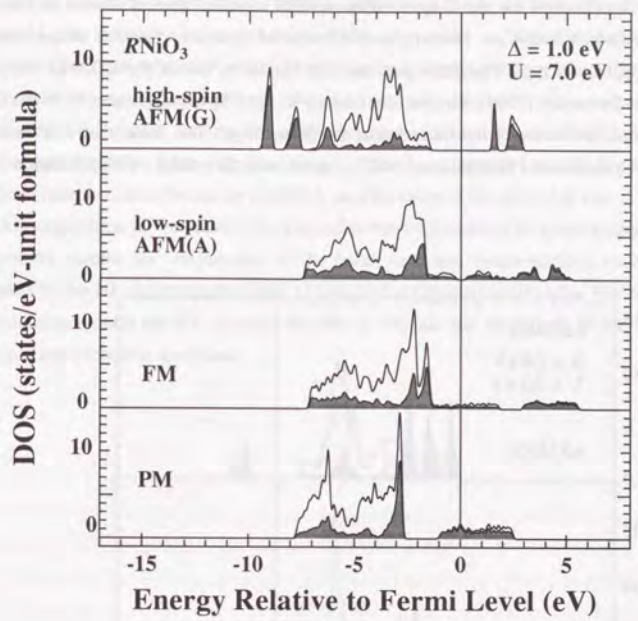

Fig. 5.14. Density of states for high-spin *G*-type AFM, low-spin *A*-type AFM, FM and PM states for $RNiO_3$.

5.3.8. d^8 compounds

In high-spin d^8 compounds, where the t_{2g} orbitals are fully occupied and the e_g orbitals are half filled, there is no orbital degree of freedom. Therefore, the *G*-type AFM state is the lowest in energy in the HF calculation. This result is consistent with the LDA+U calculation by Czyzyk and Sawatzky [1994] which predict tetragonally-distorted $LaCuO_3$ as an insulator with the *G*-type AFM ordering. However, experimentally, rhombohedrally-distorted $LaCuO_3$ is a PM metal and tetragonally-distorted $LaCuO_3$ also shows metallic behavior [Demazeau *et al.*, 1972, Bringly *et al.*, 1993]. As mentioned in the previous section, the HF calculation fails to describe the PM metallic state near the metal-insulator transition. The energy of the PM metallic state may significantly be lowered by the correlation effect beyond the HF approximation compared with the *G*-type AFM state.

The density of states for the *G*-type AFM and PM metallic states is shown in Fig. 5.15 for $\Delta = 0.0$ eV and $\angle$Cu-O-Cu = 180°. In the *G*-type AFM state, the character of the band gap is of the charge-transfer type. The density of states is similar to that of the LDA+U calculation by Czyzyk and Sawatzky [1994]. On the other hand, in the PM metallic state, both the Cu 3*d* and O 2*p* orbitals are strongly hybridized near the Fermi level. The density of state is similar to that of LDA calculation [Takegahara, 1987; Czyzyk and Sawatzky, 1994; Hamada *et al.*, 1995].

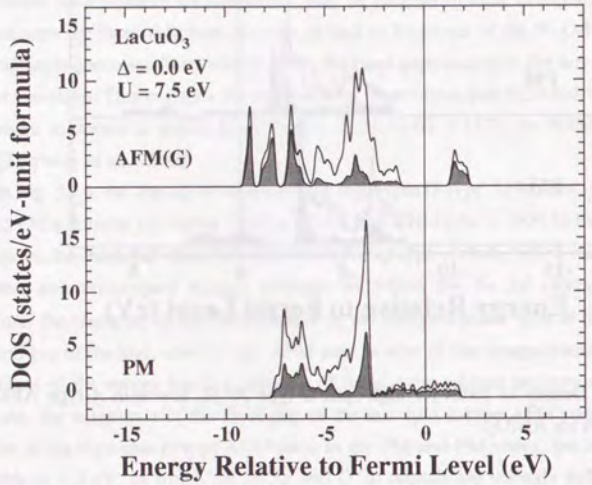

Fig. 5.15. Density of states for *G*-type AFM and PM states for $LaCuO_3$.

5.4. Conclusion

The spin- and orbital- unrestricted HF calculation can explain the various magnetic and electronic properties of perovskite-type 3*d* transition-metal oxides, which are originated from the 10-fold degeneracy or the spin and orbital degrees of freedom of the 3*d* orbitals. The HF calculations have revealed the interesting interplay between the orbital and spin ordering in the perovskite-type 3*d* transition-metal oxides with the partially filled t_{2g} or e_g orbital. It has also been found that the orbital ordered states are strongly affected by the Jahn-Teller distortion and $GdFeO_3$-type distortion. FM and *C*-type AFM solutions with orbital ordering are stabilized by

the Jahn-Teller distortion in d^1 and d^2 compounds respectively. In high-spin d^4 compounds, while a FM state is favored without the Jahn-Teller distortion, the Jahn-Teller distortion makes an *A*-type AFM state with $3x^2$-r^2/$3y^2$-r^2-type orbital ordering lower in energy than the FM state. For the low-spin d^7 compounds, the observed magnetic structure is so complicated that the present HF calculation cannot give a clear description. However, in the HF calculation, the $GdFeO_3$-type distortion makes the magnitude of the band gap larger, which can explain the metallic versus insulating behavior of $RNiO_3$ as a function of the size of *R* ion.

Although these HF results for the ground states are generally in good agreement with the experimental results, the magnitudes of the band gaps and single-particle excitation spectra calculated by the HF approximation fails to explain the experimental results. We should include the fluctuation around the HF solution in order to explain the magnitude of the band gap and single-particle excitation spectrum.

Chapter six

Self-energy correction to unrestricted Hartree-Fock solutions of lattice models for 3*d* transition-metal oxides

In order to explain the excitation properties of 3*d* transition-metal oxides in a unified framework, we have performed second-order perturbation calculations of the self-energy corrections around the unrestricted Hartree-Fock solution of lattice models using the electronic-structure parameters deduced from photoemission spectroscopy. The self-energy modifies the magnitude of the band gap and causes substantial spectral weight transfer over a wide energy range both in insulating and metallic compounds of the Mott-Hubbard type as well as of the charge-transfer type, resulting in considerably improved agreement between theory and experiment.

6.1. Introduction

In these decades, many researchers have been fascinated by 3*d* transition-metal oxides, where a partially filled 3*d* band causes various magnetic and electrical properties [Mott, 1990; Tsuda *et al.*, 1990]. While many of them are antiferromagnetic (AFM) insulators (MnO, NiO, $LaTiO_3$, etc.), some of them exist as paramagnetic (PM) metals (TiO, VO, $SrVO_3$, $LaNiO_3$, etc.) or nonmagnetic insulators ($LaCoO_3$, $NaCuO_2$, etc.). It is well-known that conventional one-electron band-structure calculations fail to predict the AFM insulating states and that strong correlation between the 3*d* electrons is essential to the insulating behavior [de Boer and Verwey, 1937]. Photoemission spectra of these oxides have successfully been analyzed using cluster models or Anderson-impurity models [Fujimori and Minami, 1984; Zaanen, 1986] and their electronic structures have been interpreted in terms of the Zaanen-Sawatzky-Allen (ZSA) scheme [Zaanen *et al.*, 1985; Hüfner, 1985], according to which transition-metal compounds are classified into two regimes, namely, the Mott-Hubbard regime, where the *d*-*d* Coulomb interaction U is smaller than oxygen 2*p*-to-transition-metal 3*d* charge-transfer energy Δ, and the charge-transfer regime where Δ is smaller than U.

Meanwhile, many band-theoretical attempts using the local-(spin-)density approximation [L(S)DA] have been made to describe the insulating behavior of the 3*d* transition-metal oxides from first principles. It has been shown that LSDA calculations with actual magnetic structures can give a finite band gap for NiO and MnO [Terakura *et al.*, 1984] and that the orbital-polarized LSDA can predict the insulating behavior of CoO [Norman, 1991]. However, these calculations considerably underestimate the magnitudes of the band gaps because the L(S)DA suffers from the self-interaction problem. Svane and Gunnarsson [1990] and Arai and Fujiwara [1995] have shown that the self-interaction correction (SIC) to the L(S)DA improves agreement for the magnitudes of the band gaps between theory and experiment. The LDA+U method, which has been proposed by Anisimov, Zaanen and Andersen [1991], has also been successfully applied to many 3*d* transition-metal oxides. *Ab-initio* Hartree-Fock (HF) calculations on $CaCuO_2$ [Massida *et al.*, 1992] and NiO [Towler *et al.*, 1994], which do not suffer from the self-interaction, also give the insulating behaviors like the SIC-LDA and LDA+U methods although the magnitude of the band gaps are overestimated. In the LDA+U, SIC-LDA and HF calculations for typical charge-transfer insulators, the occupied 3*d* band is lowered below the oxygen 2*p* band and the character of the band gap is correctly predicted to be of the charge-transfer type or the *p*-*d* type. However, single-particle spectral functions obtained from these calculations disagree with the photoemission spectra in that the satellite structure has a too low binding energy and its intensity is too strong. For a PM metallic state, the LDA+U, SIC-LDA and HF calculations are almost equivalent to the LDA and fail to give a satellite structure which has been observed in some PM transition-metal oxides [Fujimori *et al.*, 1992a; Eisaki, 1992; Inoue *et al.*, 1995; Morikawa *et al.*, 1995].

In order to explain the single-particle spectral functions of 3*d* transition-metal oxides, one has to include electron correlation effects, which have been neglected in the band-structure calculations and are to be included as a self-energy correction to the HF or LDA solutions. There have been some attempts of *ab-initio* calculations of the self-energy using GW approximation [Massida *et al.*, 1992, 1995; Aryasetiawan and Gunnarsson, 1995]. However, since *ab-initio* calculations of the self-energy needs prohibitively large computational time, it is difficult to apply it to many compounds systematicaly. In order to investigate the effect of the self-energy correction in compounds with various ground states, one can alternatively perform HF and subsequent self-energy calculation on a realistic tight-binding model using parameters deduced from the cluster-model analysis of photoemission spectra. The model HF calculations have correctly predicted the magnetic and orbital orderings in perovskite-type 3*d* transition-metal oxides and their effect as well as the effect of lattice distortions on the magnitude of the band gaps [Mizokawa and Fujimori, 1995; Chapter 5]. However, single-particle spectral functions obtained from the model HF calculations for charge-transfer insulators disagree with the experimental results in the same way as in the *ab-initio* LDA+U and SIC-LDA calculations. The model HF calculations also tends to overestimate the magnitudes of the band gaps, especially in Mott-Hubbard-type insulators. It is expected that, once we have found a HF solution which has the same symmetry as the real system, we can approach the exact description of both the ground state and the single-particle excitation spectra by perturbation expansion in the interaction term as in the perturbation calculation around the nonmagnetic HF solution of the Kondo problem [Yamada and Yoshida, 1970, 1975].

6.2. Self-energy calculation using local approach

In this section, we have performed second-order perturbation calculations of the self-energy correction using the so-called local approximation [Treglia *et al.*, 1980, 1982; Steiner *et al.*, 1991, 1992] in order to explain the single-particle spectra of 3*d* transition-metal oxides with various types of ground states: An AFM insulator NiO of the charge-transfer type, a ferromagnetic insulator $YTiO_3$ of the Mott-Hubbard type, a nonmagnetic insulator $LaCoO_3$ and a PM metal $SrVO_3$. We have employed a multiband *d*-*p* model, where we have included the full degeneracy of the transition-metal 3*d* and oxygen 2*p* orbitals. Hybridization terms between 3*d* and 2*p* are expressed in terms of Slater-Koster parameters ($pd\sigma$), ($pd\pi$), ($pp\sigma$) and ($pp\pi$) [Slater and Koster, 1954]. The ratio ($pd\sigma$)/($pd\pi$) is fixed at ~ -2.2 and ($pp\sigma$) and ($pp\pi$) are fixed at 0.60 eV and 0.15 eV, respectively [Mattheiss, 1972]. The intra-atomic Coulomb terms are given by Kanamori parameters u, u', j, j', where the relationships $u' = u - 2j$ and $j' = j$ is assumed in order to retain the rotational invariance of the interaction term [Kanamori, 1963]. The Kanamori parameters can be deduced from Racah parameters through $u = A + 4B + 3C$ and $j = (5/2)B + C$, where B and C have been fixed to the free-ion values [Sugano *et al.*, 1970].

The multiplet-averaged *d-d* Coulomb interaction U (= A -14/9B +7/9C) and the charge-transfer energy Δ for the d^n configuration are given by u - (20/9)j and ε_d^0 - ε_p + nU, respectively, where ε_d^0 and ε_p are the bare energy levels of the 3*d* and 2*p* orbitals. The three adjustable parameters, Δ, U and ($pd\sigma$) have been deduced from cluster-model analyses of photoemission spectra.

We have calculated the 3*d* components of the self-energy $\Sigma_{mm'}(\omega)$ to second order in u, u', j and j' using the local approximation [Treglia *et al.*, 1980, 1982; Steiner *et al.*, 1991, 1992]. The self-energy of a Bloch orbital in the HF solution is given by $\alpha_m\alpha_{m'}\Sigma_{mm'}(\omega)$, where α_m is the weight of the m-th 3*d* orbital in the Bloch orbital. The momentum dependence of the self-energy is included only through the momentum dependence of the α_m. For a metallic solution, the Fermi level has to be self-consistently redefined after the inclusion of the self-energy so as to keep the imaginary part of the self-energy to be zero at the Fermi level [Calandra and Manghi, 1992]. 512 k points were sampled in the first Brillouine zone for the distorted perovskite ($GdFeO_3$-type) and rock-salt-type structures. The energy meshes are 0.1 eV for insulating solutions and 0.05 eV for metallic solutions, which are small enough to calculate the density of states with required accuracy.

6.2.1. NiO

NiO (d^8) is a typical charge-transfer-type insulator and the values of Δ, U and ($pd\sigma$) have been estimated to be 4.0, 7.0 and -1.4 eV, respectively [Fujimori and Minami, 1984; Hüfner *et al.*, 1984; van Elp, 1991]. As shown in Fig. 1, the HF calculation reproduces the magnitude of the band gap ~ 4 eV. However, the same calculation fails to reproduce the satellite structure in the photoemission spectra in that the calculated lower Hubbard band of almost pure Ni 3*d* character has too small binding energy (~ -8 eV) and is too sharp and strong. The shape of the main-band region ranging from 0 eV to -6 eV also deviates from the experimental result in that it has too small *d* spectral weight near the top of the valence band. The self-energy correction improves agreement with the photoemission spectra in the satellite region. Part of the *d* spectral weight of the lower Hubbard band is transferred towards lower energy, -8 to -15 eV, forming the satellite structure. The remaining part is shifted towards higher energy (-1 to -5 eV) and increases the *d* character near the top of the main-band region. As a result, agreement with the observed photoemission spectra both in the position of the satellite structure and in the shape of the main-band region has been improved. However the calculated satellite structure is too broad in comparison with the observed satellite peak. In order to correctly reproduce the width of the satellite peak, higher-order terms would be needed. On the other hand, the magnitude of the band gap is only slightly reduced by the self-energy correction, in agreement with the experimental band gap. The charge-transfer or *p-d* character of the band gap is also maintained.

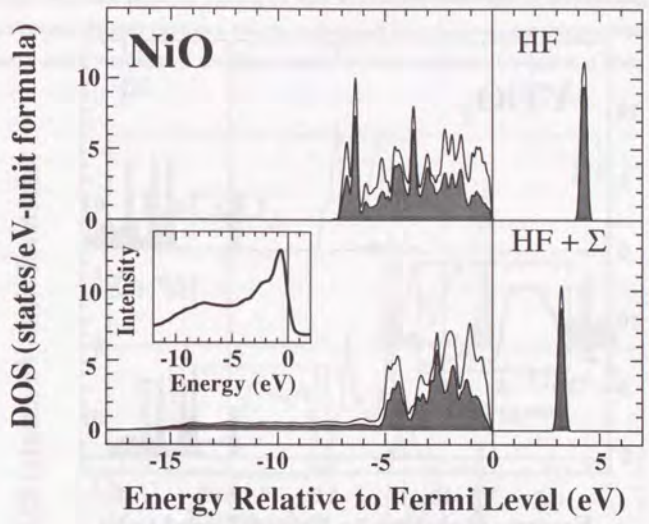

Fig. 6.1. Spectral function of NiO calculated using the HF approximation (upper panel) and that including the self-energy correction calculated using the second-order perturbation (lower panel). The shaded area indicates the transition-metal 3*d* spectral weight. The inset shows the photoemission spectrum of NiO taken at $h\nu$ = 1486.6 eV [van Elp, 1991].

6.2.2. $YTiO_3$

As a typical Mott-Hubbard-type insulator, we have studied $RTiO_3$ (R = rare earth), which has the d^1 configuration. The magnitude of the band gap of $RTiO_3$ tends to be overestimated in the HF calculation. For example, while a ferromagnetic insulator $YTiO_3$ has a band gap of ~ 1 eV [Arima *et al.*, 1993], it is predicted to be ~ 3 eV in the HF calculation using a realistic parameter set, Δ = 7.0 eV, U = 4.0 eV and ($pd\sigma$) = -2.2 eV [Bocquet *et al.*, 1995] as shown in the upper panel of Fig. 6.1. The self-energy correction in this region is found quite large because the states just above and below the band gap are dominated by 3*d* character. Both the occupied (lower Hubbard) and unoccupied 3*d* (upper Hubbard) bands are shifted towards the Fermi level, reducing the band gap from the HF values to ~ 1 eV as shown in Fig. 6.2. On the other hand, the position of the O 2*p* band, which is already in good agreement with the experimental result [Morikawa *et al.*, 1995] within the HF approximation, is hardly affected by the self-energy correction.

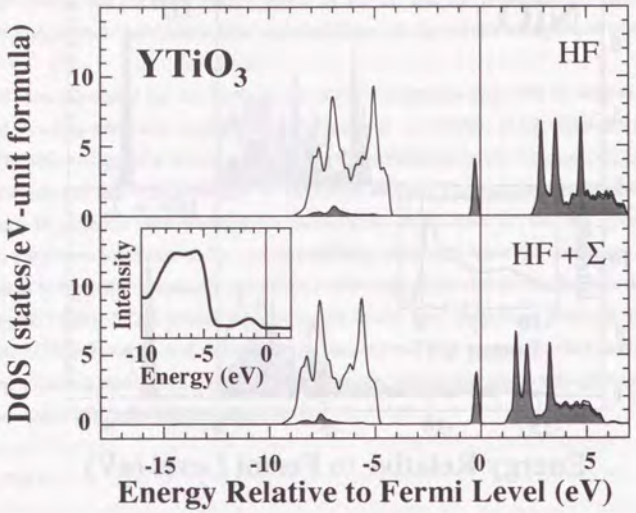

Fig. 6.2. Spectral function of $YTiO_3$. The same as Fig. 6.1. The inset shows the photoemission spectrum of $YTiO_3$ taken at $h\nu$ = 21.2 eV [Morikawa, 1995].

6.2.3. $LaCoO_3$

For a nonmagnetic insulator $RCoO_3$ (d^6), where the t_{2g} band is fully occupied and the e_g band is empty, the HF approximation gives an insulating solution without spin nor orbital ordering, implying that $RCoO_3$ is nothing but a band insulator. However, the magnitude of the band gap is ~ 3 eV in the HF calculation using the values of Δ, U and ($pd\sigma$) (2.0, 6.5 and -1.8 eV, respectively) estimated from the cluster-model analysis of the photoemission spectra [Abbate *et al.*, 1993; Saitoh *et al.*, 1995b], which is much larger than the experimental value of 0.6 eV [Chainani *et al.*, 1992]. The self-energy correction drastically reduces the magnitude of the band gap from the HF value to ~ 0.5 eV (see Fig. 6.3) in contrast to NiO. As for the single-particle spectra, too, agreement between the HF calculation and the experimental result is not good and is improved by the self-energy correction as shown in the lower panel of Fig. 6.3. The experimentally observed broad satellite structure ranging from -8 eV to -13 eV [Abbate *et al.*, 1993] is reproduced by the second-order perturbation. An interesting question is to what extent the wave function of the ground state becomes closer to that of a local-singlet (of the $d^7\underline{L}$

configuration in the cluster language) by the perturbation calculation. A quantitative investigation of this point in $RCoO_3$ as well as in other nonmagnetic and insulating transition-metal compounds may give us a clue to understand the relationship between these nonmagnetic transition-metal compounds and the so-called Kondo insulators [Appeli and Fisk, 1992].

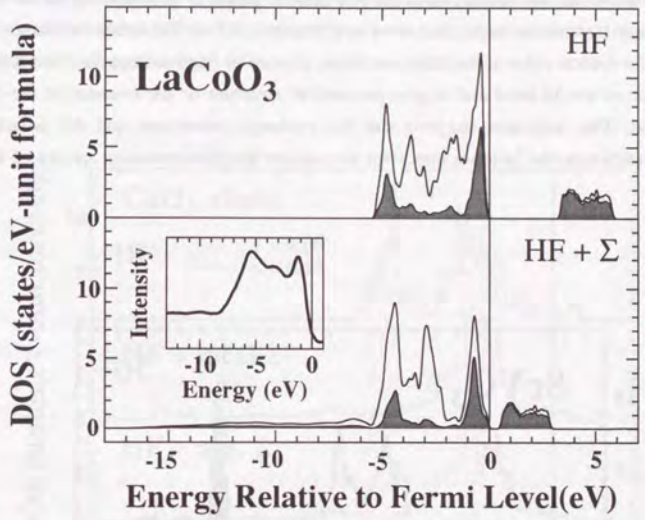

Fig. 6.3. Spectral function of $LaCoO_3$. The same as Fig. 6.1. The inset shows the photoemission spectrum of $LaCoO_3$ taken at $h\nu$ = 1486.6 eV [Abbate *et al.*, 1993].

6.2.4. $SrVO_3$

In the photoemission spectra of PM metals such as $SrVO_3$ and $CaVO_3$ (d^1), a remnant of the lower Hubbard band, which can be viewed as a sort of satellite structure, has been observed at ~ 1.5 eV below the Fermi level [Fujimori *et al.*, 1992a; Eisaki, 1992; Inoue *et al.*, 1995; Morikawa *et al.*, 1995]. Calculations on the infinite-dimension single-band Hubbard model reproduce such satellite structure at half filling [Müller-Hartmann, 1989a, 1989b; Georges and Kotliar, 1992; Jarrell, 1992]. However, since one-sixth of each triply-degenerate t_{2g} band is occupied in $SrVO_3$ and $CaVO_3$, we cannot directly compare the result of the single-band model with the photoemission spectra. In Fig. 6.4, the HF and self-energy corrected results for $SrVO_3$ are displayed [for Δ = 4.0 eV, U = 3.0 eV and ($pd\sigma$) = -2.2 eV]. The result of the HF

calculation is essentially the same as that of the LDA band structure calculation for the PM solution, in which one-sixth of the t_{2g} band is occupied. The second-order self-energy strongly renormalizes the t_{2g} band and gives a narrow quasi-particle band at Fermi level and a satellite structure at ~ 1 eV below the Fermi level, which may correspond to the -1.5 eV peak in the photoemission spectra. In the present model, the band gap of the d^1 system is determined by $u' - j$, while the d-d Coulomb interaction in the PM metallic phase is governed by the averaged Coulomb energy U, which is larger than $u' - j$ by $(7/9)j$ (~ 0.5 eV). Therefore, although $u' - j$ is lower than the critical value of the Mott transition, U may be large enough to cause a strong renormalization of the 3d band and to give the satellite structure or the remnant of the lower Hubbard band. This argument suggests that the exchange interaction and the anisotropic Coulomb interaction on the 3d ion is important to consider the photoemission spectra of the d^1 system.

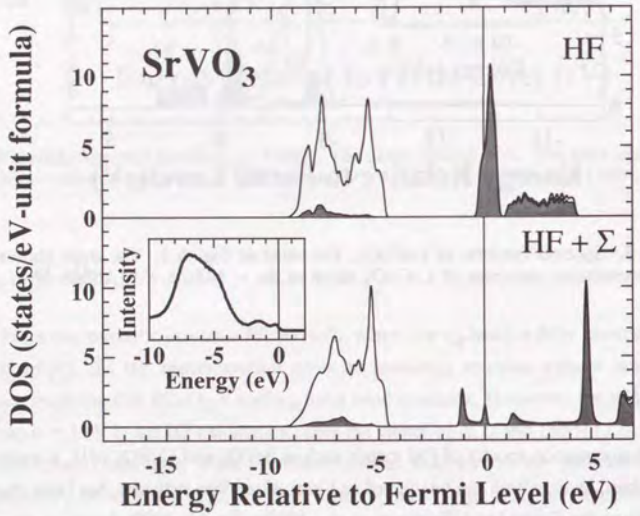

Fig. 6.4. Spectral function of $SrVO_3$. The same as Fig. 6.1. The inset shows the photoemission spectrum of $SrVO_3$ taken at $h\nu$ = 60 eV [Morikawa *et al.*, 1995].

6.3. Effect of low dimensionality

We have studied the one-dimensinal CuO_3 chain and the two-dimensional CuO_2 plane by using the second order perturbation around the PM, metallic HF solusions. In the one- and two-dimensional systems, the mometum dependence of the self-energy is expected to be important. Here, starting from the local approximation, the momentum dependence of the self-energy is included by taking into account the nearest neighbor and next nearest neighbor contributions to the self-energy.

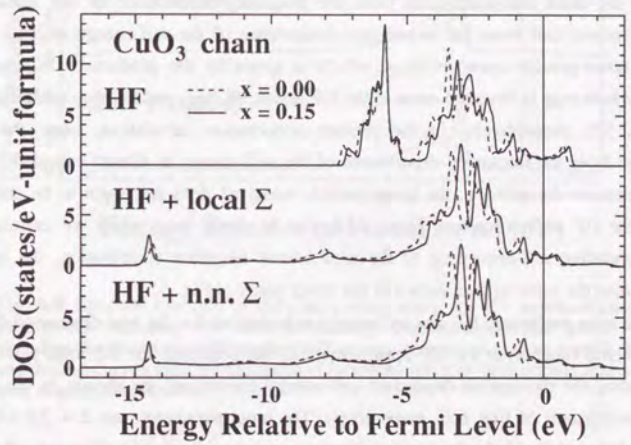

Fig. 6.5. Spectral functions of the CuO_3 chain using HF approximation (upper panel), those including the local self-energy correction (middle panel) and those including the momentum-dependent self-energy correction (lower panel). The solid and dashed curves indicate the spectral functions without hole doping and with 15% hole doping, respectively.

At first, let us present the result for the one-dimensional CuO_3 chain. Since one-dimensional metallic system is not a Fermi liquid but a Tomonaga-Luttinger liquid [Tomonaga, 1950; Luttinger, 1963], it seems to be meaningless to apply the self-energy correction to the Fermi liquid state in one dimension. However, many quasi-one-dimensional compounds which are expected to have Fermi-liquid ground states, show photoemission spectra in which the intensity at the Fermi level almost disappears as expected in a Tomonaga-Luttinger liquid. Therefore, it is interesting to investigate how the momentum-dependent self-energy correction

suppresses the spectral weight at the Fermi level in one dimension. The spectral functions of the CuO_3 chain obtained by the HF calculation and by the local self-energy calculation are shown in the upper and middle panels of Fig. 6.5. The input parameters are $\Delta = 2.0$ eV, $U = 7.5$ eV and $(pd\sigma) = -1.8$ eV. The band crossing the Fermi level is strongly renormalized by the local self-energy correction. While the intensity at the Fermi level is hardly changed, the band width is reduced to ~ 60 % of that in the HF approximation. The lower panel of Fig. 6.5 shows the spectral function corrected using the momentum-dependent self-energy which is calculated up to the nearest neighbor contribution. By including the momentum dependence of the self-energy, the intensity at the Fermi level is reduced to ~ 60 % and the band width is enlarged to ~ 150 % of that obtained from the local self-energy correction. This band renormalization indicates that the mass renormalization from the frequency-dependence of the self-energy $m_\omega/m_{HF} \sim 1/0.6$ and that from the momentum-dependence of the self-energy $m_k/m_{HF} \sim 0.6$ result in the quasi-particle mass m^*/m_{HF}, which is given by the product of m_ω/m_{HF} and m_k/m_{HF}, ~ 1, where m_{HF} is the band mass in the HF result. m_ω/m_{HF} and m_k/m_{HF} are defined by (2.54) and (2.55), respectively. In the present perturbation calculation, since the mass renormalization from the frequency-dependence of the self-energy is almost canceled by that from the momentum-dependence, the quasi-particle mass m^* does not seem to be enhanced from that in the HF approximation. Here, it should be noted that, when we calculate the momentum-dependent self-energy up to the next nearest neighbor contribution, the spectral function is almost the same as that shown in the lower panel of Fig. 6.5.

Next, we have performed HF and self-energy calculations for the two-dimensional CuO_2 plane. The spectral function in the HF approximation, that corrected for the local self-energy and that including the momentum-dependent self-energy correction, are shown in the upper, middle and lower panels of Fig. 6.6, respectively. The input parameters are $\Delta = 2.0$ eV, $U = 7.5$ eV and $(pd\sigma) = -1.8$ eV. In the spectral function including the local self-energy, the band width is almost equal to that obtained from the HF approximation and the intensity at the Fermi level is hardly changed. The spectral function corrected for the momentum-dependent self-energy, which is calculated up to the nearest neighbor contribution, is similar to that obtained from the local self-energy correction, indicating that the momentum dependence of the self-energy is small in the two-dimensional CuO_2 plane compared with that in the one-dimensional CuO_3 chain. Therefore, in contrast to the one-dimensional CuO_3 chain, the band renormalizaion near the Fermi level is small and $m_\omega/m_{HF} \sim 1$, $m_k/m_{HF} \sim 1$ and $m^*/m_{HF} \sim 1$ in the present perturbation calculation. In the charge-transfer-type cuprates, where the *d* weight near the Fermi level is small, the self-energy correction near the Fermi level is relatively small and the self-energy correction in the satellite region is very strong. In addition, the band crossing the Fermi level is non-degenerate in the cuprates, resulting in the small self-energy correction. On the other hand, in Mott-Hubbard-type $SrVO_3$, since the *d* weight near the Fermi level is large and

triply-degenerate t_{2g} bands cross the Fermi level, the effect of the self-energy is very strong near the Fermi level as shown in the previous section.

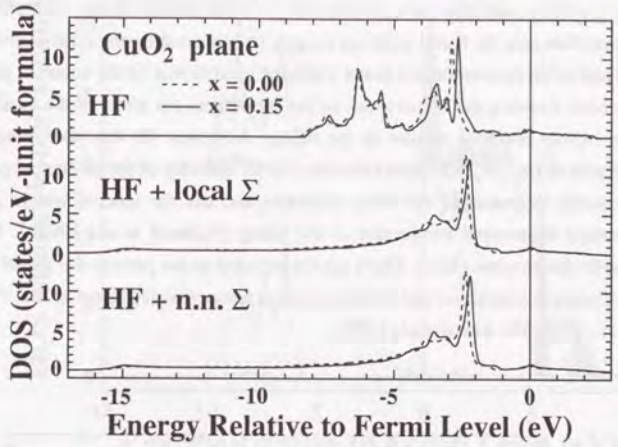

Fig. 6.6. Spectral function of the CuO_2 plane using the HF approximation (upper panel), that including the local self-energy correction (middle panel) and that including the momentum-dependent self-energy correction (lower panel). The solid and dashed curves indicate the spectral functions without hole doping and with 15% hole doping, respectively.

6.4. Effect of inter-site Coulomb interaction

As discussed in the previous section, the momentum dependence of the self-energy beyond the local approximation is not so strong in the *d-p* model whose dimension is more than one [Schweitzer and Czycholl, 1990]. However, in many two-dimensional metallic compounds such as $La_{2-x}Sr_xCuO_4$ [Fujimori *et al.*, 1989a, 1989b; Ino *et al.*, 1995] and three-dimensional metallic compounds such as $La_{1-x}Sr_xTiO_3$ [Fujimori *et al.*, 1992b], $Ca_{1-x}Sr_xVO_3$ [Eisaki, 1992; Fujimori *et al.*, 1992a; Inoue *et al.*, 1995; Morikawa *et al.*, 1995], $LaNiO_3$ [Kemp and Cox, 1990] and $LaCuO_3$ [Chapter 4], the spectral weight at the Fermi level is very small compared with that predicted by band-structure calculations. When we apply the present perturbation calculation to the metallic HF solution of the three-dimensional single-band Hubbard model, the self-energy hardly depends on the momentum and the density of states at the Fermi level is nearly equal to that of HF results [Khurana, 1989]. In the *d-p* model, the

momentum dependence of the self-energy is derived from that of the hybridization between the *d* and *p* orbitals. However, as shown in $LaCuO_3$ (see Fig. 4.5) and $SrVO_3$ (see Fig. 4.4), the intensity at the Fermi level is still overestimated in the calculations. A more serious discrepancy appears in a doped system or a filling-controlled system. In Fig. 6.7 and 6.8, the spectral functions for $La_{1-x}Sr_xTiO_3$ including the local self-energy correction are shown. The effect of the self-energy correction near the Fermi level can roughly be estimated by the relative intensity of the incoherent part or the remnant of the lower Hubbard band to that of the coherent part or the quasi-particle band crossing the Fermi level. In the calculation, the effect of the local self-energy correction rapidly becomes smaller as the fillings decreases. On the other hand, the photoemission spectra of $La_{1-x}Sr_xTiO_3$ shows that the relative intensity of the incoherent part to the coherent part hardly decreases as the filling decreases and that the spectral weight at the Fermi level is strongly suppressed irrespective of the filling [Fujimori *et al.*, 1992b]. These discrepancies may be due to some effects which are not included in the present *d-p* model such as the long-rang Coulomb interaction and electron-phonon interaction [Fujimori *et al.*, 1992a, 1992b; Inoue *et al.*, 1995; Morikawa *et al.*, 1995].

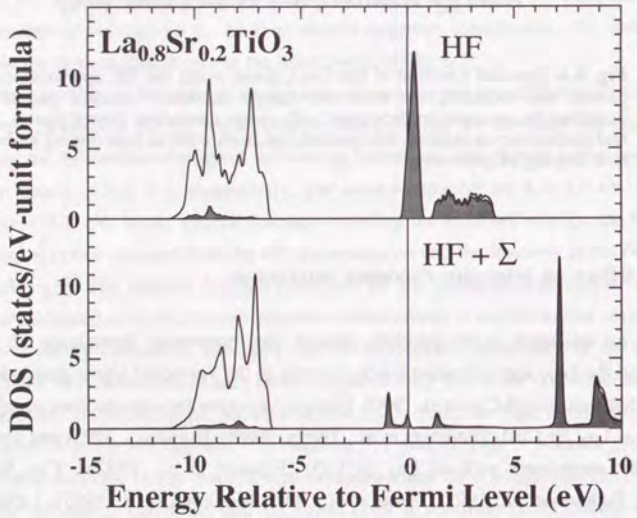

Fig. 6.7. Spectral function of $La_{0.8}Sr_{0.2}TiO_3$ calculated using the HF approximation (upper panel) and that including the self-energy correction calculated using the second-order perturbation (lower panel). The shaded area indicates the transition-metal 3*d* spectral weight.

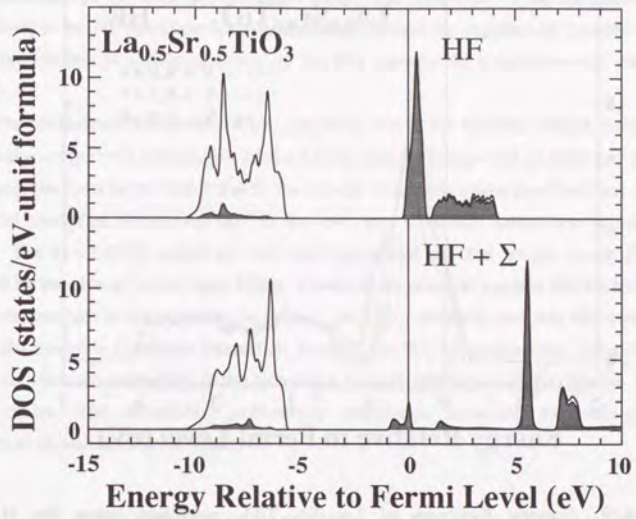

Fig. 6.8. Spectral function of $La_{0.5}Sr_{0.5}TiO_3$ calculated using the HF approximation (upper panel) and that including the self-energy correction calculated using the second-order perturbation (lower panel). The shaded area indicates the transition-metal 3*d* spectral weight.

The long-range part of the *d-d* Coulomb interaction is screened by the electronic polarization of the oxygen 2*p* subshell as well as by the lattice polarization in the insulating 3*d* transition-metal oxides [Chen and Overhauser, 1991]. However, when the *d* electron becomes itinerant, the screening cannot follow the motion of the *d* electron and the long-range Coulomb interaction may be important. On the other hand, in the high density limit, the non-local exchange part of the long-range Coulomb interaction is almost canceled by the correlation effect, the effect of the non-local exchange interaction is expected to be more important as the density of the *d* electron become low [Jang and Min, 1993]. Here, using the HF approximation, we have investigated how the density of states is affected by the exchange interaction derived from the unscreened nearest-neighbor Coulomb interaction *V*.

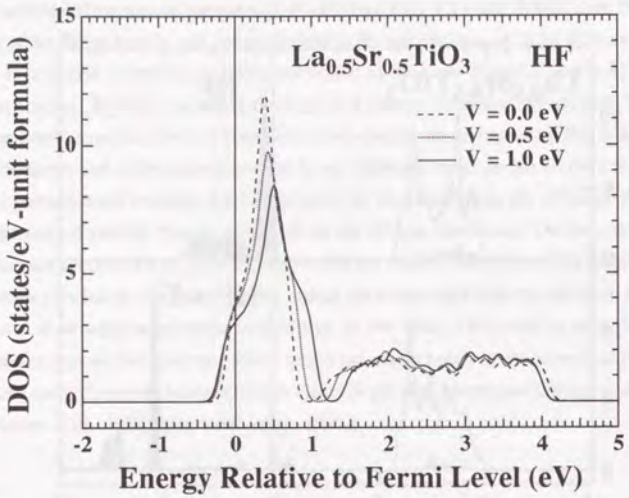

Fig. 6.9. Spectral functions of $La_{0.5}Sr_{0.5}TiO_3$ calculated using the HF approximation with inter-site Coulomb interaction V.

We have employed a model Hamiltonian obtained by adding the inter-site Coulomb term,

$$H_d = V \sum_{i,i',m\sigma,m'\sigma'} d^+_{i,m\sigma} d_{i,m\sigma} d^+_{i',m'\sigma'} d_{i',m'\sigma'} , \qquad (6.1)$$

to the Hamiltonian (2.17). When we have applied the HF approximation to the inter-site Coulomb term, the mean field Hamiltonian,

$$\begin{aligned} H_d^{MF} = {} & V \sum_{i,i',m\sigma,m'\sigma'} \left\langle d^+_{i,m\sigma} d_{i,m\sigma} \right\rangle d^+_{i',m'\sigma'} d_{i',m'\sigma'} + V \sum_{i,i',m\sigma,m'\sigma'} d^+_{i,m\sigma} d_{i,m\sigma} \left\langle d^+_{i',m'\sigma'} d_{i',m'\sigma'} \right\rangle \\ & - V \sum_{i,i',m\sigma,m'\sigma'} \left\langle d^+_{i,m\sigma} d_{i,m\sigma} \right\rangle \left\langle d^+_{i',m'\sigma'} d_{i',m'\sigma'} \right\rangle \\ & - V \sum_{i,i',m\sigma,m'\sigma'} \left\langle d^+_{i,m\sigma} d_{i',m'\sigma} \right\rangle d^+_{i',m'\sigma'} d_{i,m\sigma} - V \sum_{i,i',m\sigma,m'\sigma'} d^+_{i,m\sigma} d_{i',m'\sigma} \left\langle d^+_{i',m'\sigma'} d_{i,m\sigma} \right\rangle \\ & + V \sum_{i,i',m\sigma,m'\sigma'} \left\langle d^+_{i,m\sigma} d_{i',m'\sigma} \right\rangle \left\langle d^+_{i',m'\sigma'} d_{i,m\sigma} \right\rangle , \qquad (6.2) \end{aligned}$$

is obtained. The forth and fifth terms are derived from the inter-site exchange interaction and function as effective inter-site hopping terms. In Fig. 6.9, the density of states calculated using

the HF approximation for $La_{0.5}Sr_{0.5}TiO_3$ is shown. As the inter-site Coulomb interaction V increases, the band width of the t_{2g} band is enlarged and the intensity at the Fermi level is suppressed due to the inter-site exchange terms. The reduction of the spectral weight at the Fermi level in the HF calculation can qualitatively explain the suppressed spectral weight at the Fermi level which is widely observed in the PM metallic 3*d* transition-metal oxides such as $LaCuO_3$.

The photoemission spectra of $La_{1-x}Sr_xTiO_3$, where the spectral weight at the Fermi level is strongly suppressed irrespective of the filling, can be interpreted as follows. As the filling decreases, the correlation effect due to the on-site Coulomb interaction becomes small and the non-local exchange interaction due to the inter-site Coulomb interaction is expected to be strong. The two effects cancel out and the suppressed spectral weight at the Fermi level is affected by the change in the band filling. However, in order to explain the relative intensity of the incoherent part to the coherent part in $La_{1-x}Sr_xTiO_3$, we have to study the correlation effect due to the inter-site Coulomb interaction beyond the HF approximation. Another problem is how to estimate the magnitude of the inter-site Coulomb interaction in the metallic 3*d* transition-metal oxides. The quantitative self-energy calculation including the inter-site Coulomb interaction should be done in future.

6.5. Conclusion

The success of the cluster-model calculation in reproducing the photoemission spectra of the 3*d* transition-metal compounds suggests that the intra-cluster correlation effect is essential to explain the photoemission spectra. Assuming that the exact result of the lattice model gives essentially the same spectrum as that of the cluster model, the output of the cluster-model analyses is used as input of the lattice model in the present work. If we can fully include the correlation effect beyond the HF approximation, the photoemission spectra may be as well reproduced as by the cluster-model calculation. In this work, it is shown that the self-energy corrections to the HF solutions calculated to second order in U improve agreement between the photoemission spectra and the calculations both for the insulating and metallic oxides. The present method can be applied to a wider range of transition-metal compounds including halides, in which the local-cluster approach works as in the oxides [Fujimori and Minami, 1984; Zaanen, 1986], silicides, borides, etc., in which band-structure calculations seem to be a better starting point than the local-cluster calculation, and chalcogenides which seems to be located in the intermediate range of the two extremes. Systematic investigations of these compounds will give us a clue to link between the band picture and the local-cluster picture and lead us to deeper understanding of correlated *d*-electron systems. The self-energy correction may be improved by including higher-order terms and/or by going beyond the local

approximation. The higher-order ladder-type diagrams are expected to be required in order to better reproduce the satellite structure of NiO [Aryasetiawan and Gunnarsson, 1995] and the inclusion of the non-local part of the self-energy may be essential in low dimensional systems. Improvement along these lines remains to be done in future.

Chapter seven

Electronic structure of 3*d* transition-metal impurities in II-VI semiconductors

The electronic properties of substitutional 3*d* transition-metal impurities in II-VI semiconductors have been studied using the cluster and Anderson impurity models with configuration interaction. It is shown that the photoemission and inverse-photoemission spectra, *d-d* optical absorption spectra, exchange interaction between the magnetic moment and the host band states, donor and acceptor ionization energies can be reproduced with the same set of parameters, which show systematic variation with expected chemical trends. The importance of multiplet effects in the formation of donor and acceptor levels within the band gap is demonstrated. The electronic structure of hypothetical zinc-blende-type 3*d* transition-metal chalcogenides has been investigated by means of the unrestricted Hartree-Fock approach on a lattice model for the zinc-blende structure. The relationship between the electronic structure of the 3*d* transition-metal impurities in II-VI semiconductors and that of the 3*d* transition-metal chalcogenides has been discussed.

7.1. Introduction

3*d* transition-metal impurities in semiconductors have attracted much interest from their technological importance as well as from the viewpoint of basic physics: Apparently paradoxical experimental results have been obtained from different experimental techniques [Zunger, 1986]. Optical absorption spectra show a series of weak, sharp features due to intra-atomic *d*-*d* transition and have been analyzed by ligand-field theory [Kamimura *et al.*, 1969; Sugano *et al.*, 1970; Griffith, 1971], indicating that the 3*d* electrons are essentially localized. Donor and acceptor ionization energies deduced from transport and charge-transfer optical absorption show variation suggestive of multiplet effects [Fazzio *et al.*, 1984; Zunger 1986]. On the other hand, the reduction of hyperfine-coupling constants relative to free ions in electron-spin resonance spectra and super hyperfine interaction in electron-nuclear-spin double resonance spectra suggest that the 3*d* electrons are delocalized through strong hybridization with the host band states, and have been successfully reproduced by first-principles calculations using the local-density approximation (LDA) [Zunger, 1986; Katayama-Yoshida and Zunger, 1986; Oshiyama *et al.*, 1988]. Haldane and Anderson [1976] have shown using the unrestricted Hartree-Fock (HF) approximation that under the strong hybridization multiple charge states are formed within the band gap. There have been some attempts to describe the ionization energies and *d*-*d* transition energies starting from the HF or LDA solutions [Picoli and Chomette, 1984; Zunger, 1986; Katayama-Yoshida and Zunger, 1986; Oshiyama *et al.*, 1988]. For example, LDA calculations corrected for self-interaction have been extensively made by Zunger [1986] to calculate the donor and acceptor ionization energies. Recently, photoemission studies on diluted magnetic semiconductors [Furdyna, 1988] such as $Cd_{1-x}Mn_xTe$ have shown that the hybridization is quite substantial as predicted by the LDA calculations whereas there are also multi-electron satellite features which cannot be explained by one-electron theory [Taniguchi *et al.*, 1986]. In order to explain the photoemission spectra, cluster [Ley *et al.*, 1987; Taniguchi *et al.*, 1987] and Anderson impurity models [Gunnarsson *et al.*, 1989] with configuration interaction (CI) have been introduced. The latter models start from the ionic configuration and include CI with the ligand-to-3*d* charge-transferred configurations. In the light of the various physical pictures emerging from the different experiments and different theories, it is highly desirable to construct a coherent picture in which one can explain the various experimental data in a unified way.

In this chapter, we have applied CI theory to the analysis of a variety of experimental data and shown that the CI picture can indeed give a unified description of the electronic properties of the 3*d* transition-metal impurities. The organization of this chapter is as follows. A brief description of the CI picture is given in Sec. 7.2. In Sec. 7.3, we present the results of *d*-*d* absorption spectra, photoemission and inverse-photoemission spectra and exchange constants between the 3*d* magnetic moment and the host band states obtained from the cluster model

calculations. Donor and acceptor ionization energies are also calculated using the Anderson impurity model. Finally, in Sec.7.4, unrestricted Hartree-Fock calculations on a lattice model for zinc-blende structure are given.

7.2. Configuration-interaction approach

In the CI picture, the wavefunctions of the ground state and charge-conserving excited states, which we call *N*-electron states, are spanned by the d^n, $d^{n+1}\underline{L}$, ..., $d^{10}\underline{L}^{10-n}$ configurations, where $\underline{L}$ denotes a hole in the valence band for the Anderson impurity model or a hole in a ligand *p* orbital for the cluster model. The ligand-to-3*d* charge-transfer energy is defined by $\Delta \equiv E(d^{n+1}\underline{L}) - E(d^n)$ and the 3*d*-3*d* Coulomb interaction energy by $U \equiv E(d^{n-1}) + E(d^{n+1}) - 2E(d^n)$, where $E(d^n\underline{L}^{n'})$ is the center of gravity of the $d^n\underline{L}^{n'}$ multiplet. These definitions, from which the multiplet effect is excluded, makes clear the systematic variation of the parameters on cation atomic number and valence [Bocquet *et al.*, 1992b]. Alternatively, the charge-transfer and Coulomb interaction energies can be defined with respect to the lowest term of each multiplet, and are denoted by Δ_{eff} and U_{eff}, respectively. Note that the actual energy required for the acceptor ionization process $d^n \rightarrow d^{n+1} + \underline{L}$ is determined by Δ_{eff} rather than Δ. The multiplet splittings are given in terms of Racah *B*, *C* parameters, which are fixed to the free-ion values [Griffith, 1971].

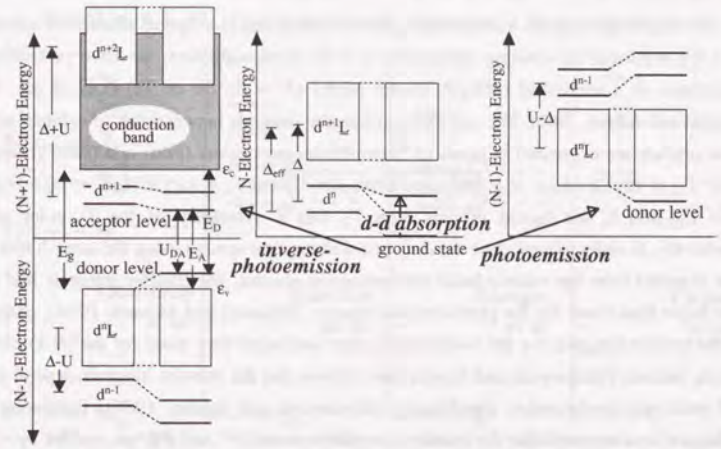

Fig. 7.1. Schematic energy-level diagrams for a d^n transition-metal impurity in a II-VI semiconductor, including hybridization between the 3*d* and host valence band. For clarity, higher-order charge-transfer states (e.g. $d^{n+2}\underline{L}^2$ in the *N*-electron states) are not shown.

The energy of the ground state $E_0(N)$ of the neutral impurity (A^0) as well as those of the excited d^n multiplet terms are obtained by diagonalizing the Hamiltonian in the N-electron subspace as shown in the central panel of Fig. 7.1. In the right panel of Fig. 7.1, we show the energy levels of the (N-1)-electron states (positively ionized impurity: A^+), namely, the final states of photoemission which are given by linear combinations of d^{n-1}, $d^n\underline{L}$, $d^{n+1}\underline{L}^2$, etc. The lowest energy level of the (N-1)-electron system is the first ionization level of the N-electron system or the donor level; The donor ionization energy is given by $E_0(N\text{-}1) - E_0(N) + \varepsilon_c$ ($\equiv E_D$), where ε_c is the energy of the conduction band minimum. The energy levels for the (N+1)-electron states (negatively ionized impurity: A^-) are shown in the left panel of Fig. 7.1. The lowest energy level of the (N+1)-electron system is the affinity level of the N-electron system or the acceptor level; The acceptor ionization energy is given by $E_0(N+1) - E_0(N) - \varepsilon_v$ ($\equiv E_A$), where ε_v is the energy of the valence band maximum. If we replot the electron removal energies $E(N\text{-}1) - E_0(N)$ downward and combine it with the electron addition energies $E(N+1) - E_0(N)$ as in the left panel of Fig. 7.1, we can effectively map the many-electron energies onto the one-electron energy-level scheme.

7.3. Confuguration-interaction calculation on cluster and Anderson impurity models

7.3.1. *d-d* optical absorption spectra

In order to analyze the valence-band photoemission and *d-d* optical absorption spectra of M^{2+} (A^0) impurities substituting cation sites in II-VI semiconductors, we have performed CI calculations on a tetrahedral $(MX_4)^{6-}$ cluster model (X = S, Se or Te) [Ley *et al.*, 1987; Bouhelal and Albert, 1989]. The one-electron transfer integrals between the 3*d* orbitals and the ligand orbitals are expressed in terms of Slater-Koster parameters ($pd\sigma$) and ($pd\pi$) [Harrison, 1989]: $T_{t2} \equiv \langle t_2 \mid h \mid L_{t2}\rangle = \sqrt{4/3(pd\sigma)^2+8/9(pd\pi)^2}$ and $T_e \equiv \langle e \mid h \mid L_e\rangle = 2\sqrt{6}/3(pd\pi)$, where L_{t2} and L_e are ligand orbitals with T_2 and E symmetry of the T_d point group, respectively. In order to reproduce the *d-d* optical absorption spectra using the same Δ and U as those obtained from the valence-band photoemission spectra, the transfer integrals had to be taken larger than those for the photoemission spectra [Fujimori and Minami, 1984], indicating that the transfer integrals for the N-electron system are larger than those for the (N-1)-electron system. Indeed, Gunnarsson and Jepsen have shown that the transfer integrals depend on the local electronic configuration significantly [Gunnarson and Jepsen, 1988]. Following their results, we have assumed that the transfer integrals between d^{n-1} and $d^n\underline{L}$ are smaller by ~20 % and those between d^{n+1} and $d^{n+2}\underline{L}$ larger by ~ 20% than those between d^n and $d^{n+1}\underline{L}$, etc. Values for d^n-$d^{n+1}\underline{L}$ are given in this paper.

In Fig. 7.2, the *d-d* optical absorption spectra of MnO [Mochizuki *et al.*, 1990], where the Mn^{2+} ion is octahedrally coordinated by six O^{2-} ions, and Mn^{2+} (d^5: A^0) impurities in ZnS [McClure, 1963], ZnSe [Langer and Richer, 1966] and CdTe [Lee and Ramdas, 1984] are compared with the result of CI cluster-model calculations. Here, we compare the calculated multiplet structures with the energies of absorption maxima in the spectra which correspond to the purely electronic (Frank-Condon) transition energies. The ground state of the Mn^{2+} impurity is $^6A_1$ in the tetrahedral as well as in the octahedral coordination geometry. The energy levels for the lowest excited terms $^4T_1$, $^4T_2$, $^4A_1$ and ^4E, which originate from the ^4G term of the free d^5 ion, are in good agreement with experiment. Agreement is less satisfactory for higher terms ^4E, $^4T_1$ and $^4T_2$, which are derived from the ^4D and ^4P terms, because the energy levels of the ^4D and ^4P of the free d^5 ion already cannot be accurately reproduced within the Racah parameter scheme. The obtained parameter sets are listed in Table 7.1, where one can see that in going from S to Se to Te the charge-transfer energy Δ decreases as the electronegativity of the ligand decreases and that the transfer integral ($pd\sigma$) also decreases as the distance between the transition-metal cation and the ligand anions increases [Harisson, 1989]. The effects of the decrease in Δ and in ($pd\sigma$) cancel out to yield almost identical $^6A_1$-$^4T_1$ separation, consistent with the experimental results.

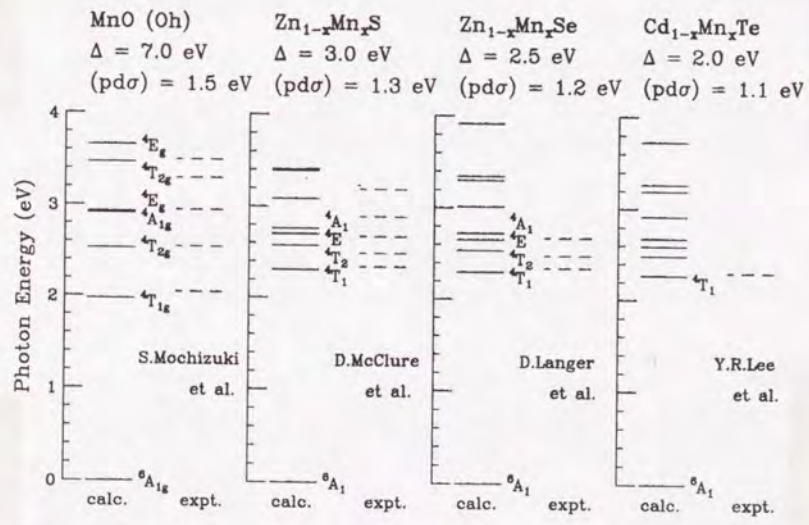

Fig. 7.2. Energy levels for Mn^{2+} (A^0) impurities in II-VI semiconductors and MnO calculated using the CI cluster model compared with experimental *d-d* optical absorption spectra [McClure, 1963; Langer and Richer, 1966; Lee and ramdas, 1984; Mochizuki *et al.*, 1990].

We have also performed CI cluster-model calculations for various transition-metal impurities, V to Ni, in ZnS and ZnSe. The *d-d* optical absorption spectra [McClure, 1963; Roussos and Schulz, 1980; Weakliem, 1962; Koidl *et al.*, 1973; Ham and Slack, 1971; Kelly and Williams, 1970; Grebe and Schulz, 1972; Grebe *et al.*, 1976; Hoang and Baranowski, 1977] are compared with the CI cluster-model calculations in Fig. 7.3 for the ZnS host. The obtained parameters are listed in Table 7.2. The calculated *d-d* transition energies are generally in good agreement with the experimental results. Agreement for the $^4T_1$ level of Co^{2+} and the $^3T_1$ level of Cr^{2+} is less satisfactory because the energy level of ^4P for the free d^7 ion and that of ^3P for the free d^4 ion already cannot be reproduced well within the Racah parameter scheme. The value of Δ thus obtained is monotonically decreases in going from lighter to heavier transition-metal atoms as expected from chemical trends whereas Δ_{eff} exhibits non-monotonic behavior due to the multiplet effects [Zaanen, 1986; Zaanen and Sawatzky, 1987, 1990; Bocquet *et al.*, 1992b].

Table 7.1. Parameters used to calculate the valence-band photoemission and inverse photoemission spectra and *d-d* optical absorption spectra (in eV).

	Δ	U	$(pd\sigma)$
MnO	7.0	5.5	-1.5
$Cd_{1-x}Mn_xS/Zn_{1-x}Mn_xS$	3.0	4.0	-1.3
$Cd_{1-x}Mn_xSe/Zn_{1-x}Mn_xSe$	2.5	4.0	-1.2
$Cd_{1-x}Mn_xTe$	2.0	4.0	-1.1

Table 7.2. Parameters used to calculate the *d-d* optical absorption spectra of neutral (Mn^{2+}: A^0) transition-metal impurities in ZnS and ZnSe (in eV). Racah *B* and *C* parameters are fixed to the values of free ions [Griffith, 1971].

			ZnS		ZnSe	
	B	*C*	Δ (Δ_{eff})	$(pd\sigma)$	Δ (Δ_{eff})	$(pd\sigma)$
Ni^{2+}	0.135	0.600	1.0 (2.3)	-1.2	0.5 (1.8)	-1.1
Co^{2+}	0.138	0.541	1.5 (2.9)	-1.1	1.0 (2.4)	-1.0
Fe^{2+}	0.131	0.484	2.0 (3.3)	-1.2	1.5 (2.8)	-1.05
Mn^{2+}	0.119	0.412	3.0 (5.2)	-1.3	2.5 (4.7)	-1.2
Cr^{2+}	0.103	0.425	4.0 (1.9)	-1.2	3.5 (1.4)	-1.1
V^{2+}	0.095	0.354	4.5 (3.6)	-1.3	4.0 (3.1)	-1.2

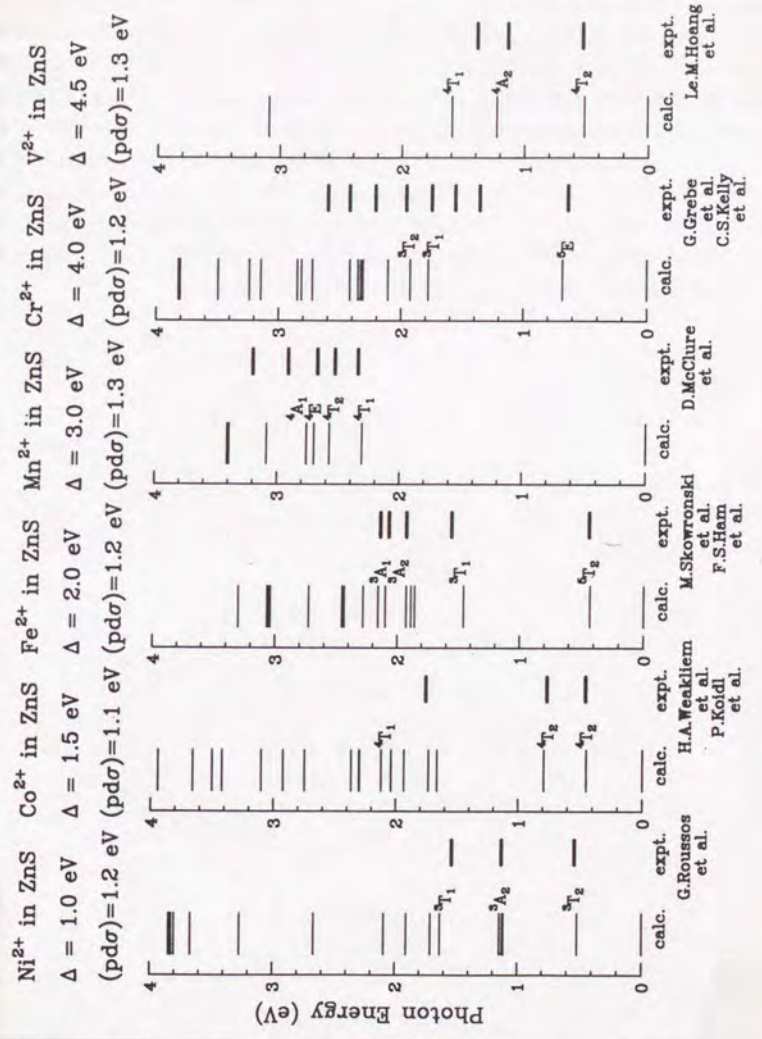

Fig. 7.3. Energy levels for various transition-metal impurities (from V^{2+} to Ni^{2+}) in ZnS calculated using the CI cluster model compared with experimental *d-d* optical absorption spectra [McClure, 1963; Roussos and Schulz, 1980; Weakliem, 1962; Koidl *et al.*, 1973; Ham and Slack, 1971; Kelly and Williams, 1970; Grebe and Schulz, 1972; Grebe *et al.*, 1976; Hoang and Baranowski, 1977].

7.3.2. Photoemission and inverse-photoemission spectra

In Fig. 7.4, we compare the Mn 3*d*-derived photoemission spectra of $Cd_{1-x}Mn_xY$ (Y = S, Se, Te) [Taniguchi *et al.*, 1986; Ley *et al.*, 1987] with those calculated using the CI cluster model. In contrast to the *d-d* optical absorption spectra, the changes in Δ and ($pd\sigma$) with ligand atoms affect the photoemission spectra constructively because the energy-level ordering of the ionic (d^5 or d^4) and charge-transfer ($d^6\underline{L}$ or $d^5\underline{L}$) configurations is inverted in going from the N-electron to the (N-1)-electron states: In going from S to Se to Te, the intensity within ~2.5 eV of the valence-band maximum relative to the main peak at ~3.4 eV decreases and that of the satellite structure at 5-9 eV increases, which is well reproduced with the same parameter sets obtained from the *d-d* optical absorption spectra given in Table 7.1.

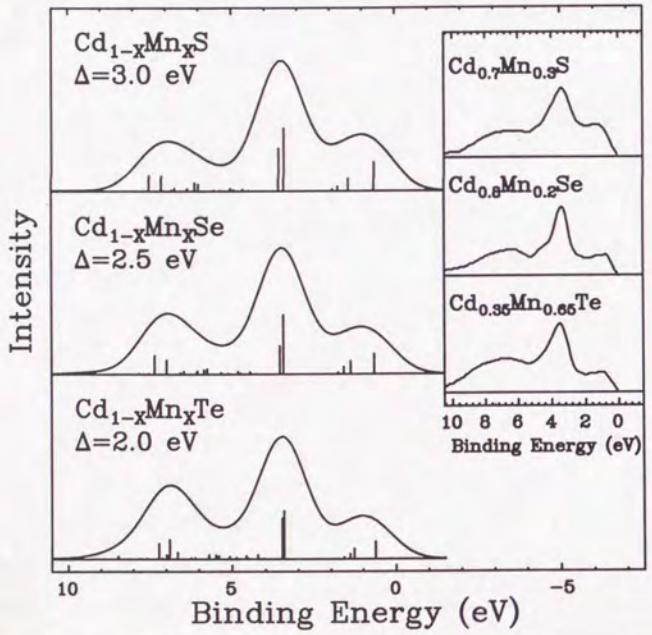

Fig. 7.4. Mn 3*d*-derived photoemission spectra for $Cd_{1-x}Mn_xY$ (Y = S, Se, Te) calculated using the CI cluster model. Experimental results [Taniguchi *et al.*, 1987] are shown in the inset.

As for the inverse-photoemission spectra, the Mn 3*d*-derived structure ~4.8 eV above the valence-band maximum [Franciosi *et al.*, 1989] is also reproduced by the CI cluster-model calculation as shown in Fig. 7.5 whereas *ab-initio* local-spin-density approximation (LSDA) band-structure calculations [Wei and Zunger, 1987] have predicted it to be ~2 eV above the valence-band maximum. The failure of the band-structure calculation is due to the neglect of the Coulomb contribution to the Mn $3d\uparrow$-$3d\downarrow$ splitting, which is entirely due to the exchange interaction in the LSDA band-structure calculation.

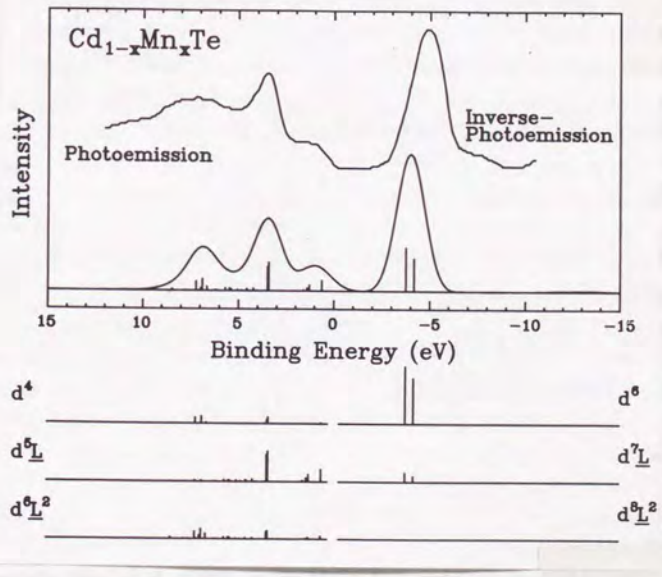

Fig. 7.5. Mn 3*d*-derived photoemission [Taniguchi *et al.*, 1987] and inverse-photoemission spectra [Franciosi *et al.*, 1989] for $Cd_{1-x}Mn_xTe$ compared with those obtained by the CI cluster model.

7.3.3. Exchange constants

In the II-VI semiconductors, the conduction band is mainly formed by the *s* orbitals of the cation and the valence band by the *p* orbitals of the anion. The exchange interaction between the *s* electrons in the conduction band and the *d* electrons of the transition-metal impurities is derived from the so-called direct exchange. On the other hand, the exchange interaction between the *p* electrons in the valence band and the *d* electrons is mainly determined by the *p-d* hybridization [Furdyna, 1988; Larsson *et al.*, 1988; Hass, 1991]. Especially at the Γ point, the top of the valence band is purely constructed from the anion *p* orbitals which can only hybridize with the *d* orbitals of the t_2 symmetry. When the magnetic moments of the transition-metal impurities are aligned by a magnetic field, the valence and conduction bands are split through the exchange interaction. The band splitting have been studied by free exciton spectroscopy and the exchange constant $N\beta$ between the 3*d* electrons and the Bloch electrons at the valence band maximum has been obtained [Furdyna, 1988].

Let us consider an Anderson impurity model in which the 3*d*-3*d* Coulomb interaction is taken into account in terms of Kanamori parameters, *u*, *u'*, *j* and *j'*, in order to calculate the exchange constant. The Hamiltonian is given by

$$H = \varepsilon_s \sum_{\vec{k},\sigma} s^+_{\vec{k},\sigma} s_{\vec{k},\sigma} + \varepsilon_p \sum_{\vec{k},l,\sigma} p^+_{\vec{k},l\sigma} p_{\vec{k},l\sigma} + \sum_{\vec{k},\sigma} V^{ss}_{\vec{k}} s^+_{\vec{k},\sigma} s_{\vec{k},\sigma} + \text{H. c.}$$
$$+ \sum_{\vec{k},l,\sigma} V^{sp}_{\vec{k},l} s^+_{\vec{k},\sigma} p_{\vec{k},l'\sigma} + \text{H. c.} + \sum_{\vec{k},l>l',\sigma} V^{pp}_{\vec{k},ll'} p^+_{\vec{k},l\sigma} p_{\vec{k},l'\sigma} + \text{H. c.} + H_{pd} + H_d \qquad (7.1)$$

$$H_d = \varepsilon^0_d \sum_{i,m,\sigma} d^+_{i,m\sigma} d_{i,m\sigma} + \sum_{i,m,m',\sigma,\sigma'} h_{m\sigma,m'\sigma'} d^+_{i,m\sigma} d_{i,m'\sigma'}$$
$$+ \sum_{i,m} u\, d^+_{i,m\uparrow} d_{i,m\uparrow} d^+_{i,m\downarrow} d_{i,m\downarrow} + \sum_{i,m\neq m'} u'\, d^+_{i,m\uparrow} d_{i,m\uparrow} d^+_{i,m'\downarrow} d_{i,m'\downarrow}$$
$$+ \sum_{i,m>m',\sigma} (u'-j)\, d^+_{i,m\sigma} d_{i,m\sigma} d^+_{i,m'\sigma} d_{i,m'\sigma} + \sum_{i,m\neq m'} j'\, d^+_{i,m\uparrow} d_{i,m'\uparrow} d^+_{i,m\downarrow} d_{i,m'\downarrow}$$
$$+ \sum_{i,m\neq m'} j\, d^+_{i,m\uparrow} d_{i,m'\uparrow} d^+_{i,m'\downarrow} d_{i,m\downarrow}, \qquad (7.2)$$

$$H_{pd} = \sum_{\vec{k},l,\sigma} \sum_{i,m} V^{pd}_{\vec{k},lm} p^+_{\vec{k},l\sigma} d_{i,m\sigma} + \text{H. c.}, \qquad (7.3)$$

where

$$p^+_{\vec{k},l\sigma} \equiv \frac{1}{\sqrt{N}} \sum_i e^{i\vec{k}\cdot\vec{R}_i} p^+_{l\sigma}. \qquad (7.4)$$

(7.1) represents the Hamiltonian for the cation *s* and anion *p* orbitals of the host semiconductor. (7.2) describes the Hamiltonian for the 3*d* orbitals of the transition-metal impurity, in which the

crystal field is expressed by $h_{m\sigma,m'\sigma'}$ and the interatomic 3*d*-3*d* Coulomb interaction by Kanamori parameters, *u*, *u'*, *j* and *j'* [Kanamori, 1963]. We have to assume the relationships $u' = u - 2j$ and $j' = j$ in order to keep the rotational invariance in real space of the Coulomb terms. The hybridization between the 3*d* orbitals and the host band states is expressed by (7.3).

Using the electronic-structure parameters obtained from the cluster-model analysis, we can calculate $N\beta$'s for the 3*d* transition-metal impurities in the second order of perturbation on the hybridization term. The terms which contribute to the second order perturbation are summarized in Fig. 7.6, which is good approximation in the dilute limit. The calculated $N\beta$'s are listed in Table 7.3. For example, the exchange constant $N\beta$'s for the Mn^{2+}, Fe^{2+} and Co^{2+} impurities are given by

$$\sim -(16/S)[1/(-\delta_{eff} + U_{eff}) + 1/\delta_{eff}](1/3(pd\sigma) - 2/9\sqrt{3}(pd\pi))^2 \qquad (7.5)$$

[Larsson *et al.*, 1988; Hass, 1991], where δ_{eff} is defined by $\Delta_{eff} - W_V/2$ and W_V is the width of the host valence band. W_V is fixed at 2 eV. U_{eff} is given by $u + 4j$, $u + 3j$ and $u + 2j$ for the Mn^{2+}, Fe^{2+} and Co^{2+} impurities respectively. The factor $1/3(pd\sigma) - 2/9\sqrt{3}(pd\pi)$ is the transfer integral between the t_2 orbitals and the orbitals at the valence-band maximum of the host semiconductor. Here, the magnitude of the local spin *S* is 5/2, 2 and 3/2 for Mn^{2+}, Fe^{2+} and Co^{2+}, respectively. The $N\beta$ values for $Cd_{1-x}Mn_xY$ (*Y* = S, Se and Te) evaluated using the above parameters are -1.3, -1.1 and -0.9, which are in good agreement with the experimental results, -1.8, -1.11 and -0.88 for *Y* = S, Se and Te, respectively [Furdyna, 1988]. Here, the values for the *N*-electron state are used for $(pd\sigma)$ and $(pd\pi)$ since $N\beta$ is obtained from magneto-optical measurements. In the estimation by Larsson *et al.* [1988], $\varepsilon_v - \varepsilon_d \sim 3.4$ eV instead of δ_{eff} has been used in (7.5) for Mn compounds, where ε_d is the position of the main peak in the photoemission spectra. The $\varepsilon_v - \varepsilon_d$ values thus estimated are roughly constant, whereas the δ_{eff} values obtained from the photoemission spectra actually decrease in going from S to Se to Te. The $N\beta$ values for the Mn^{2+}, Fe^{2+} and Co^{2+} impurities in ZnSe are calculated to be -1.1, -1.3 and -2.3 eV, respectively, using the parameters listed in Table 7.3. These values are also in agreement with the experimental values -1.238, -1.450 and -1.883 for Mn^{2+}, Fe^{2+} and Co^{2+} impurities in ZnSe [Hamdani *et al.*, 1992].

Recently, it has been reported that the exchange constant $N\beta$ for Cr^{2+} in ZnSe is positive, namely, the local spin of the Cr^{2+} ion and that of the hole in the host valence band couple ferromagnetically [Mac *et al.*, 1993]. In the Mn^{2+}, Fe^{2+} and Co^{2+} impurities, where the t_2 orbitals are half filled, a ligand hole whose spin is antiparallel to that of the transition-metal impurity can only be transferred into the unoccupied t_2 orbitals. Therefore, the *p-d* exchange is always antiferromagnetic. On the other hand, for the Cr^{2+} impurity, a ligand hole whose spin is parallel as well as antiparallel can be transferred to the unoccupied t_2 orbitals. As a result, ferromagnetic and antiferromagnetic terms coexist in the *p-d* exchange interaction. The Cr^{2+}

impurity, where the t_2 orbitals are partially occupied, undergoes a Jahn-Teller distortion which makes the evaluation of $N\beta$ complicated. Here, we have assumed that the populations of the CrY_4 tetrahedra elongated along *x*-, *y*- and *z*-directions are 1/3 [Mac *et al.*, 1994; Bhattacharjee, 1994]. The terms which contribute to the *p-d* exchange are given in Fig. 7.6 (b). $N\beta$'s for the Cr^{2+} impurities in ZnS and ZnSe thus calculated are -0.5 eV and +0.8 eV, respectively, as listed in Table 7.3. The positive $N\beta$ value for the Cr^{2+} impurity in ZnSe is in good agreement with the experimental value +0.85 [Mac *et al.*, 1993]. $N\beta$ for the Cr^{2+} impurity in ZnS becomes negative because δ_{eff} of Cr^{2+} in ZnS is large compared with that of Cr^{2+} in ZnSe.

V^{2+} and Ni^{2+} impurities, where t_2 orbitals are partially filled, should also be accompanied by the Jahn-Teller distortion. Under the same assumption, the terms for the *p-d* exchange can be determined as shown in Fig. 7.6 (c) and (d). The V^{2+} impurity is expected to show the same behavior as the Cr^{2+} impurity because the t_2 subshell is less than half-filled. However, $N\beta$'s for V^{2+} thus calculated are negative as listed in Table 7.3. This is because δ_{eff} of V^{2+} is much larger than that of Cr^{2+} in ZnSe.

For Ti^{2+}, where t_2 orbitals are empty, ligand holes can be transferred into the t_2 orbitals irrespective of their spin direction. As shown in Fig. 7.6 (e), the state obtained by the transfer of the ligand hole whose spin is parallel to the Ti^{2+} spin is stabilized by the intra-atomic exchange interaction *j*. Therefore the *p-d* exchange constant for Ti^{2+} becomes positive as listed in Table 7.3. It is very interesting to check the prediction for the *p-d* exchange constant, especially for the positive value of Ti^{2+}. However, no experimental result of the Ti^{2+}, V^{2+} and Ni^{2+} impurities in II-VI semiconductors has been reported.

Table 7.3. Exchange constant $N\beta$'s for the 3*d* transition-metal impurities in ZnS and ZnSe (in eV). Kanamori parameters are fixed to the values of free ions.

			ZnS		ZnSe	
	u	*j*	δ_{eff}	$N\beta$	δ_{eff}	$N\beta$
Ni^{2+}	7.58	0.94	0.7	-6.0	0.2	-20.0
Co^{2+}	6.97	0.89	1.9	-2.2	1.4	-2.3
Fe^{2+}	6.30	0.81	2.9	-1.5	2.4	-1.3
Mn^{2+}	5.58	0.71	4.2	-1.3	3.7	-1.1
Cr^{2+}	5.02	0.68	0.9	-0.5	0.4	+0.8
V^{2+}	4.32	0.59	2.1	-3.1	1.6	-0.8
Ti^{2+}	3.72	0.55	2.4	+0.8	1.9	+1.0

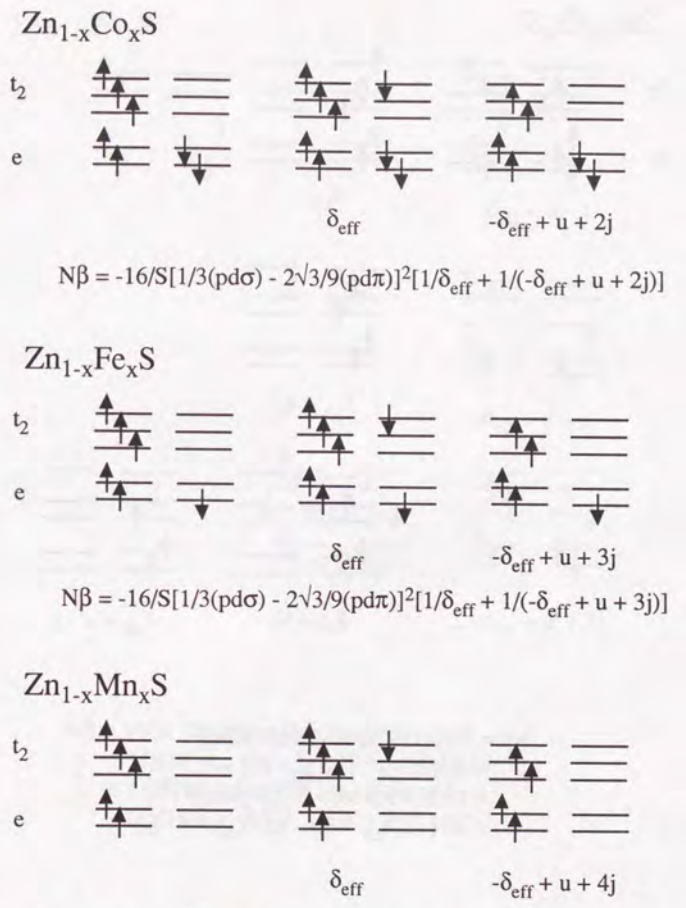

Fig. 7.6. (a) Configurations which contribute to the *p-d* exchange interaction in the second order of the hybridization term for $Zn_{1-x}Co_xS$, $Zn_{1-x}Fe_xS$ and $Zn_{1-x}Mn_xS$. The configurations for the ground state, affinity states and ionization states are shown in the left, middle and right column, respectively, below which the energy difference between the ground state and each affinity or ionization state is shown.

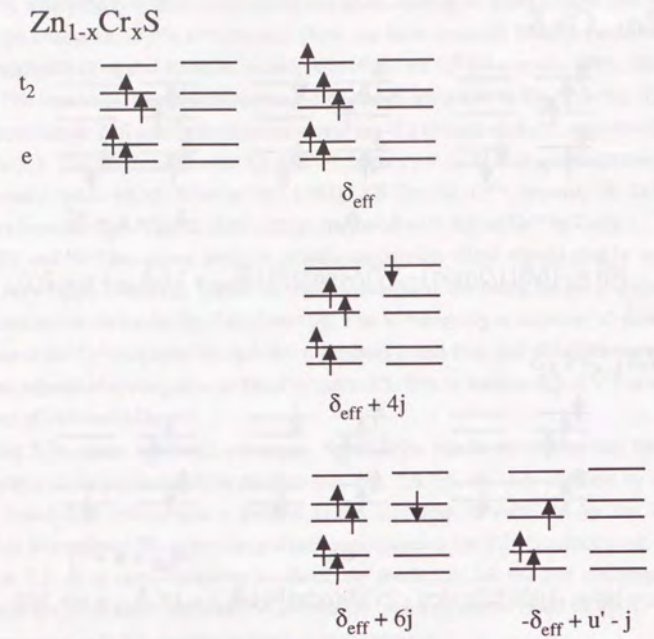

$$N\beta = 16/S[1/3(pd\sigma) - 2\sqrt{3}/9(pd\pi)]^2 \times 1/3[1/\delta_{eff} - 1/(\delta_{eff} + 4j)] + 16/S[1/3(pd\sigma) - 2\sqrt{3}/9(pd\pi)]^2 \times 2/3[-1/(\delta_{eff} + 6j) - 1/(-\delta_{eff} + u' - j)]$$

Fig. 7.6. (b) Configurations which contribute to the *p-d* exchange interaction in the second order of the hybridization term for $Zn_{1-x}Cr_xS$. The configurations for the ground state, affinity states and ionization states are shown in the left, middle and right column, respectively, below which the energy difference between the ground state and each affinity or ionization state is shown.

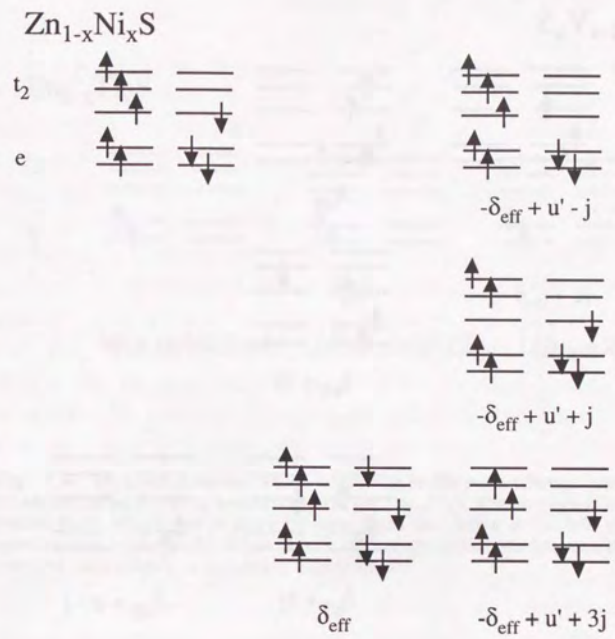

$$N\beta = 16/S[1/3(pd\sigma) - 2\sqrt{3}/9(pd\pi)]^2 \times 1/3[1/(-\delta_{eff} + u' - j) - 1/(-\delta_{eff} + u' + j)] + 16/S[1/3(pd\sigma) - 2\sqrt{3}/9(pd\pi)]^2 \times 2/3[-1/\delta_{eff} - 1/(-\delta_{eff} + u' + 3j)]$$

Fig. 7.6. (c) Configurations which contribute to the *p-d* exchange interaction in the second order of the hybridization term for $Zn_{1-x}Ni_xS$. The configurations for the ground state, affinity states and ionization states are shown in the left, middle and right column, respectively, below which the energy difference between the ground state and each affinity or ionization state is shown.

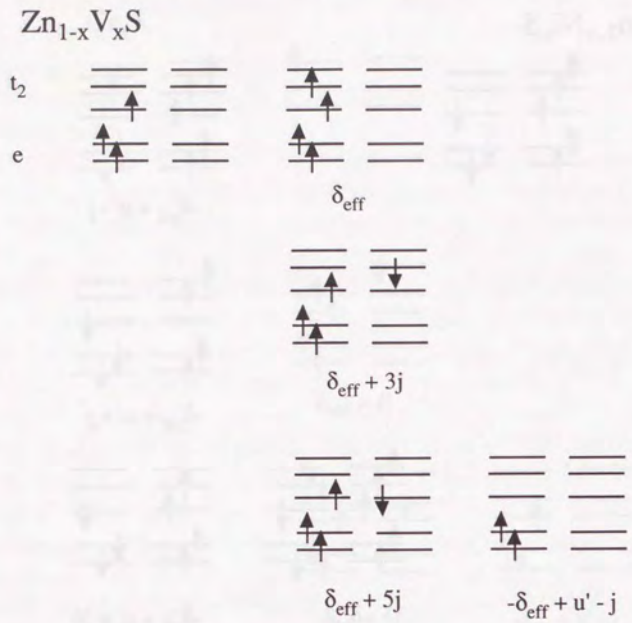

$$N\beta = 16/S[1/3(pd\sigma) - 2\sqrt{3}/9(pd\pi)]^2 \times 2/3[1/\delta_{eff} - 1/(\delta_{eff} + 3j)] + 16/S[1/3(pd\sigma) - 2\sqrt{3}/9(pd\pi)]^2 \times 1/3[-1/(\delta_{eff} + 5j) - 1/(-\delta_{eff} + u' - j)]$$

Fig. 7.6. (d) Configurations which contribute to the *p-d* exchange interaction in the second order of the hybridization term for $Zn_{1-x}V_xS$. The configurations for the ground state, affinity states and ionization states are shown in the left, middle and right column, respectively, below which the energy difference between the ground state and each affinity or ionization state is shown.

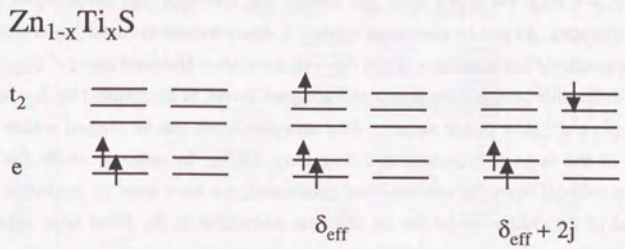

$$N\beta = 16/S[1/3(pd\sigma) - 2\sqrt{3}/9(pd\pi)]^2[1/\delta_{eff} - 1/(\delta_{eff} + 2j)]$$

Fig. 7.6. (e) Configurations which contribute to the *p-d* exchange interaction in the second order of the hybridization term for $Zn_{1-x}Ti_xS$. The configurations for the ground state, affinity states and ionization states are shown in the left, middle and right column, respectively, below which the energy difference between the ground state and each affinity or ionization state is shown.

7.3.4. Donor and acceptor ionization energies

When $\Delta_{eff} < U_{eff}$, the donor level has mainly $d^n\underline{L}$ character and the acceptor level has mainly d^{n+1} character. As can be seen from Table 7.2, many transition-metal impurities in II-VI semiconductors satisfy this condition. Then the "effective Mott-Hubbard energy" U_{DA} (see Fig. 7.1), *i.e.* the difference between the donor and acceptor levels, is determined by Δ_{eff} rather than U_{eff} and therefore $d^n\underline{L}$-like donor and d^{n+1}-like acceptor levels can be formed within the band gap in spite of the large U [Haldane and Anderson, 1976]. In order to study the $d^n\underline{L}$-like discrete states split-off from the valence-band continuum, we have used an Anderson impurity model instead of the cluster model for an M^{2+} ion embedded in the filled host valence band [Zaanen, 1986; Gunnarsson *et al.*, 1989]. In order to solve the model numerically, the intra-atomic multiplet coupling is approximated by retaining only the diagonal matrix elements in Kanamori parameters [Bocquet *et al.*, 1992b]. As for the transfer integrals, we introduce $V_{t2}(\varepsilon) \equiv < t_2 \mid h \mid \underline{L}_{t2}(\varepsilon) >$ and $V_e(\varepsilon) \equiv < e \mid h \mid \underline{L}_e(\varepsilon) >$, where ε is the energy of the valence electron. The energy dependence of $|V_{t2}(\varepsilon)|^2$ and $|V_e(\varepsilon)|^2$ is assumed to be semi-ellipsoids with an appropriate width W_V, which is taken to be ~ 2 eV for sulfides and selenides. Although the width of the valence band is 4-5 eV for ZnS or ZnSe studied here, the top 2-3 eV of the valence-band is found to mainly contribute to the $|V_{t2}(\varepsilon)|^2$ and $|V_e(\varepsilon)|^2$. Here, it has been confirmed using a tight-binding band model that a band with relatively small dispersion ~2-3 eV, which is mainly constructed from the anion *p* and cation *s* orbitals, strongly hybridizes with the impurity 3*d* orbitals. In actual calculations, the valence-band continuum is replaced by 10-20 discrete states, and $\int|V_{t2}(\varepsilon)|^2 d\varepsilon$ and $\int|V_e(\varepsilon)|^2 d\varepsilon$ are assumed to be equal to $T_{t2}{}^2$ and $T_e{}^2$, respectively. Under this condition, the $W_V \rightarrow 0$ limit corresponds to the cluster model.

As shown in Fig. 7.7, for Cr^{2+}, a $d^4\underline{L}$-like split-off state is formed well below the $d^4\underline{L}$ continuum in the (N–1)-electron state through the strong hybridization with the d^3 state, which originally lies $U_{eff}-\Delta_{eff}$ ~ 1.1 eV above the center of the $d^4\underline{L}$ continuum. The split-off state corresponds to the donor level in the band gap. Since $U_{DA} \sim \Delta_{eff}$ and the Δ_{eff} is smaller than the band gap of ZnS, the lowest energy level of the (N+1)-electron state or the acceptor level is located below the conduction-band minimum. We can map the donor and acceptor levels onto the one-electron energy-level scheme following the procedure described in Sec. 7.2 (see Fig. 7.1). On the other hand, in the (N–1)-electron state of Mn^{2+} in ZnS, a discrete state hardly splits off from the $d^5\underline{L}$ continuum as shown in Fig. 7.8 because the d^4 state is too far ($U_{eff}-\Delta_{eff}$ ~ 3.2 eV) above the center of the $d^5\underline{L}$ continuum, which is stabilized by the exchange energy of the half-filled d^5 shell, to induce a split-off state. An acceptor level is also not formed within the band gap since the Δ_{eff} is much larger than the band gap of ZnS.

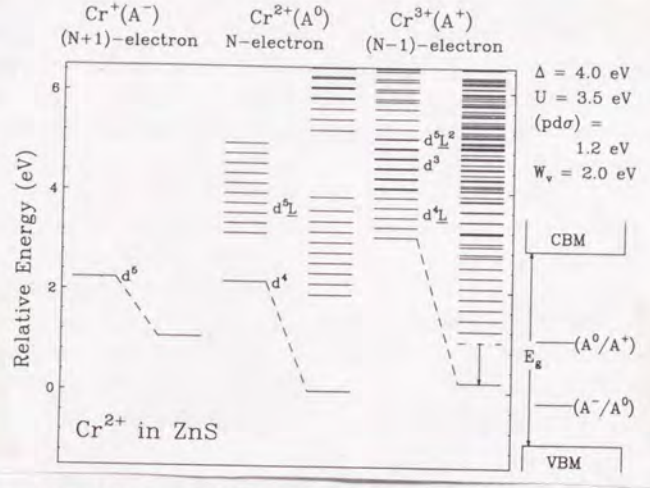

Fig. 7.7. (N-1)-electron (A^+), N-electron (A^0) and (N+1)-electron (A^-) energy levels of a Cr impurity in ZnS calculated using the Anderson impurity model. The inset shows their mapping onto the one-electron energy-level scheme.

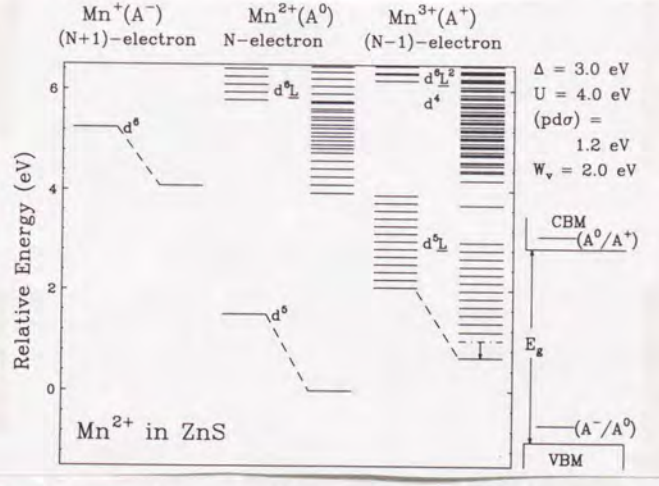

Fig. 7.8. (N-1)-electron (A^+), N-electron (A^0) and (N+1)-electron (A^-) energy levels of a Mn impurity in ZnS calculated using the Anderson impurity model. The inset shows their mapping onto the one-electron energy-level scheme.

In Fig. 7.9, the donor and acceptor ionization levels, $\varepsilon_c - E_D$ and $\varepsilon_v + E_A$, calculated using the parameter sets in Table 7.2 are compared with experimental results [Fazzio, 1984; Zunger, 1986]. The calculated values are generally in good agreement with the experimental results. For most of the transition metal impurities, since the Δ_{eff}'s are smaller than the band gaps of ZnS and ZnSe, the acceptor levels are located below the conduction band minimum. The calculated results explain the general lowering of the donor and acceptor levels with increasing atomic number of the transition-metal impurities as due to the monotonic decrease of Δ. As mentioned above, on the other hand, the local maxima and minima at Cr, Mn or Fe are attributed to the multiplet effects, which are reflected upon the non-monotonic behavior of Δ_{eff}.

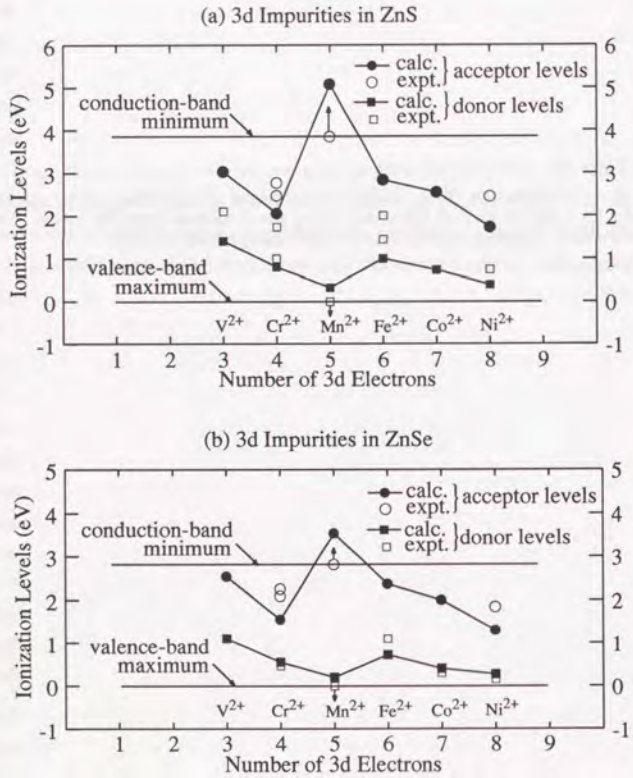

Fig. 7.9. Donor and acceptor ionization levels for various 3*d* transition-metal impurities in ZnS (a) and ZnSe (b) calculated using the Anderson impurity model. The calculations are compared with experimental values [Zunger, 1986].

7.4. Unrestricted Hartree-Fock calculation on a lattice model for zinc-blende structure

The sign of the *d-d* superexchange interaction is related to that of the *p-d* exchange constant in the transition-metal substituted II-VI diluted magnetic semiconductors [Larson *et al.*, 1988]. Therefore, the magnetic structure of the zinc-blende-type 3*d* transition-metal chalcogenides, which can be regarded as the 100% substituted limit of the diluted magnetic semiconductors, is expected to reflect character of the *p-d* exchange interaction. In order to investigate the electronic structure of the zinc-blende-type 3*d* transition-metal chalcogenides, we can apply the unrestricted HF calculation to a zinc-blende-type *d-p* lattice model using the electronic structure parameters deduced from the CI local-cluster analysis.

As discussed in the previous section, while the Mn^{2+} impurity shows the antiferromagnetic (AFM) *p-d* exchange interaction, the Cr^{2+} impurity has the ferromagnetic (FM) *p-d* exchange interaction. Therefore, it is interesting to compare the magnetic structure of zinc-blende MnTe with that of CrTe. Experimentally, the zinc-blende MnTe has artificially been synthesized by molecular-beam epitaxy and shows a magnetic structure of the AFM-III type [Ando *et al.*, 1992, 1993]. On the other hand, zinc-blende-type CrTe has never been obtained. Here, we have performed the unrestricted HF calculations for MnTe and hypothetical CrTe. The input parameters are $\Delta = 2.0$ eV, $U = 4.0$ eV and $(pd\sigma) = -1.0$ eV for MnTe and $\Delta = 3.0$ eV, $U = 3.5$ eV and $(pd\sigma) = -1.0$ eV for CrTe. $(pp\sigma)$ and $(pp\pi)$, which are transfer integrals between Te 5*p* orbitals, are fixed at 1.0 eV and -0.25 eV, respectively. In table 7.4, total energies per unit formula of the AFM-I, AFM-II, AFM-III and FM states are compared for MnTe and CrTe. For MnTe, the AF-III state is predicted to be the ground state, which agrees with the experimental result. The AF-I and AF-III are almost degenerate and the AFM-II and FM states are higher in energy. The similar result has been obtained by Wei and Zunger [1993] by the *ab-initio* LSDA calculation. Character of the band gap is of the typical charge-transfer type. On the other hand, for CrTe, the HF calculation predicts that the FM state has the lowest energy and that the AFM states are higher in energy. The FM versus AFM behavior obtained by the HF calculation reflects the sign of the *p-d* exchange constant in the dilute limit.

The densitiy of states for MnTe (AFM-III) and CrTe (FM) obtained from the HF calculation on the lattice model are shown in Fig. 7.10. In MnTe, Δ_{eff} is very large compared with Δ because the d^5 configuration is stabilized by the large intra-atomic exchange energy. Therefore the charge-transfer-type band gap of ~ 3 eV opens between the occupied Te 5*p* orbitals and the unoccupied Mn 3*d* orbitals. On the other hand, in CrTe, Δ_{eff} is smaller than Δ because the $d^5\underline{L}$ configuration is stabilized by the exchange energy and the d^4 configuration is not. As a result, zinc-blende CrTe is predicted to be metallic in the HF calculation.

Table 7.5. Relative total energies per unit formula of the FM, AFM-I, AFM-II and AFM-III configurations (in meV) for zinc-blende-type MnTe and CrTe

	relative total energies			
	FM	AFM-I	AFM-II	AFM-III
MnTe	0.0	-92.5	-71.3	-94.1
CrTe	0.0	240.0	187.1	255.9

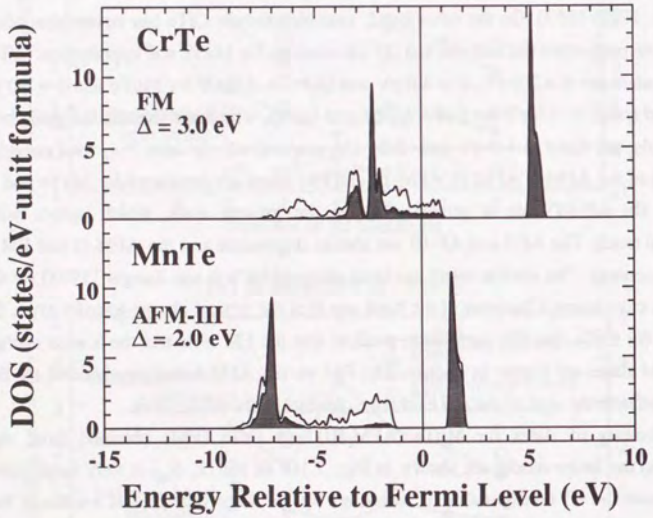

Fig. 7.9. Density of states for zinc-blende-type MnTe and CrTe calculated by the HF approximation.

7.5. Conclusion

We have shown that the various experimental results on the 3*d* transition-metal impurities in II-VI semiconductors can be consistently explained in the CI picture: the *d-d* optical absorption, photoemission and inverse-photoemission spectra and donor and acceptor ionization energies can be reproduced with a single set of parameters, Δ, U and $(pd\sigma)$. It is shown that the physical properties are controlled largely both by the smooth variation of Δ as a function of impurity atomic number and by the apparently irregular variation of Δ_{eff} due to the multiplet effects. The variation of the *p-d* exchange constant is also qualitatively explained. The electronic structures of the 3*d* transition-metal chalcogenides have been studied by the unrestricted HF calculations and have been discussed in comparison with those of the 3*d* transition-metal impurities in II-VI semiconductors. Application of the present method with more realistic model to a wider range of impurity systems as well as to the calculation of other physical properties remain to be made in future.

Chapter eight

Concluding remarks

In this thesis, the electronic structures of the perovskite-type 3*d* transition-metal oxides and 3*d* transition-metal impurities in II-VI semiconductors, in which both the *d*-*d* Coulomb interaction and the *d*-ligand hybridization are strong, have been studied experimentally and theoretically.

In Chapter 3, the electronic structure of formally Ni^{3+} (d^7) $PrNiO_3$, which shows metal-insulator transition as a function of temperature, has been investigated by photoemission and x-ray absorption spectroscopy. The local-cluster analyses of the photoemission spectra have provided us with the electronic structure parameters: the oxygen 2*p*-to-transition-metal 3*d* charge-transfer energy, the 3*d*-3*d* Coulomb interaction energy and the transfer integral between the oxygen 2*p* and transition-metal 3*d* orbitals. The charge-transfer energy was estimated to be ~ 1.0 eV. It has been found that the d^7 and $d^8\underline{L}$ configurations are strongly hybridized in the ground state. The HF band-structure calculations on the perovskite-type lattice model using the electronic-structure parameters have revealed that the $GdFeO_3$-type lattice distortion enlarges the magnitude of the band gap and have given us a picture of the metallic versus insulating behavior of $RNiO_3$ system. However, we could not find a HF solution which is consistent with the spin and orbital ordering obtained from the neutron diffraction measurement [García-Muños *et al.*, 1994].

In Chapter 4, the electronic structure of formally Cu^{3+} (d^8) $LaCuO_3$ have been studied by the photoemission and x-ray absorption spectroscopy and subsequent local-cluster and HF band-structure calculations. From the local-cluster analysis of the photoemission spectra, the charge-transfer energy was estimated to be ~ -1.0 eV. It has been found that the ground state mainly has $d^9\underline{L}$ character into which d^8 character is strongly mixed. The Cu 2*p* XAS spectra which could not be explained by the local-cluster calculation, indicates that the intercluster interaction is important. On the other hand, the HF band-structure calculation on the lattice models cannot explain the satellite structure of the photoemission spectra, suggesting the correlation effect beyond the HF approximation is strong. Although the local self-energy correction to the HF solution somewhat improved the agreement with the photoemission spectra, the observed intensity at the Fermi level is strongly suppressed compared with the calculation.

In Chapter 5, the spin- and orbital-unrestricted HF calculations on the perovskite-type *d*-*p* models have been presented. The interplay between the spin and orbital ordering and the $GdFeO_3$-type and Jahn-Teller-type lattice distortions has extensively been studied for $RTiO_3$ and RVO_3, where t_{2g} subshell is partially filled, and $RMnO_3$ and $RNiO_3$, where e_g subshell is partially occupied. Based on the HF calculation, the experimental results on the ground states of the perovskite-type 3*d* transition-metal oxides have been explained in an unified way. However, as for the magnitude of the band gap and valence-band photoemission spectrum, the HF calculation failed to reproduce the experimental results.

It is very interesting to study the effect of the orbital ordering and lattice distortions on the metal-insulator transitions of the doped 3*d* transition-metal oxides such as $Y_{1-x}Ca_xTiO_3$, $La_{1-x}Sr_xVO_3$ and $La_{1-x}Sr_xMnO_3$. Angle-resolved photoemission spectroscopy of well-characterized surfaces of the 3*d* transition-metal oxides will give us many important pieces of information on the orbital ordering and orbital fluctuation.

In Chapter 6, the effect of the self-energy correction to the Hartree-Fock solution has systematically been investigated by calculating the self-energy up to second order in the 3*d*-3*d* Coulomb interaction. It has been shown that the photoemission spectra of the insulating 3*d* transition-metal oxides of the Mott-Hubbard and charge-transfer types are well reproduced by the self-energy correction using the local approximation which neglects the momentum dependence of the self-energy. The remnant of the lower Hubbard band, which have been observed in some PM metallic 3*d* transition-metal oxides, has also been obtained. The validity of the local approximation has been checked by the expansion around the local limit. It has been shown that the effects of the momentum dependence of the self-energy is large in the one-dimensional CuO_3 chain and is small in the two-dimensional CuO_2 plane. The intensity at the Fermi level calculated using the local self-energy correction was too strong compared with that observed in some PM metallic 3*d* transition-metal oxides including $LaCuO_3$. The effect of the inter-site Coulomb interaction has also been investigated using the HF calculation in order to explain the small spectral weight at the Fermi level.

It is important to study the effect of the long-range Coulomb interaction on the electronic structure of the 3*d* transition-metal compounds. In order to give an answer to this problem, we have to systematically take photoemission spectra of 3*d* transition-metal compounds including chalchogenides and oxides, where the screening by the ligand ions are expected to be different, and carefully analyze the data using the model calculation where the inter-site Coulomb interaction and screening effect by the ligand ions are explicitly included.

In Chapter 7, the electronic structures of the substitutional 3*d* transition-metal impurities in semiconductors have been studied mainly using the configuration-interaction local-cluster calculation. The electronic structure of the 3*d* transition-metal chalcogenides, which can be viewed as 100% substituted limit, have been discussed using HF band-structure calculation. These calculations give us a rough picture to link the electronic structure of the impurity limit, in which the local-cluster approach works well, to that of the 3*d* transition-metal compounds.

The local-cluster approach is useful to describe the photoemission spectra of the 3*d* transition-metal compounds studied in the present work. The HF solution of the lattice model, in which the output of the cluster-model analyses is used as input, is a good starting point to study the relationship between their various ground-state physical properties and electronic structures. The self-energy correction to the HF solution is promising to explain their ground-state properties and photoemission spectra in a unified way. Efforts along these lines should be continued in future in order to bridge between the local-cluster picture and band picture and to

give further understanding of the electronic structure of the 3*d* transition-metal compounds in which both the *d*-*d* Coulomb interaction and the *d*-ligand hybridization are strong.

Acknowledgment

It would have been impossible to perform the present work if many people had not given me support, advice and useful discussions. It is my great pleasure to express my gratitude to the following people.

First of all, I would like to thank Prof. Atsushi Fujimori for providing me with an opportunity to have performed the present work and for continuos support. I am grateful to Prof. Hirohumi Namatame for introducing me to the experimental techniques.

I would like to express my gratitude to Dr. Takahisa Arima, Prof. Yoshinori Tokura and Prof. Nobuo Mori for the collaboration in the work on $PrNiO_3$. I have to thank Prof. Jun Akimitsu for the collaboration in the work on $PrNiO_3$ and the stimulating discussions on the orbital ordering in $YTiO_3$. I am grateful to Prof. Yasuo Takeda and Prof. Mikio Takano for the collaboration in the work on $LaCuO_3$.

I would like to thank Prof. Akira Yagishita and the staff of Photon Factory, for the technical support in the XAS measurement. I have to thank Dr. Yasuhisa Tezuka and Prof. Sik Shin and the staff of the Synchrotron Radiation Laboratory, Institute for Solid State Physics for the technical support in the resonant photoemission measurement.

It is my pleasure to thank Prof. Dipankar D. Sarma for valuable discussions during his stay in Tokyo last winter. I would like to thank Dr. Vladimir I. Anishimov and Dr. Miguel Abbate for useful discussions on the electronic structure of the 3*d* transition-metal oxides. I would like to express my gratitude to Prof. George A. Sawatzky for valuable and general suggestions on the electronic structure of the 3*d* transition-metal oxides.

I am grateful to Prof. Akio Kotani and Dr. Kozo Okada for the valuable discussions on the cluster-model analysis of the photoemission spectra. I would like to thank Dr. Hiroshi Eisaki for introducing me to the physical properties of the 3*d* transition-metal oxides.

It is my pleasure to thank Dr. Koukichi Tomimoto, Dr. Noriaki Hamada, Dr. Hideaki Sawada, Dr. Igor V. Solevyev for useful discussions on orbital ordering in perovskite-type transition-metal oxides.

I would like to express my gratitude to Dr. Hiroshi Kohno and Prof. Hidetoshi Fukuyama for enlightening discussions on the effect of electron correlation in the 3*d* transition-metal compounds.

I would like to thank Prof. Katsuaki Sato, Dr. Koji Ando, Dr. Hiroaki Anno, Dr. Hitoshi Sato and Prof. Masaki Taniguchi for stimulating discussions on the electronic structure of 3*d* transition-metal impurities in II-VI semiconductors.

I have to thank Dr. Keiji Morikawa, Dr. Isao H. Inoue, Dr. Tomohiko Saitoh and Dr. Kenya Shimada, who are studying electronic structure of the 3*d* transition-metal oxides and chalcogenides with Fujimori group and sharing interest with me, for their helps and stimulating

discussions. I am also grateful to other present and previous members of Fujimori group, Dr. Shin-ichi Nohara, Dr. Motohiko Nakamura, Dr. Katsuhiko Yamaguchi, Dr. Antoine E. Bocquet, Dr. Oliver Rader, Mr. Izumi Hase, Mr. Kazutoshi Mamiya, Mr. Akira Sekiyama, Mr. Kengo Fujioka, Mr. Takehisa Konishi, Mr. Akihiro Ino, Mr. Kensuke Kobayashi, Mr. Jin-Young Son, Mr. Jun Okamoto, Mr. Tomofumi Susaki and Mr. Toshiyuki Tsujioka for their support and encouragement. I am thankful to Ms. Yoko Sasaki, Ms. Yumiko Takano and Ms. Hazuki Wakazono for their support.

Finally, I am very grateful to all those whose name are not mentioned here but who helped me a lot.

Part of the calculations in this work were performed on a VAX computer in Meson Science Laboratory, University of Tokyo. The present work is supported by a Grant-in-Aid for Scientific Research from the Ministry of Education, Science and Culture.

Appendix I: Matrix elements of $3d$-$3d$ Coulomb interaction

Relationships between Racah parameters and Slater integrals:

$A = F^0 - 49/441F^4$

$B = 1/49F^2 - 5/441F^4$

$C = 35/441F^4$

A, B, C: Racah parameters

F^0, F^2, F^4: Slater integrals

Relationships between Kanamori parameters:

$u = A + 4B + 3C$

$j = 5/2B + C$

u, u', j, j' ($u' = u - 2j$, $j' = j$): Kanamori parameters

$u \equiv <$ m m $|\ e^2/r\ |$ m m$>$

$u' \equiv <$ m m' $|\ e^2/r\ |$ m m'$>$

$j \equiv <$ m m' $|\ e^2/r\ |$ m' m$>$

$j' \equiv <$ m m $|\ e^2/r\ |$ m' m'$>$

m, m': ξ, η, ζ, u, and v

Table I.1. Matrix elements $<$ m m' $|\ e^2/r\ |$ m m'$>$ (m, m': ξ, η, ζ, u, and v) in terms of Racah parameters and Kanamori parameters.

m \ m'	ξ	η	ζ	u	v
ξ	$A+4B+3C$	$A-2B+C$	$A-2B+C$	$A+2B+C$	$A-2B+C$
	u	u'	u'	u'	u'
η		$A+4B+3C$	$A-2B+C$	$A+2B+C$	$A-2B+C$
		u	u'	u'	u'
ζ			$A+4B+3C$	$A-4B+C$	$A+4B+C$
			u	u'	u'
u				$A+4B+3C$	$A-4B+C$
				u	u'
v					$A+4B+3C$
					u

Table I.2. Matrix elements < m m' | e^2/r | m m'> (m, m': l_z) in terms of Racah parameters and Kanamori parameters.

m \ m'	2	1	0	-1	-2
2	$A+4B+2C$	$A-2B+C$	$A-4B+C$	$A-2B+C$	$A+4B+2C$
	$(u+u')/2$	u'	u'	u'	$(u+u')/2$
1		$A+B+2C$	$A+2B+C$	$A+B+2C$	$A-2B+C$
		$(u+u')/2$	u'	$(u+u')/2$	u'
0			$A+4B+3C$	$A+2B+C$	$A-4B+C$
			u	u'	u'
-1				$A+B+2C$	$A-2B+C$
				$(u+u')/2$	u'
-2					$A+4B+2C$
					$(u+u')/2$

Table I.3. Matrix elements < m m' | e^2/r | m' m> (m, m': ξ, η, ζ, u, and v) in terms of Racah parameters and Kanamori parameters.

m \ m'	ξ	η	ζ	u	v
ξ		$3B+C$	$3B+C$	$B+C$	$3B+C$
		j	j	j	j
η			$3B+C$	$B+C$	$3B+C$
			j	j	j
ζ				$4B+C$	C
				j	j
u					$4B+C$
					j
v					

Table I.4. Matrix elements < m m' | e^2/r | m' m> (m, m': l_z) in terms of Racah parameters and Kanamori parameters.

m \ m'	2	1	0	-1	-2
2		$6B+C$	$4B+C$	C	$2C$
		j	j	j	$2j$
1			$B+C$	$-6B+2C$	C
			j	$2j$	j
0				$B+C$	$4B+C$
				j	j
-1					$6B+C$
					j
-2					

Matrix elements < m m' | e^2/r | m'' m'''> :

$< \xi\ \eta \mid e^2/r \mid \zeta\ u > = < \xi\ \eta \mid e^2/r \mid u\ \zeta > = \sqrt{3}B$

$< \xi\ \eta \mid e^2/r \mid \zeta\ v > = -< \xi\ \eta \mid e^2/r \mid v\ \zeta > = 3B$

$< \zeta\ \xi \mid e^2/r \mid \upsilon\ \eta > = -2\sqrt{3}B$

$< \xi\ u \mid e^2/r \mid x\ v > = -< \eta\ u \mid e^2/r \mid \eta\ v > = 2\sqrt{3}B$

$< \xi\ u \mid e^2/r \mid v\ \xi > = -< \eta\ u \mid e^2/r \mid v\ \eta > = -\sqrt{3}B$

< m m' | e^2/r | m'' m'''> does not change its value by the exchange m ↔ m' and m'' ↔ m''' or m ↔ m'' and m' ↔ m'''.

Appendix II: Matrix elements of the lowest terms $E(d^n)$, the charge-transfer energy Δ_{eff} and the d-d Coulomb interaction U_{eff}

Table II.1. Matrix elements of the lowest terms $E(d^n)$, the charge-transfer energy Δ_{eff} and the d-d Coulomb interaction U_{eff} in terms of Racah parameters [Kamimura *et al.*, 1969].

d^n (O_h, T_d)	$E(d^n)$	Δ_{eff}	U_{eff}
d^1 ($^3T_{2g}$, ^2E)		Δ_0 - 8B	A - 8B
d^2 ($^3T_{1g}$, $^3A_2$)	A - 8B	Δ_0 - 7B	A + B
d^3 ($^4A_{2g}$, $^4T_1$)	3A - 15B	Δ_0 - 6B	A + B
d^4 ($^5T_{1g}$, $^5T_2$)	6A - 21B	Δ_0 - 14B	A - 8B
d^5 ($^6A_{1g}$, $^6A_1$)	10A - 35B	Δ_0 - 7C	A + 14B + 7C
d^6 ($^5T_{2g}$, ^5E)	15A + (-14B+7C) - 21B	Δ_0 - 8B + 7C	A - 8B
d^7 ($^4T_{1g}$, $^4A_2$)	21A + 2(-14B+7C) - 15B	Δ_0 - 7B + 7C	A + B
d^8 ($^3A_{2g}$, $^3T_1$)	28A + 3(-14B+7C) - 8B	Δ_0 - 6B + 7C	A + B
d^9 (^2E_g, $^2T_2$)	36A + 4(-14B+7C)	Δ_0 - 14B + 7C	A - 8B

Table II.2. Matrix elements of the lowest terms $E(d^n)$, the charge-transfer energy Δ_{eff} and the d-d Coulomb interaction U_{eff} in terms of Kanamori parameters.

d^n	$E(d^n)$	Δ_{eff}	U_{eff}
d^1		Δ_0 - 7/2B	A - 7/2B
d^2	u' - j	Δ_0 - 7B	A - 7/2B
d^3	3u' -3j	Δ_0 - 21/2B	A - 7/2B
d^4	6u' - 6j	Δ_0 - 14B	A - 7/2B
d^5	10u' - 10j	Δ_0 - 7C	A + 14B + 7C
d^6	u + 14u' - 10j	Δ_0 - 7/2B + 7C	A - 7/2B
d^7	2u + 19u' - 11j	Δ_0 - 7B + 7C	A - 7/2B
d^8	3u + 25u' - 13j	Δ_0 - 21/2B + 7C	A - 7/2B
d^9	4u + 32u' - 16j	Δ_0 - 14B + 7C	A - 7/2B

Appendix III: Ligand field due to non-orthogonality for the octahedral and tetrahedral clusters

Since the octahedral MX_6 (M: transition metal, X: ligand) cluster has the point group symmetry O_h, the 3d orbitals are reduced into the orbitals with t_{2g} (yz, zx, xy) and e_g ($3z^2$-r^2, x^2-y^2) symmetries. The transfer and overlap integrals between the 3d orbitals and the ligand molecular orbitals with t_{2g} and e_g symmetries constructed from the ligand p orbitals are shown below.

transfer integrals:

$$V_{t2} = \langle L_{yz}|H_{pd}|d_{yz}\rangle = \langle L_{zx}|H_{pd}|d_{zx}\rangle = \langle L_{xy}|H_{pd}|d_{xy}\rangle = 2(pd\pi)$$
$$V_e = \langle L_{x^2-y^2}|H_{pd}|d_{x^2-y^2}\rangle = \langle L_{3z^2-r^2}|H_{pd}|d_{3z^2-r^2}\rangle = -\sqrt{3}\,(pd\sigma)$$

overlap integrals:

$$S_{t2} = \langle L_{yz}|d_{yz}\rangle = \langle L_{zx}|d_{zx}\rangle = \langle L_{xy}|d_{xy}\rangle = 2S_\pi$$
$$S_e = \langle L_{x^2-y^2}|d_{x^2-y^2}\rangle = \langle L_{3z^2-r^2}|d_{3z^2-r^2}\rangle = -\sqrt{3}\,S_\sigma$$

Since the tetrahedral MX_4 cluster has the point group symmetry T_d, the 3d orbitals are reduced into the orbitals with t_2 (yz, zx, xy) and e ($3z^2$-r^2, x^2-y^2) symmetries. We have a set of ligand molecular orbitals with e symmetry and two sets of ligand molecular orbitals with t_2 symmetry in the tetrahedral MX_4 cluster. We can construct six ligand orbitals from the ligand molecular orbitals with t_2 symmetry: The transfer integrals between three of them and the 3d orbitals are zero and those between the other three and the 3d orbitals are finite. If we neglect the interaction between the former three ligand orbitals and the latter three, the transfer and overlap integrals between the 3d orbitals and the ligand molecular orbitals are given as those in the octahedral cluster.

transfer integrals:

$$V_{t2} = \langle L_{yz}|H_{pd}|d_{yz}\rangle = \langle L_{zx}|H_{pd}|d_{zx}\rangle = \langle L_{xy}|H_{pd}|d_{xy}\rangle = \sqrt{4/3(pd\sigma)^2+8/9(pd\pi)^2}$$
$$V_e = \langle L_{x^2-y^2}|H_{pd}|d_{x^2-y^2}\rangle = \langle L_{3z^2-r^2}|H_{pd}|d_{3z^2-r^2}\rangle = 2\sqrt{6}\,/3(pd\pi)$$

overlap integrals:

$$S_{t2} = \langle L_{yz}|d_{yz}\rangle = \langle L_{zx}|d_{zx}\rangle = \langle L_{xy}d_{xy}\rangle = -\sqrt{4/3S_\sigma{}^2+8/9S_\pi{}^2}$$
$$S_e = \langle L_{x^2-y^2}|d_{x^2-y^2}\rangle = \langle L_{3z^2-r^2}|d_{3z^2-r^2}\rangle = 2\sqrt{6}\,/3S_\pi$$

If we use the atomic orbitals to construct the ligand molecular orbitals without orthogonalizing procedures, the overlap integrals of the orbitals on the adjacent sites cannot be neglected. When we consider the overlap integrals between the transition-metal $3d$ orbitals and the ligand $2p$ orbitals, the ligand field $10Dq$ due to non-orthogonality is evaluated in terms of the overlap integrals and the transfer integrals using the relation $\langle 0|p_m d_m\, H_{pd}\, d_m^{+} p_m^{+}|0\rangle = -2V_m S_m$. The ligand field $10Dq$ for the octahedral and tetrahedral clusters is given by

$$10Dq = \langle d_{x^2-y^2} L_{x^2-y^2}|H_{pd}|d_{x^2-y^2} L_{x^2-y^2}\rangle - \langle d_{yz} L_{yz}|\, H_{pd}|d_{yz} L_{yz}\rangle$$
$$= -2(S_e V_e - S_{t2} V_{t2}) \ ,$$

which is positive for the octahedral cluster and negative for the tetrahedral cluster. It should be noted that the signs of the transfer and overlap integrals depend on the definitions [Here, $(pd\sigma)<0$, $(pd\pi)>0$, $S_\sigma>0$, $S_\pi<0$].

References

Abbate, M., F. M. F. de Groot, J. C. Fuggle, A. Fujimori, O. Strebel, F. Lopez, M. Domke, G. Kaindl, G. A. Sawatzky, M. Takano, Y. Takeda, H. Eisaki, and S. Uchida, 1992, Phys. Rev. B **46**, 3771.

Abbate, M., J. C. Fuggle, A. Fujimori, L. H. Tjeng, C. T. Chen, R. Potze, G. A. Sawatzky, H. Eisaki, and S. Uchida, 1993, Phys. Rev. B **47**, 16124.

Ando, K., K. Takahashi, and T. Okuda, 1992a, J. Magn. Magn. Mater. **104-107**, 993.

Ando, K., K. Takahashi, T. Okuda, and M. Umehara, 1992b, Phys. Rev. B **46**, 12289.

Anisimov, V. I., J. Zaanen, and O. K. Andersen, 1991, Phys. Rev. B **44**, 943.

Appeli, G., and Z. Fisk, 1992, Comments Condens. Matter Phys. **16**, 155.

Ashkenazi, J., and M. Weger, 1973, Adv. Phys. **22**, 207.

Arai, M., and T. Fujiwara, 1995, Phys. Rev. B **51**, 1477.

Arima, T., Y. Tokura, and J. B. Torrance, 1993, Phys. Rev. B **48**, 17006.

Aryasetiawan, F., and O. Gunnarsson, 1995, Phys. Rev. Lett. **74**, 3221.

Barman, S. R., A. Chainani, and D. D. Sarma, 1994, Phys. Rev. B **49**, 8475.

Bednorz, J. G., and K. A. Müller, 1986, Z. Phys. B **64**, 189.

Bhattacharjee, A. K., 1994, Phys. Rev. B **49**, 13987.

Bocquet, A. E., A. Fujimori, T. Mizokawa, T. Saitoh, H. Namatame, S. Suga, N. Kimizuka, Y. Takeda, and M. Takano, 1992a, Phys. Rev. B **45**, 1561.

Bocquet, A. E., T. Mizokawa, T. Saitoh, H. Namatame, and A. Fujimori, 1992b, Phys. Rev. B **46**, 3771.

Bocquet, A. E., T. Mizokawa, K. Morikawa, A. Fujimori, S. R. Barman, K. Maiti, D. D. Sarma, Y. Tokura, and M. Onoda, 1995, Phys. Rev. B, **52**, 13838.

Bordet, P., C. Chaillout, M. Marezio, Q. Huang, A. Santoro, S-W. Cheong, H. Takagi, C. S. Oglesby, and B. Batlogg, 1993, J. Sold State Chem. **106**, 253.

Bouhelal, A., and J. P. Albert, 1989, Solid State Commun. **69**, 713.

Brandow, B. H., 1977, Adv. Phys. **26**, 651.

Bringley, J. F., B. A. Scott, S. J. La Placa, R. F. Boehme, T. M. Shaw, M. W. McElfresh, S. S. Trail, and D. E. Cox, 1990, Nature **347**, 263.

Bringley, J. F., B. A. Scott, S. J. La Placa, T. R. McGuire, F. Mehran, M. W. McElfresh, and D. E. Cox, 1993, Phys. Rev. B **47**, 15269.

Calandra, C., and F. Manghi, 1992, Phys. Rev. B **45**, 5819.

Cardona, M., and L. Ley, 1978, in *Photoemission in Solids I*, edited by M. Cardona and L. Ley (Spliger-Verlag, Berlin), p. 1.

Castellani, C., C. R. Natoli, and J. Ranninger, 1975, Phys. Rev. B **18**, 4945.

Chainani, A., M. Mathew, and D. D. Sarma, 1992, Phys. Rev. B **46**, 9976.

Chainani, A., M. Mathew, and D. D. Sarma, 1993, Phys. Rev. B **47**, 15397.

Chen, C. T., F. Sette, Y. Ma, M. S. Hybertsen, E. B. Stechel, W. M. C. Foulkes, M. Schluter, S-W. Cheong, A. S. Cooper, L. W. Rupp, Jr., B. Batlogg, Y. L. Soo, Z. H. Ming, A. Krol, and Y. H. Kao, 1991, Phys. Rev. Lett. **66**, 104.

Chen, C. T., L.H. Tjeng, J. Kwo, H. L. Kao, P. Rudolf, F. Sette and R. M. Fleming, 1992, Phys. Rev. Lett. **68**, 2543.

Chen, X. M., and A. W. Overhauser, 1991, Phys. Rev. B **43**, 14182.

Crandles, D. A., T. Timusk, J. D. Garrett, and J. E. Greedan, 1992, Physica C **201**, 407.

Cyrot, M., and C. Lyon-Caen, 1975, J. Phys. (Paris) **36**, 253.

Czyzyk, M. T., and G. A. Sawatzky, 1994, Phys. Rev. B **49**, 14211.

de Boer, H. J., and E. J. W. Verwey, 1937, Proc. Phys. Soc. **49**, 59.

de Groot, F. M. F., M. Grioni, J. C. Fuggle, J. Ghijsen, G. A. Sawatzky, and H. Petersen, 1989, Phys. Rev. B **40**, 5715.

de Groot, F. M. F., J. C. Fuggle, B. T. Tole and G. A. Sawatzky, 1990, Phys. Rev. B **40**, 5715.

Demazeau, G., C. Parent, M. Pouchard, and P. Hagenmuller, 1972, Matter. Res. Bull. **7**, 913.

Drracq, S., S. Matar, and G. Demazeau, 1993, Solid State Commun. **85**, 961.

Eisaki, H., 1992, Thesis (University of Tokyo).

Elemans, J. B. A. A., B. van Laar, K. R. vander Veen, and B. O. Loopstra, 1971, J. Solid State Chem. **3**, 328.

Eskes, H., and G. A. Sawatzky, 1988, Phys. Rev. Lett. **61** 1415.

Eskes, H., L. H. Tjeng, and G. A. Sawatzky, 1990, Phys. Rev. B **41**, 288.

Fazzio, A., M. J. Caldas, and A. Zunger, 1984, Phys. Rev. B **30**, 3430.

Franciosi, A., A. Wall, Y. Gao, J. H. Weaver, M. H. Tai, J. D. Dow, R. U. Kasowski, R. Reifenberger, and F. Pool, 1989, Phys. Rev. B **40**, 12009.

Fuggle, J. C., 1992, in *Unoccupied Electronic States*, edited by J. C. Fuggle and J. E. Inglesfield (Springer-Verlag, Berlin).

Fujishima, Y., Y. Tokura, T. Arima, and S. Uchida, 1992, Phys. Rev. B **46**, 11167.

Fujimori, A., and F. Minami, 1984, Phys. Rev. B **30**, 957.

Fujimori, A., E. Takayama-Muromachi, Y. Uchida, and B. Okai, 1987, Phys. Rev. B **35**, 8814.

Fujimori, A., Y. Tokura, H. Eisaki, H. Takagi, S. Uchida, and M. Sato, 1989a, Phys. Rev. B **39**, 793.

Fujimori, A., S. Takekawa, E. Takayama-Muromachi, Y. Uchida, A. Ono, T. Takahashi, Y. Okabe, and H. Katayama-Yoshida, 1989b, Phys. Rev. B **39**, 2255.

Fujimori, A., I. Hase, H. Namatame, Y. Fujishima, Y. Tokura, H. Eisaki, S. Uchida, K. Takegahara, and F. M. F. de Groot, 1992a, Phys. Rev. Lett. **69**, 1796.

Fujimori, A., I. Hase, H. Namatame, Y. Fujishima, Y. Tokura, M. Abbate, F. M. F. de Groot, M. T. Czyzyk, J. C. Fuggle, O. Strebel, F. Lopez, M. Domke, and G. Kaindl, 1992b, Phys. Rev. B **46**, 9841.

Furdyna, J. K., 1988, J. Appl. Phys. **64**, R29.

Gagliano, E. R., and C. A. Balseiro, 1988, Phys. Rev. B **38**, 11766.

García-Muñoz, J. L., J. Rodríguez-Carvajal, P. Lacorre, and J. B. Torrance, 1992a, Phys. Rev. B **46**, 4414.

García-Muñoz, J. L., J. Rodríguez-Carvajal, and P. Lacorre, 1992b, Europhys. Lett. **20**, 241.

García-Muñoz, J. L., J. Rodríguez-Carvajal, and P. Lacorre, 1994, Phys. Rev. B **50**, 978.

Garret, J. D., and J. E. Greedan, 1981, Inorg. Chem. **20**, 1025.

Georges, A., and G. Kotliar, 1992, Phys. Rev. B **45**, 6479.

Ghijsen, J., L. H. Tjeng, J. van Elp, H. Eskes, J. Westerink, G. A. Sawatzky, and M. T. Czyzyk, 1988, Phys.Rev.B **38** 11322.

Goodenough, J. B.,1955 , Phys. Rev. **100**, 564.

Goodenough, J. B., A. Wold, R. J. Aronott, and N. Menyuk, 1961, Phys. Rev. **124**, 373.

Goodenough, J. B., and P. Raccah, 1965, J. Appl. Phys. **36**, 1031.

Goral, J. P., J. E. Greedan, and D. A. MacLean, 1982, J. Solid State Chem. **43**, 244.

Goral, J. P., and J. E. Greedan, 1983, J. Mag. Mag. Mat. **37**, 315.

Grant, J. B., and A. K. McMahan, 1991, Phys. Rev. Lett. **66**, 488.

Grant, J. B., and A. K. McMahan, 1992, Phys. Rev. B **46**, 8440.

Grebe, G., and H. J. Schulz, 1972, Phys. Status Solidi B **54**, K69.

Grebe, G., G. Roussos, and H. J. Schulz, 1976, J. Phys. C **9**, 4511.

Greeff, C. W., H. R. Glyde, and B. E. Clements, 1992, Phys. Rev. B **45**, 7951.

Griffith, J. S., 1971, *The Theory of Transition Metal Ions* (Cambridge, London).

Grioni, M., J. B. Goedkoop, R. Schoorl, F. M. F. de Groot, J. C. Fuggle, F. Schäfers, E. E. Koch, G. Rossi, J.-M. Esteva, and R. C. Karnatak, 1989, Phys. Rev. B **39**, 1541.

Gunnarsson, O., and K. Schönhammer, 1987, in *Handbook on the Physics and Chemistry of Rare Earths*, Vol. 10, edited by K. A. Gschneider, Jr., L. Eyring and S. Hüfner (Elsevier, Amstrdam), Chap. 64.

Gunnarsson, O., and O. Jepsen , 1988, Phys. Rev. B **38**, 3568.

Gunnarsson, O., O. K. Anderson, O. Jepsen, and J. Zaanen, 1989, Phys. Rev. B **39**, 1708.

Haldane, F. D. M., and P. W. Anderson, 1976, Phys. Rev. B **13**, 2553.

Ham, F. S., and G. A. Slack, 1971, Phys. Rev. B **4**, 777.

Hamada, N., H. Sawada, and K. Terakura, 1995, in *Spectroscopy of Mott Insulators and Correlated Metals*, edited by A. Fujimori and Y. Tokura, (Splinger-Verlag, Berlin), p. 95.

Hamdani, F., J. P. Lascaray, D. Coquillat, A. K. Bhattacharjee, M. Nawrocki, and Z. Golacki, 1992, Phys. Rev. B **45**, 13298.

Harrison, W. A., 1989, *Electronic Structure and the Properties of Solids* (Dover, New York).

Hass, K. C., 1991, in *Semimagnetic Semiconductors and Diluted Magnetic Semiconductors*, edited by M. Averous and M. Balkanski (Plenum, New York), p. 59.

Hoang, Le. M., and J. M. Baranowski, 1977, Phys. Status Solidi B **84**, 361.

Hubbard, J., 1963, Proc. R. Soc. London A **276**, 238.

Hubbard, J., 1964a, Proc. R. Soc. London A **277**, 237.

Hubbard, J., 1964b, Proc. R. Soc. London A **281**, 401.

Hüfner, S., J. Osterwalder, T. Riesterer, and F. Hullinger, 1984, Solid State Commun. **52**, 793.

Hüfner, S., 1985, Z. Phys. B **61**, 135.

Hüfner, S., 1995, *Phtoelectron Spectroscopy* (Splinger-Verlag, Berlin).

Hutchings, M. T., E. J. Samuelsen, G. Shirane, and K. Hirakawa, 1969, Phys. Rev. B **188**, 919.

Inagaki, S., and R. Kubo, 1973, Int. J. Magn. **4**, 139.

Inagaki, S., 1975, J. Phys. Soc. Jpn. **39**, 596.

Ino, A., *et al.*, 1995, unpublished.

Inoue, I. H., I. Hase, Y. Aiura, A. Fujimori, Y. Haruyama, T. Maruyama, and Y. Nishihara, 1995, Phys. Rev. Lett. **74**, 2539.

Jang, Y.-R., and B. I. Min, 1993, Phys. Rev. B **48**, 1914.

Jarrell, M., 1992, Phys. Rev. Lett. **69**, 168.

Jonker, G. H., and J. H. van Santen, 1950, Physica **16**, 337.

Jonker, G. H., and J. H. van Santen, 1953, Physica **19**, 120.

Kamimura, H., S. Sugano, and Y. Tanabe, 1969, *Ligand Field Theory and Its Applications* (Syokabo, Tokyo) in Japanese.

Kanamori, J., 1959, J. Phys. Chem. Solids, **10**, 87.

Kanamori, J., 1963, Prog. Theor. Phys. **30**, 275.

Katayama-Yoshida, H., and A. Zunger, 1986, Phys. Rev. B **33**, 2961.

Kawano, H., H. Yoshizawa, and Y. Ueda, 1994, J. Phys. Soc. Jpn. **63**, 2857.

Kelly, C. S., and F. Williams, 1970, Phys. Rev. B **2**, 3.

Kemp, J. P., and P. A. Cox, 1990, Solid State Commun. **75**, 731.

Khurana, A., 1989, Phys. Rev. B **40**, 4216.

Koehler, W. C. , and E. O. Wollan, 1957, J. Phys. Chem. Solids **2**, 100.

Koidl, P., O. F. Schirmer, and U. Kaufmann, 1973, Phys. Rev. B **8**, 4926.

Korotin, M. A., S. Yu. Ezhov, I. V. Solovyev, V. I. Anisimov, D. I. Khomskii, and G. A. Sawatzky, 1995, submitted to Phys. Rev. B.

Kotani, A., 1987, in *Handbook of Synchrotron Radiation*, Vol. 2, edited by G. V. Marr (Elsevier, Amstrdam, 1987), Chap. 9.

Krause, M. O., and J. H. Oliver, 1979, J. Phys. Chem. Ref. Data **8**, 329.

Kugel, K. I., and D. I. Khomskii, 1973, Sov. Phys.-JETP **37**, 725.

Kugel, K. I., and D. I. Khomskii, 1982, Sov. Phys. Usp **25**, 231.

Kumagai, K., T. Suzuki, Y. taguchi, Y. Okada, Y. Fujishima, and Y. Tokura, 1993, Phys. Rev. B **48**, 7636.

Lacorre, P., J. B. Torrance, J. Pannetier, A. I. Nazzal, P. W. Wang, and T. C. Huang, 1991, J. Solid State Chem. **91**, 225.

Langer, D. W., and H. J. Richer, 1966, Phys. Rev. **146**, 554.

Larson, B. E., K. C. Hass, H. Ehrenreich, and A. E. Carlsson, 1988, Phys. Rev. B **37**, 4137.

Lee, Y. R., and A. K. Ramdas, 1984, Solid State Commun. **51**, 861.

Ley, L., M. Taniguchi, J. Ghijsen, R. L. Johnson, and A. Fujimori, 1987, Phys. Rev. B **35**, 2839.

Mac, W., Nguyen The Kohi, A. Twardowski, J. A. Gaj, and M. Demianiuk, 1993, Phys. Rev. Lett. **71**, 2327.

Mac, W., A. Twardowski, P. J. T. Eggenkamp, H. J. M. Swagten, Y. Shapira, and M. Demianiuk, 1994, Phys. Rev. B **50**, 14144.

MacLean, D. A., H.-N. Ng, and J. E. Greedan, 1979, J. Solid State Chem. **30**, 35.

Mahan, G. D., 1981, *Many Particle Physics* (Plenum, New York).

Mahajan, A. V., D. C. Jhonston, D. R. Orgeson, and F. Borsa, 1993, Phys. Rev. B **46**, 10966.

Mann, J. B., *Los Alamos Scientific Laboratory Report* No. LASL-3690 (unpublished).

Massidda, S., M. Posternak, and A. Baldereschi, 1992, Phys. Rev. B **46**, 11705.

Massidda, S., A. Continenza, M. Posternak, and A. Baldereschi, 1995, Phys. Rev. Lett. **74**, 2323.

Matsumoto, G., 1970, J. Phys. Soc. Jpn. **29**, 606.

Mattheiss, L. F., 1972, Phys. Rev. B **5**, 290.

McClure, D. S., 1963, J. Chem. Phys. **39**, 2850.

Medarde, M., A. Fontaine, J. L. García-Muñoz, J. Rodríguez-Carvajal, M. de Santis, M. Sacchi, G. Rossi, and P. Laccore, 1992, Phys. Rev. B **46**, 14975.

Mizokawa, T., H. Namatame, A. Fujimori, K. Akeyama, H. Kondoh, H. Kuroda, and N. Kosugi, 1991, Phys. Rev. Lett. **67** 1638.

Mizokawa, T., and A. Fujimori, 1993, Phys. Rev. B **48**, 14150.

Mizokawa, T., H. Namatame, A. Fujimori, K. Akeyama, H. Kondoh, H. Kuroda, and N. Kosugi, 1994, Phys. Rev. B **49**, 7193.

Mizokawa, T., and A. Fujimori, 1995, Phys. Rev. B **51**, 12880.

Mochizuki, S., B. Piriou, and J. Dexpert-Ghys, 1990, J. Phys. Cond. Matt. **2**, 5225.

Morikawa, K., 1995, Thesis (University of Tokyo).

Morikawa, K., T. Mizokawa, K. Kobayashi, A. Fujimori, H. Eisaki, S. Uchida, F. Iga, and Y. Nishihara, 1995, Phys. Rev. B **52**, 13711.

Mott, N. F., 1949, Proc. Phys. Soc. Sect. A **62**, 416.

Mott, N. F., 1990, *Metal-Insulator Transitions* (Taylor and Francis, London).

Müller-Hartmann, E., 1989a, Z. Phys. B **74**, 507 (1989).

Müller-Hartmann, E., 1989b, Z. Phys. B **76**, 211 (1989).

Nimkar, S., D. D. Sarma, H. R. Krishnamurthy, and S. Ramasesha, 1993, Phys. Rev. B **48**, 7355.

Norman, M. R., 1991, Phys. Rev. Lett. **64**, 1162.

Ogasawara, H., A. Kotani, R. Potze, G. A. Sawatzky, and B. T. Thole, 1991, Phys. Rev. B **44**, 5465.

Okada, K., and A. Kotani, 1991, J. Phys. Soc. Jpn. **60**, 772.

Okada, K., and A. Kotani, 1992, J. Phys. Soc. Jpn. **61**, 4619.

Okada, K., A. Kotani, and B. T. Thole, 1992, J. Electron Spectrosc. Relat. Phenom **58**, 325.

Okazaki, A., 1969, J. Phys. Soc. Jpn. **26**, 870.

Okimoto, Y., T. Katsufuji, Y. Okada, T. Arima, and Y. Tokura, 1995, Phys. Rev. B **51**, 9581.

Oshiyama, A., N. Hamada, and H. Katayama-Yoshida, 1988, Phys. Rev. B **37**, 1395.

Park, J., S. Ryu, M. Han, and S.-J. Oh, 1988, Phys. Rev. B **37**, 10867.

Picoli, G., and A. Chomette, 1984, Phys. Rev. B **30**, 7138.

Raccah, P. M., and J. B. Goodenough, 1967, Phys. Rev. **155**, 932.

Roussos, G., and H. R. Schulz, 1980, Phys. Status Solidi B **100**, 577.

Saitoh, T., A. E. Bocquet, T. Mizokawa, H. Namatame, A. Fujimori, M. Abbate, Y. Takeda, and M. Takano, 1995a, Phys. Rev. B **51**, 13942.

Saitoh, T., A. E. Bocquet, T. Mizokawa, and A. Fujimori, 1995b, Phys. Rev. B **52**, 7934.

Saitoh, T., 1995, Thesis (University of Tokyo).

Sarma, D. D., O. Strebel, C. T. Simmons, U. Neukirch, G. Kaindl, R. Hoppe, and H. P. Müller, 1988, Phys. Rev. B **37**, 9784.

Sarma, D. D., 1990, J. Solid State Chem. **88**, 45.

Sarma, D. D., H. R. Krishnamurthy, S. Nimkar, S. Ramasesha, P. P. Mitra, and T. V. Ramakrishnan, 1992, Pramana-J. Phys. **38**, L531.

Sawada, H., N. Hamada, and K. Terakura, 1995, submitted to Phys. Rev. B.

Sawada, H., 1995, private communication.

Sawatzky, G. A., and D. Post, 1979, Phys. Rev. B **20**, 1546.

Schweitzer, H., and G. Czycholl, 1990, Solid State Commun. **74**, 735.

Shen, Z.-X., J. W. Allen, J. J. Yeh, J.-S. Kang, W. Ellis, W. Spicer, I. Lindau, M. B. Maple, Y. D. Dalichaouch, M. S. Torikachvili, and J. Z. Sun, 1987, Phys. Rev. B **36**, 8414.

Shirakawa, N., and M. Ishikawa, 1991, JJAP **30**, L775.

Shirley, D. C., 1978, in *Photoemission in Solids I*, edited by M. Cardona and L. Ley (Spliger-Verlag, Berlin), p. 165.

Skowronski, M., and Z. Liro, 1982, J. Phys. C **15**, 137.

Slater, J. C., and G. F. Koster, 1954, Phys. Rev. **94**, 1498.

Slater, J. C., 1960, *Quantum Theory of Atomic Spectra I, II*, (McGraw-Hill, New York).

Steiner, P., V. Kinsinger, I. Sander, B. Siegwart, S. Hüfner, C. Politis, R. Hoppe, and H. P. Muller, 1987, Z. Phys. B **67**, 497.

Steiner, M. M., R. C. Albers, D. J. Scalapino, and L. J. Sham, 1991, Phys. Rev. B **43**, 1637.

Steiner, M. M., R. C. Albers, and L. J. Sham, 1992, Phys. Rev. B **45**, 13272.

Sugano, S., Y. Tanabe, and H. Kamimura, 1970, *Multiplets of Transition Metal Ions in Crystals* (Academic, New York).

Svane, A., and O. Gunnarsson, 1990, Phys. Rev. Lett. **65**, 1148.

Taguchi, Y., T. Tokura, T. Arima, and F. Inaba, 1993, Phys. Rev. B **48**, 511.

Tanabe, Y., and S. Sugano, 1954a, J. Phys. Soc. Jpn. **9**, 753.

Tanabe, Y., and S. Sugano, 1954b, J. Phys. Soc. Jpn. **9**, 766.

Taniguchi, M., L. Ley, R. J. Johnson, J. Ghijsen, and M. Cardona, 1986, Phys. Rev. B **33**, 1206.

Taniguchi, M., A. Fujimori, M. Fujisawa, T. Mori, I. Souma, and Y. Oka, 1987, Solid State Commun **62**, 431.

Terakura, K., T. Oguchi, A. R. Williams, and J. Kübler, 1984, Phys. Rev. B **30**, 4734.

Thoronton, G., B. C. Tofield, and D. E. Williams, 1982, Solid State Commun. **44**, 1213.

Tokura, Y., Y. Taguchi, Y. Okada, Y. Fujishima, T. Arima, K. Kumagai, and Y. Iye, 1993, Phys. Rev. Lett. **70**, 2126.

Tokura, Y., A. Urushibara, Y. Moritomo, T. Arima, A. Asamitsu, G. Kido, and N. Furukawa, 1994, J. Phys. Soc. Jpn. **63**, 3931.

Tomimoto, K., 1995, private communication.

Tomonaga, S., 1950, Prog. Theor. Phys. **5**, 349.

Torrance, J. B., P. Lacorre, A. I. Nazzal, E. J. Ansaldo, and C. H. Niedermayer, 1992, Phys. Rev. B **45**, 8209.

Towler, M. D., N. L. Allan, N. M. Harrison, V. R. Saunders, W. C. Mackrodt, and E. Aprà, 1994, Phys. Rev. B **50**, 5041.

Treglia, G., F. Ducastelle, and D. Spanjard, 1980, J. Physique **41**, 281.

Treglia, G., F. Ducastelle, and D. Spanjard, 1982, **43**, 341.

Tsuda, N., K. Nasu, A. Yanase, and K. Siratori, 1990, *Electronic Conduction in Oxides* (Springer-Verlag, Berlin).

Tsukuda, N., and A. Okazaki, 1972, J. Phys. Soc. Jpn. **33**, 1088.

Uozumi, T., K. Okada, and A. Kotani, 1993, J. Phys. Soc. Jpn. **62**, 2595.

van der Laan, G., C. Westra, C. Haas, and G. A. Sawatzky, 1981, Phys. Rev. B **23**, 4369.

van Elp, J., B. G. Searle, G. A. Sawatzky, and M. Sacchi, 1991, Solid State Communi. **80**, 67.

van Elp, J., 1991, Ph. D. Thesis (University of Groningen).

van Veenendaal, M. A., and G. A. Sawatzky, 1994, Phys. Rev. B **49**, 3473.

Wakoh, S., 1977, J. Phys. F **7**, L15.

Weakliem, H. A., 1962, J. Chem. Phys. **36**, 2117.

Wei, S.-H., and A. Zunger, 1987, Phys. Rev. B **35**, 2340.

Wei, S.-H., and A. Zunger, 1993, Phys. Rev. B **48**, 6111.

Wollan, E. O., and W. C. Koehler, 1955, Phys. Rev. **100**, 545.

Yamada, K., and K. Yosida, 1970, Prog. Theor. Phys. Suppl. **46**, 244.

Yamada, K., and K. Yosida, 1975, Prog. Theor. Phys. **53**, 970.

Yamaguchi, T., S. Shibuya and S. Sugano, 1982, J. Phys. C **15**, 2625.

Yamaguchi, T., S. Shibuya, S. Suga, and S. Shin, 1982, J. Phys. C **15**, 2641.

Yeh, J. J., and I. Lindau, 1985, At. Data and Nucl. Data Tables **32**, 1.

Zaanen, J., G. A. Sawatzky, and J. W. Allen, 1985, Phys. Rev. Lett. **55**, 418.

Zaanen, J., C. Westra, and G. A. Sawatzky, 1986, Phys. Rev. B **33**, 8060.

Zaanen, J., 1986, Ph. D. Thesis, 1986, University of Groningen

Zaanen, J., and G. A. Sawatzky, 1987, Can. J. Phys. **65**, 1262.

Zaanen, J., and G. A. Sawatzky, 1990, J. Solid State Chem. **88**, 8.

Zubkov, V. G., G. V. Bazuev, V. A. Perelyaev, and G. P. Shveikin, 1973, Sov. Phys. Solid State **15**, 1079.

Zubkov, V. G., A. S. Borukhovich, G. V. Bazuev, I. I. Matveenko, and G. P. Shveikin, 1974, Sov. Phys.-JETP **39**, 896.

Zunger, A., 1986, in *Solid State Physics* Vol. 39, edited by H. Ehrenreich and D. Turnball (Academic, New York).

98